AN EXPERIMENTAL STUDY OF MN_{12}-FAMILY MOLECULAR MAGNETS IN ISOLATION WITH HIGH SPATIAL RESOLUTION

A Dissertation

by

KELLEY THOMAS REAVES

Submitted to the Office of Graduate and Professional Studies of
Texas A&M University
in partial fulfillment of the requirements for the degree of

DOCTOR OF PHILOSOPHY

Chair of Committee,	Winfried Teizer
Committee Members,	Janet Bluemel
	Joseph H. Ross Jr.
	Jorge M. Seminario
Head of Department,	Ibrahim Karaman

December 2014

Major Subject: Materials Science & Engineering

ABSTRACT

I report my studies of $Mn_{12}O_{12}(C_6H_5COO)_{16}(H_2O)_4$, which will be referred to as Mn_{12}-Ph, a single molecule magnet, on Cu(111) and HOPG (highly oriented pyrolytic graphite) surfaces by scanning tunneling microscopy (STM). A technique of vacuum spray injection for room temperature deposition of films of a tunable density, between very diffuse isolated molecules and complete surface coverage, onto sample substrates was developed and used to create sub-monolayer films of Mn_{12}-Ph on Cu(111) for low temperature observation. Scanning tunneling spectroscopy (STS) of samples at low temperatures produced insights into the local density of states (LDOS) with a high degree of precision with spatial location (X,Y,Z) and energy (eV). These spectroscopic data were analyzed and compared to results in the literature from competing groups. A theoretical model of spin stability in an interacting graph of spins was developed and simulations were carried out to find a weak topological invariant to perturbation of a given spin state for a class of ferromagnetically interacting spin-graphs. A phenomenological (*post hoc*) model built upon poor coupling between the molecule's wave function and the Cu surface wave function is proposed to explain the spectroscopic data. Normalized (to the Cu background) junction impedance is calculated and compared in different regions of the molecular interior to form a better view of the evolution of the tunnel junction current with respect to applied bias voltage.

DEDICATION

I dedicate this document to my wife, Melissa Fuller, for putting up with the 21 months of overseas travel and the years of frustration behind my research before finally having results and for then showing me my poor grammar as I tried to report those results.

ACKNOWLEDGEMENTS

I would like to thank Dr. Winfried Teizer, my committee chair for providing the support and access to the community necessary for me to do this work, and for his continually good advice along the way. I would like to thank the members of my committee, Dr.Janet Bluemel, Dr. Jospeph H. Ross Jr., and Dr. Jorge M. Seminario for their guidance and feedback as I made progress towards completion of this document.

I would like to thank Dr. Helmut Katzgraber for helping shape my views on academic research and refining my output into professionally constructed and presented documents and Dr. Igor Roshchin for his help in refining the expression of my ideas and work.

I would like to thank the World Premier Institute program, Advanced Institute for Materials Research at Tohoku University in Sendai, Japan for hosting me and funding my research. Specifically Dr. Katsuya Iwaya, Dr. Patrick Han, Dr. Yoshinori Okada, and their boss Dr. Taro Hitosugi. Additionally I would like to thank Dr. Daniel Packwood and Dr. Filippo Federici for helping develop our modeling collaboration, some of which discussed is in this document.

Finally I would like to thank Dr. Glenn Agnolet for helping me to interpret my analyzed data when the observations seemed strange, and Ross McDonald for helping me decode data files and then walking me through the process of building a MySQL database to query for my analysis.

TABLE OF CONTENTS

LIST OF FIGURES

FIGURE Page

1. INTRODUCTION TO AN EXPERIMENTAL STUDY OF MN_{12}-FAMILY MOLECULAR MAGNETS IN ISOLATION WITH HIGH SPATIAL RESOLUTION

This is an experimental study, though I will use modeling techniques and phenomenological analysis of my results and compare to theoretical work done by others. My primary focus was observation of intact molecules on a surface with control of the key parameter of coverage density. Theoretical work and data interpretation are discussed in more detail in section 1.4 and section 5 of this dissertation. Details of modeling techniques can be found in section 1.4, as well as sections 2 and 6 of this dissertation. Scanning tunneling microscopy (STM) was my primary observational technique allowing me to study topography and electronic structure in fine detail. Scanning tunneling spectroscopy (STS) was used for high energy resolution studies of selected areas after observation via STM. For further introduction to STM and its related techniques see sections 3, 4, and 5.

Mn_{12}-Family molecules share an 'inner core' structure, as you can see in Figure 1.1, composed of eight Mn^{3+} and four Mn^{4+} ions and twelve O atoms. The ions are connected through Mn-O-Mn or Mn-O-O-Mn. These substructures are also connected to an 'outer shell' of organic ligand molecules. The molecule we spent the most time studying was referred to as Mn_{12}-Ph, by which we meant 'manganese-12-phenol' with a chemical structure $Mn_{12}O_{12}(C_6H_5COO)_{16}(H_2O)_4$. This molecule might more accurately be called 'managanese-12-benzoate' but not being chemists, the other less correct description took hold. The most commonly studied structure, and one we will use on occasion as a comparison, is Mn_{12}-Ac; instead of our benzene-like rings there is a simple acetate structure outside the 'core'. The differences in

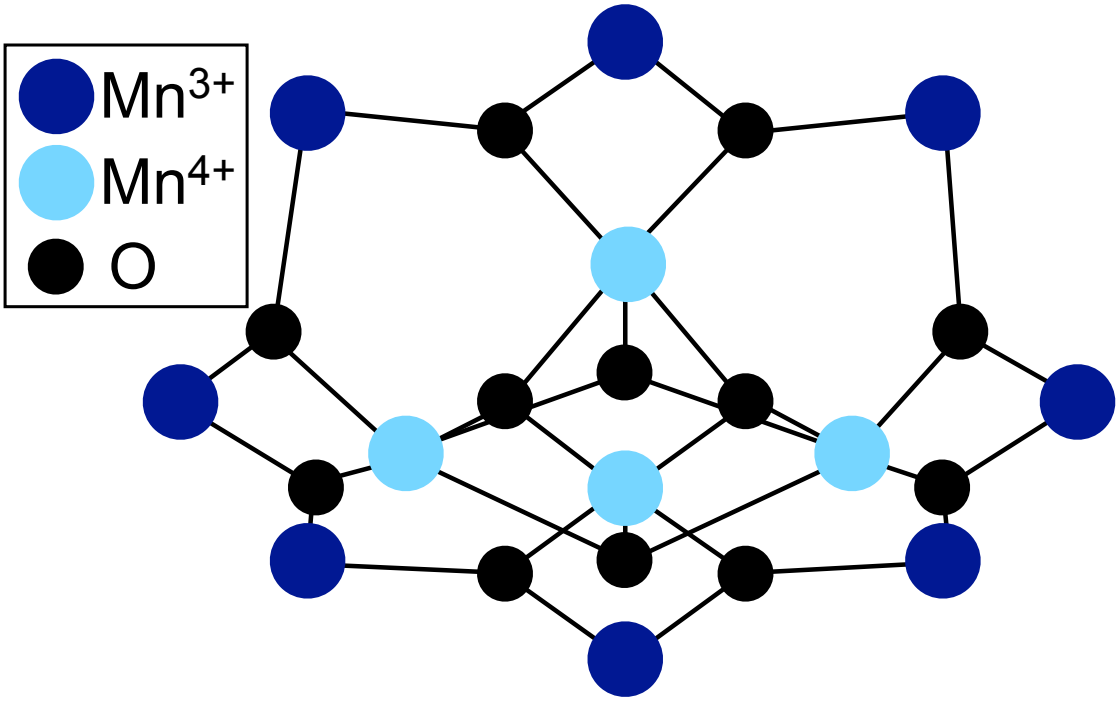

Figure 1.1: Structure of the Mn_{12} molecule's inner core. The dark large circles are Mn^{3+} ions, the lighter colored large circles are Mn^{4+} ions, the smaller black circles are O atoms, and the lines indicate a chemical bond (of O to Mn). This double shell has tetragonal symmetry and consists of an inner shell and an outer shell of Mn ions. This is a cartoon and in no particular scale, it is meant only to depict connectivity of the inner core atoms.

structure, and why we decided upon the molecule we used, will be discussed later in sections 2 and 4.

High spatial resolution is meant to imply lateral resolution that is atomic or near atomic, and vertical resolution that is better than atomic. This works out to mean a lateral resolution that is in angstroms (Å) and a vertical resolution in tenths of angstroms (0.1Å) at least. This is not simple to achieve without vacuum conditions. To gain fine energy resolution we will also require low temperatures. These two criteria will influence the choices made for producing samples, and this is discussed in sections 4 and 5.

1.1 The initial goals

This project is carried over from a previous student of Winfried Teizer. This previous student, Dongmin Seo, used AFM, STM, and SQUID techniques to study films of Mn_{12}-Ac written formally as $Mn_{12}O_{12}(O_2CCH_3)_{16}(H_2O)_4$. My initial goal was to try and reproduce D. Seo's work[1] looking for ordered film assembly on surfaces. While I was able to re-create the experimental conditions I did not observe the same results at first, though I was able eventually to give a reasonable explanation of his results and why we were not re-observing them.

Seo has presented a compelling image, Figure 1.2, where you can see order in the film as seen via atomic force microscopy (AFM) next to a control sample. It was understood from Seo's deposition technique that the molecules should have been intact on the surface, but it was a mystery as to why an ordered film would appear. Seo had some speculation as to what might have caused the behavior, and so my task was to investigate that phenomena further. It is commonly understood that these molecules should not strongly interact because of the organic ligand shell. This organic shell keeps the core too far away from any neighboring molecules to

magnetically interact. That leads the spacing observed to be particularly puzzling because it left very few options for which interactions might be occurring which could have the characteristic length of the apparently periodic spacing observed, which was on the order of the size of the molecule and which is at least an order of magnitude larger than the periodicity of the substrate surface.

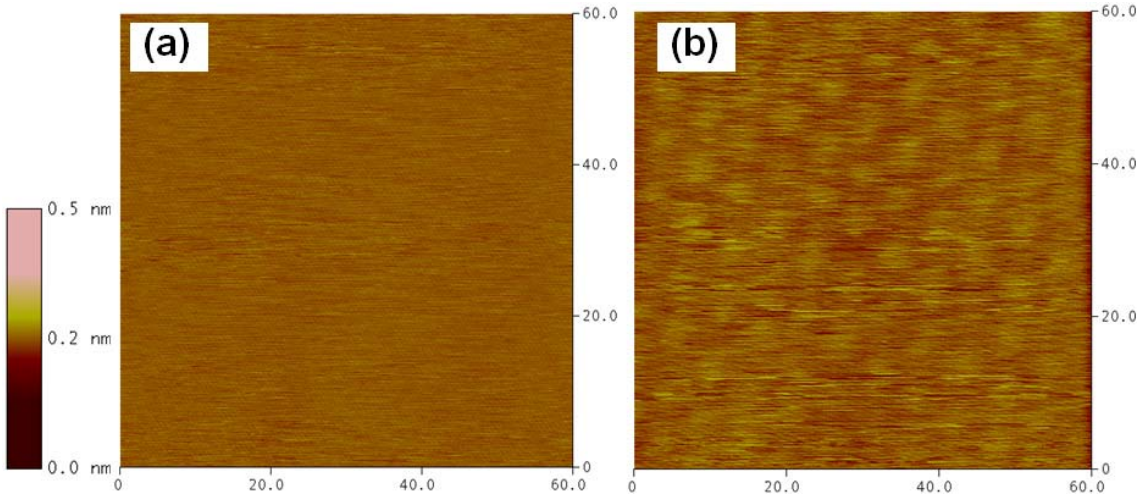

Figure 1.2: Fig. 4.12. from[1] STM images of (a) the solvent exposed HOPG, and (b) the Mn12-acetate thin film on HOPG with same conditions. The scan size of 60 nm and height scale of 0.5 nm are the same for both images. A current setpoint = 10 pA, bias voltage = 900 mV, and scan rate = 4 Hz have been used for both images.

To do this I would need to be able to: reliably deposit films with predictable densities, and understand the various competing forces involved in deposition and film formation. In addition to being able to produce samples, I would need a way of observing the film. The obvious choices were AFM, STM, and SQUID techniques to mirror Seo's work exactly.

1.2 In general, the experimental approach

In an effort to mirror the work of the previous student (Seo) I initially adopted his experimental methodology as a place to begin where I should produce known results. For further details of his work, see Seo's dissertation[1].

In order to prepare a sample for study as a film, it is necessary to produce concentrated Mn_{12}-family molecules in solution. This can be done by dissolving the original Mn_{12} micro-crystalline powder material in an appropriate solvent, chosen by the organic ligand of the Mn_{12} molecule. Various concentrations were studied in various solvents.

This solution is then applied to a substrate. In general there are two ways to do this. The first, and simplest, is to apply the solution directly to the substrate and then allow evaporation of the solvent to occur in a clean environment. The second method is to in some way spray the molecule onto the substrate. We started with the former method and transitioned to the latter for reasons of consistency.

Sample films can then be studied by various scanning probe methods to check for density and consistency of the films. Primarily I used physical probe methods like AFM and STM, but I also did SEM with EDX testing, which uses a collimated electron beam of a known energy as the probe, while tuning the sample preparation parameters. The goal was to have a surface density that was low enough to ensure some molecules were not aggregated into films but dense enough that the search time, with a technique like STM, for a molecule was short. More detail can be found in sections 3.2 and 3.4.

Samples of the micro-crystalline powder were used for superconducting quantum interference device (SQUID) magnetometry and X-ray characterization techniques to test sample purity before use in the other experiments. This testing also gives

a baseline measurement of behavior at the macroscopic level to be compared to measurements made at the microscopic scale.

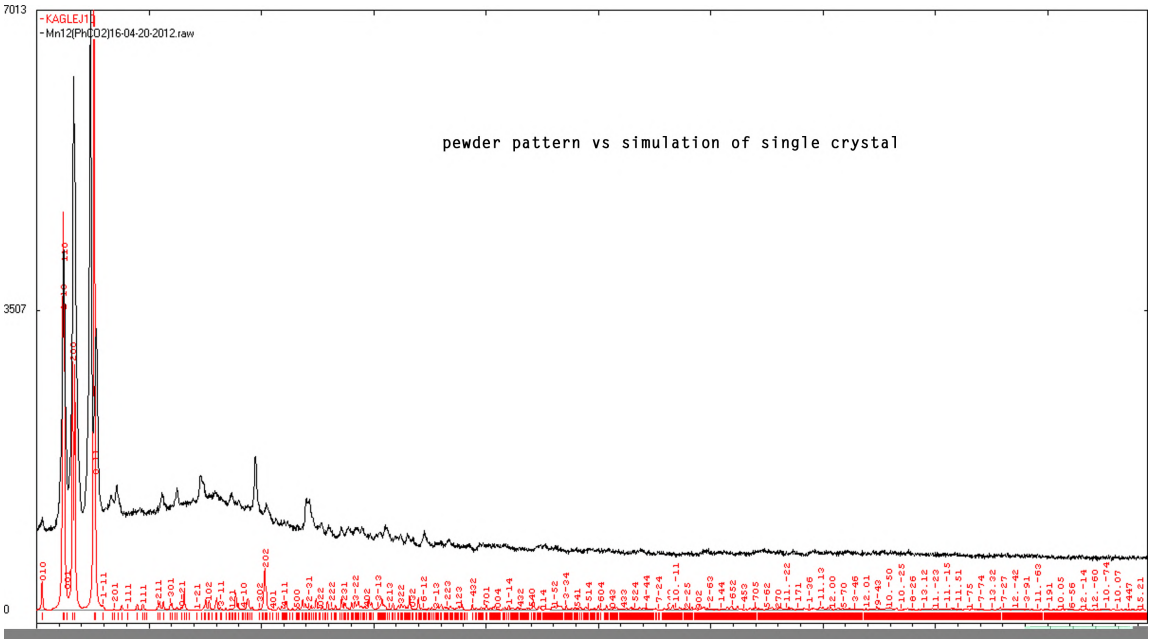

Figure 1.3: Plot of x-ray peaks of simulation and actual Mn_{12}-Ph micro-crystalline powder generated by H. Zhao, who prepared the raw Mn_{12} powder used in all of our experiments. The observed and simulated peaks are in good agreement though the micro-crystal powder shows elevated background signal from the random crystal orientations of the powder sample. This plot is from the summer of 2012 before my first trip to Japan. We received several more batches of sample with similar results.

1.3 Where the work was done, and why

Hanhau Zhao of the Dunbar chemistry group at Texas A&M synthesized the micro-crystalline powder samples of our molecular magnets and performed any ligand substitution that was required (*i.e.* switching from acetate to benzoate). The validation of synthesis is shown in Figure 1.3 where you can see good agreement between the single crystal simulation peaks and the observed peaks from the micro-

crystal powder. The SQUID and X-ray characterization of those powder samples was done at A&M (also by equipment provided by the Dunbar group). A&M has many STM groups but none of them had the specific range of capabilities needed to conduct this experiment. Namely, the STM would need to be low temperature, have the ability to apply a variable magnetic field preferably along multiple axes, and allow for preparation of the sample and transfer to the STM without breaking vacuum.

To that end I spent three months and then eighteen months in Sendai, Japan working with the Itaya surface chemistry group and then the Hitosugi STM group associated with the World Premier Institute: Institute for Advanced Materials Research (WPI-AIMR) at Tohoku University. The Hitosugi group actually has not one but two of these STMs, one of which is limited to operating at liquid He^4 temperatures ($\approx$ 4.9 K) and another machine with a dilution refrigerator allowing sub 1 K measurements. During my first three month stint, I worked for a little more than two months perfecting sample preparation and using AFM and ambient STM to observe my progress. Then we received roughly a week of time on the LT-STM. These samples were Mn_{12}-Ac on HOPG. The results of this work will be discussed in section 4. The later stint in Japan was geared towards preparing samples in vacuum and perfecting low temperature samples for eventual time on the LT-STM with the dilution refrigerator. We had nearly unlimited access to the other LT-STM and roughly three weeks of time with the very low temperature machine at the end of the trip.

2. BACKGROUND FOR AN EXPERIMENTAL STUDY OF MN_{12}-FAMILY MOLECULAR MAGNETS IN ISOLATION WITH HIGH SPATIAL RESOLUTION

2.1 Early theoretical work and modeling

Looking into how this molecule might form films I adopted a first principles approach. Given that neither Seo nor I were using ligand replacement to bond the molecule to a surface like gold[2] the dominant interactions at room temperature should be Van der Waals forces. The two objects closest together in our experiment are an isolated molecule and the surface it rests upon. The sphere to plane Van der Waals interaction has this form: $U(r) = -\frac{\alpha}{r^3}$ where $U(r)$ describes the interaction strength and r is the distance between the center of the sphere (which is what we assume our molecule to be for this simple model) and the plane it is interacting with (our surface). This interaction is very short range (sub-nanometer) but is relatively strong. The next scale to consider is the intermolecular interaction which is on the order of nanometers. This can be approximated as a sphere to sphere Van der Waals interaction which has the form: $U(r) = \frac{A}{r^12} - \frac{B}{r^6}$, where A and B are constants and r is the center-to-center distance between the spheres. In the image in question (Figure 1.2) this is roughly 6 nm, this center-to-center distance is too large to be a close-packed film. Since the film is not close-packed, but does appear ordered we could hypothesize that the spacing must derive from competition between the available interactions.

If we were to plot these two behaviors together we might expect to see some crossing where there was some critical density at which these competing interactions form an ordered film. However, if we use appropriate values for all of the constants

involved (and keep in mind the strong distance dependence) we would notice that these curves never cross in the range observed in the image due to issues of scale. So this would not explain the observation.

The temperature these images were obtained at is well above the blocking temperature of the molecule (which will be discussed further in section 2 in the section regarding molecular magnetism) and so there is no ferromagnetic ordering to explain the observation.

The control sample, which was produced using the exact procedure as the sample which produced a film but which had no Mn_{12}-Ac in the solvent when it was applied to the surface, makes it unlikely that this is a solvent-surface interaction of some kind of a solvent introduced contaminant.

This remained puzzling until we spoke with some other probe-microscopy experts. A very probable explanation for the observation is that the 'molecules' seen in the image are in fact due to an electronic analogue of the Moire pattern where repeated lattices in the $\hat{z}$ direction with slightly different orientations produce a visual superstructure with periodicity much larger than the objects making up the lattice. The AFM and STM are both subject to being fooled by this when over layers of polar molecules like water or over graphite whose layers are not perfectly matched in alignment. In our case we have both of these present. Water is introduced in the micro-crystalline powder of the molecule which explains why it is not present in the control sample. See Figure 2.1 for a glimpse of a simple visual Moire-superstructure caused by a 3° mismatch between two layers of an otherwise identical lattice structure.

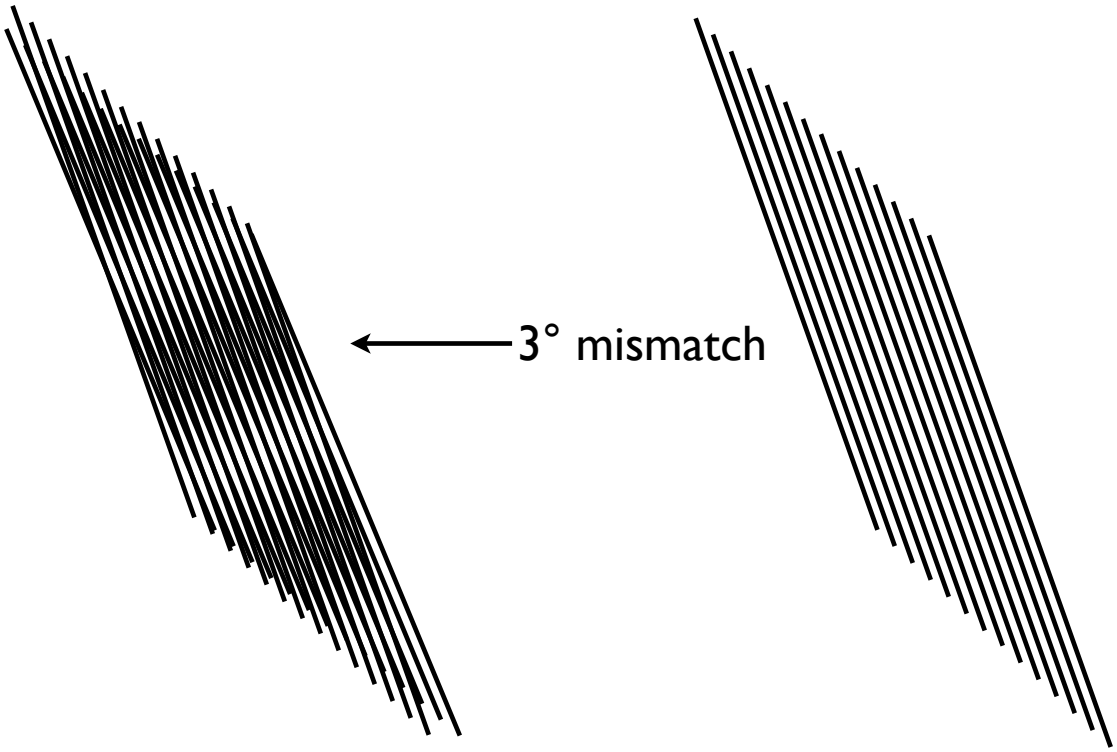

Figure 2.1: A visual Moire pattern due to a 3° mismatch between layers of a repeated pattern (diagonal lines in this case)

2.2 An overview of SPM

Scanning probe microscopy (SPM), which will be discussed in some detail in section 3, is a family of techniques involving some very small tip, in the case of STM an atomically sharp tip, which is connected through a feedback mechanism to a computer which generates 2D surface maps with a false-color $\hat{z}$ scale. In the case of Atomic Force Microscopy (AFM), this color typically indicates either height or phase (AFM assumes a Hooke's law like oscillation of the tip and measures deflection and the angle between the oscillation phase and that of the driving force). AFM is still subject to non-obvious influences of an electronic nature because the tip-surface interaction is through the Van der Waals force which is not independent

of the surface-charges involved. STM similarly measures a height, but does so by controlling a tunneling current between the tip and the surface. This tunneling current has an understood height dependence in an ideal sense, but is dependent on the work function of both the surface and the tip, as well as anything which happens to be in the tunnel junction. STM data is therefore notoriously difficult to transform into true height (again further details will be presented in sections 3, 4, and 5).

2.3 Updated goals

Having repeated Seo's work, and having a reasonable explanation in hand it was decided that we should move further and explore this system in more detail. The new goal of the work was to show evidence of ferromagnetic behavior in single molecules. This was a very ambitious goal and would involve developing a more controlled sample preparation technique which was capable of being made in a vacuum system for transfer to a low temperature STM with *in situ* access to a variable magnetic field and low temperatures.

2.4 Molecular magnets

Molecular magnets (MMs) contain roughly 4 to 100 electron spin centers (typically the d-electrons of transition metal ions) with a large total electron spin and magnetic moment[3, 4, 5, 6]. MMs typically physically are large molecules, several (to tens) of nm across, containing tens to hundreds of atoms. MMs possess unique magnetic properties that span both the classical and quantum regimes. This leads them to be of great fundamental and practical interest[9]. Figure 2.2 shows a phenomenon termed thermally assisted tunneling of magnetization across the prototypical double-well of magnetization energy of our molecule. The double-well is created by the highly anisotropic structure of the spin interactions (there is an easy magnetization axis and mirror symmetry). This tunneling phenomena is caused

when energy levels line up across the anisotropic energy barrier allowing for a a spin flip to tunnel directly through the barrier rather than being excited above it. This level alignment can be changed by applying a magnetic field to bias the double-well, and tuned to allow or disallow this tunneling phenomenon. This phenomenon can be observed as vertical steps within the hysteresis loop for in Mn_{12}-Ph and is a quantum phenomenon observable at the macro-scale[13, 12].

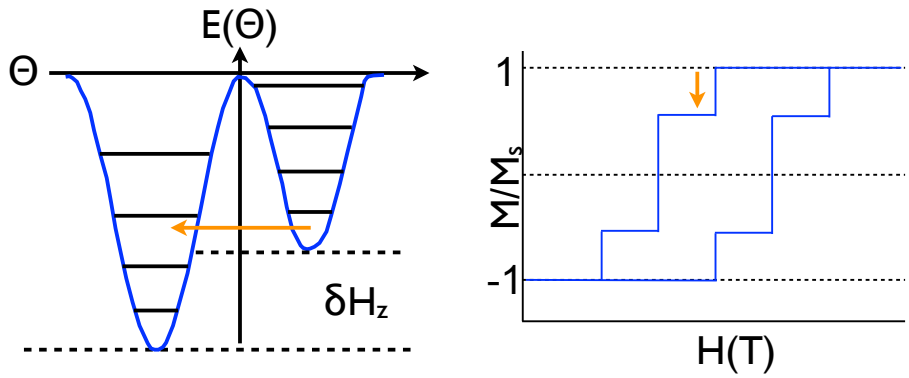

Figure 2.2: Cartoons of magnetization hysteresis and the corresponding energy versus spin orientation 'double-well' for some fixed temperature, T below the blocking temperature, and the thermally assisted (resonant) tunneling that occurs as the applied field distorts the 'double-well'. You can see the brightly colored arrow in the energy versus spin orientation graph showing spin tunneling from a lower spin state into a higher spin state of the opposite direction, made preferably by an applied magnetic field H, and the same arrow is shown on the magnetization cartoon.

2.5 Molecular magnetism

This will be a brief overview of molecular magnetism; entire text books have been written on this subject and that depth is beyond the scope of this document. I relied heavily upon the text book written by Dante Gatteschi, Roberta Sessoli, and Jacques Villain[33] to develop my understanding of molecular magnetism and the Mn_{12} family

of single molecule magnets. It is probably simplest to describe molecular magnets through the Zeeman Hamiltonian (Spin Hamiltonian).

$$H_Z = -\vec{H} \cdot \vec{m} = \mu_B \vec{H} \cdot \vec{g} \cdot \vec{S} \tag{2.1}$$

In this equation we have $\vec{H}$, the applied magnetic field, $\vec{m}$, the magnetic moment, $\vec{S}$ a spin operator, μ_B, the Bohr magneton, and $\vec{g}$ which is a tensor connecting the applied field to the spin operator. We can begin to add higher order terms, the ligand field, surface interactions, symmetry terms, and so on. To come up with analytic solutions using this Hamiltonian approach is only practical with a very small number of interacting spins. As already indicated, that is not typically the case for the molecules we would like to study but a lot of effort has been put into doing exactly that[7, 8].

2.5.1 Symmetry

Symmetry (and asymmetry) play strong roles in magnetic interactions. Molecular magnets require a few building blocks. Strong magnetic centers are needed as connection nodes in our pile of building blocks; the connections need to allow for (strong) spin coupling so that our overall structure is a set of interdependent spins forming one large net spin (at low temperatures). Asymmetry in the structure leads to a more strongly history dependent relaxation of magnetization. At very low temperatures, size effects change the dominant resistance to changing magnetization states from moving domain walls to a quantum tunneling of spin effect[34]. Single molecule magnets are too small for the domain effect to have ever been present, and thus show a behavior termed superparamagnetism above their blocking temperature. At these higher temperatures the super-paramagnetic behavior, soft magnets whose spins-flips can occur with the same characteristic timescale as any measurement ex-

periment performed. The transition between these behaviors is called the blocking temperature, and it corresponds to the relaxation time for a given magnetization state being equal to the characteristic timescale of the experiment. We will discuss asymmetry further in section 6.

2.6 Mn_{12}-Family molecular magnets

Figure 2.3 shows the structure of the prototypic example of an MM, Mn_{12}-Ph . $Mn_{12}O_{12}(C_6H_5COO)_{16}(H_2O)_4$. Mn_{12}-Ph consists of four Mn^{4+} ions and eight Mn^{3+} ions connected together through Mn-O-Mn or Mn-O-O-Mn bridges and an outer ligand shell. The coupling between the electrons of the Mn ions via the Mn-O-Mn and Mn-O-O-Mn bridges gives the Mn_{12}(Ac) molecule a total ground state electron spin of 10[4, 10]. The structure of MMs can be described in terms of the arrangement of the metallic core atoms in the molecule, which act as spin-centers. In the case of Mn_{12}(Ac), the four Mn^{4+} ions are arranged in a tetrahedral 'core' with the eight Mn^{3+} ions arranged in a ring around the periphery of the tetrahedron which also contains bonds to the organic ligand shell. Many other types of MMs with a wide range of compositions, sizes, and shapes (spin arrangements) are reported in the literature[11]. I refer to Mn_{12}-Ph, for phenyl, though to be completely chemically correct they are benzoate ligands. Sixteen benzoate ligands surround the core, determining the intrinsic minimal spacing between the magnetic molecules in a close-packed arrangement. This distance is relatively large, suppressing the magnetic interaction between neighboring molecules[14, 15].

Molecular magnets (MMs) contain roughly 4 to 100 electron spin centers (typically the d-electrons of transition metal ions) with a large total electron spin and magnetic moment[3, 4, 5, 6]. MMs typically physically are large molecules, several (to tens) of nm across, containing tens to hundreds of atoms. MMs possess unique mag-

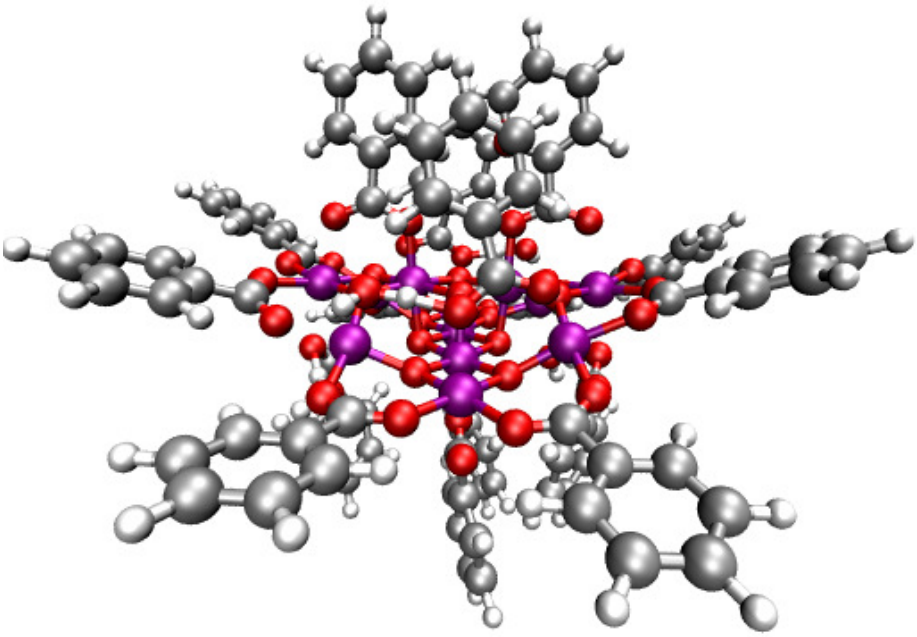

Figure 2.3: Structure of the Mn_{12}(Ph) molecule. The purple spheres in the center of the image are Mn ions, the red spheres surrounding the center are O atoms, on the outer edge of the image the grey spheres are C atoms, and the white spheres are H atoms. The radius of the Mn atoms has been modified from their ionic radius for clarity.

netic properties that span both classical and quantum domains, making them of great fundamental and practical interest[9]. Figure 2.4 shows a phenomenon termed thermally assisted tunneling of magnetization, seen as vertical steps within the hysteresis loop, in Mn_{12}-Ph, a quantum phenomenon observable at the macro-scale[13, 12].

2.7 Introduction to the current state of the field

Addressing individual magnetic molecules without damaging their structure and functionality is an essential prerequisite for designing molecular-level studies with controlled parameters and of course for development of useful devices using the technology[6]. However, in spite of the substantial efforts to organize magnetic molecular materials and to increase the sensitivity of measurement techniques, it is not

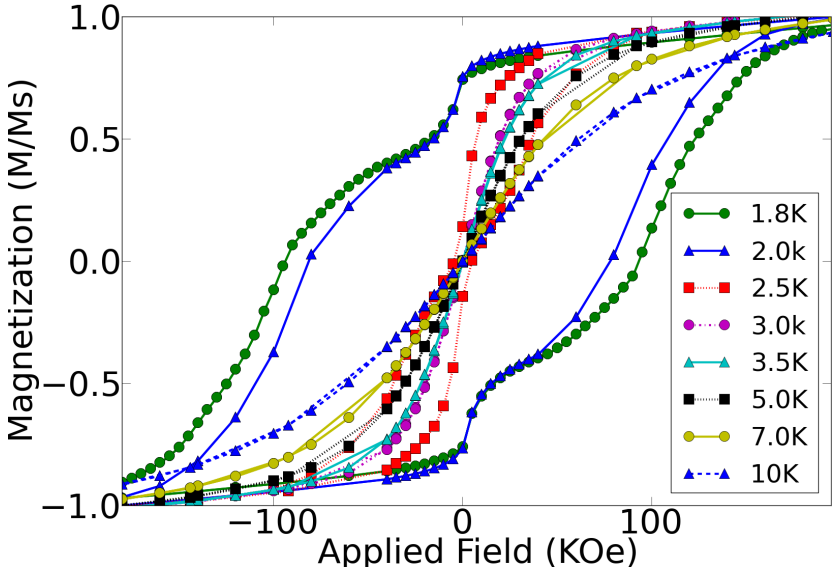

Figure 2.4: Magnetization of Mn_{12}-Ph powder sample as a function of applied magnetic field at different temperatures, $1.8\,K \leq T \leq 10\,K$. The measured magnetization has been normalized to the saturation value ($M_s \approx 0.22\,Am^2$) to remove sample size dependence but the data has not been adjusted to remove the systematic slope present in the data.

established whether individual molecular units isolated on a surface are unaltered from their bulk configuration[16]. Recently, scanning tunneling microscopy (STM) has been successfully utilized to identify several supramolecular metal ion assemblies deposited on HOPG surfaces at room temperature. The metal centers in the assemblies, such as Fe, Co, Cu and Mn, are recognizable as evident 'bright' spots in two-dimensional scanning tunneling spectroscopic (STS) images[16]. This is because of significantly enhanced tunneling currents increasing near the metal centers. The STS image-based approach provides the spatial location and arrangement of the core elements of the molecule under the STM tip which is a crucial clue to confirming the internal electronic structure of the molecule dynamically while also observing the arrangement of the local topological configuration with atomic resolution. The latter

will be an important feature, particularly in any spin-polarized tunneling studies, to understanding the magnetic connectivity of the spin network within the cluster of spin centers.

The original groups working with various Mn_{12} molecules since they reported their synthesis[14, 4] in 1993 consistently involve Roberta Sessoli, Dante Gatteschi, and Andrea Cornia. The research groups these chemists are associated with have continued to study Mn_{12} in the years since 1993, publishing roughly a dozen articles and a textbook on the subject as recently as this last year (2013). The path of their research began with synthesis and stability in solution and evolved to thin films on Au(111) with and without ligand substitution to bond the molecules to the surface and other surfaces to attempt to study the magnetic behavior in isolation as they had done in bulk crystal[6]. This work then led to a better understanding of the exchange coupling allowing for the prediction of various energy levels above the ground state[10].

More closely related to the course of experiments that I performed are those of George Christou's[7, 17] group, Wolfgang Wernsdorfer's group[18], and Roland Wiesendanger's probe microscopy group[19]. Their work shows that it is possible to deposit and study the molecule in isolation and then address it via probe microscopy. To date molecules have been studied on noble metals[20], on thin insulating films[21], and very recently on a semi-metal[22]. These represent a steady incremental advancement towards more industrially useful materials, as well as better fundamental understanding of Mn_{12}, its internal structure, and interaction with substrates.

2.8 Graph structures

Due to the limited ability of Hartree-Fock, Density Functional Theory, and Molecular-Dynamic simulations to quickly and simply simulate magnetic properties of large

systems (hundreds of atoms in size) a new and different methodology was desirable. We intended to study the ability of a complex interconnected structure to maintain its magnetic state when distorted. This would ordinarily lend itself to a spin-Hamiltonian treatment, but these models rely upon knowing (or having a very good approximation for) the interaction constants, J[23, 24]. This is a very hard physics problem to approach from first principles, but by simplifying it there was the possibility of keeping enough physical reality but using a mathematically simple model. With that trade off in mind, a mathematical model was developed.

2.8.1 Statement of the goal

1. First, modeling in this way is intended to develop a consistent and proscriptive explanation of the stability of a graph of n connected nodes under perturbation through self interaction and interaction with an external perturbation.

2. For application to Mn_{12}-family molecules, this goal must be narrowed to modeling the physical and electronic structure of an Mn_{12} molecule to find topologically invariant structural configurations and electronic states while on non-trivial surfaces.

To accomplish these goals a model has been developed which includes a graph which is defined as a collection of nodes and their associated connectivity matrix, referred to as edges. These structures can be representations of a molecule and its analogous electronic interactions (for instance the physical graph where the interaction is mediated by spin-spin interactions). With these graph(s) in hand, then a method of performing perturbations of the graph(s) to explore stable configurations has been explored.

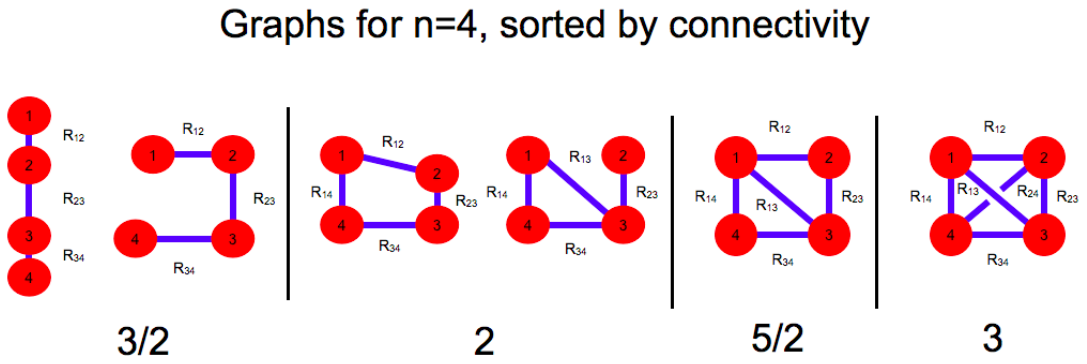

Figure 2.5: Generic graph connectivities, named for convenience: Straight Line, Branched Line, Doubly Connected Branched Line, Bent Square, Square, and Tetrahedron or Pyramid (depending on how it is arranged) for use in studying the P value of simple shapes

2.9 The model in general

Each graph in Figure 2.5 consists of a number of nodes, n, with the nodes connected to at least one neighbor (representing interactions between nodes, *i.e.* interacting spins). Then, all of the possible representations of the graph are generated. Each bond has a bond distance, $\vec{R}$. Then the graphs undergo a random perturbation (by adding a vector $\vec{U} = \vec{u_i}, \vec{u_j}, \vec{u_k}$ where the components of $\vec{U}$ obey a Gaussian distribution. Then the modified distance is now changed by $\Delta\,\vec{R}$. Now a function which we will call stability is defined as P for each graph.

$$P = \frac{\Sigma \Delta \vec{R}}{\Sigma \vec{R}} \tag{2.2}$$

Then we define the population variance of P, $var(P)$ in the usual way, which is what we will compare (and minimize) as the value of stability for each graph. In Figure 2.5 I have included the set of graphs for $n_e = 4$. In these graphs you can see that from right to left connectivity increases. Simple calculations suggest that $var(P)$

decreases with increasing connectivity, n_e (the number of edges). These simple calculations also (for a given graph) seem to show that $var(P)$ appears to minimize when the nodes are arranged in a high-symmetry conformation. Then, using small perturbations around stable points (minimums in $var(P)$), one can determine if the stable point is really a minimum or a metastable point.

2.9.1 The analytic (toy) model

1. All coupling is ferromagnetic, the strength of which is defined by distance between nodes, R_{ij}.
2. All $\Delta R_{ij} = 1$
3. All displacements, Δ are small compared to the total graph size ($\sum R_{ij}$).

From these assumptions the relationship P can be shown to have the following:

$$var(P) = 2\sigma^2 S \tag{2.3}$$

$$S = \frac{1}{n_e} + \frac{1}{n_e^2} \sum_A \cos(\Phi_a) \tag{2.4}$$

σ^2 is the standard deviation of the population constructed in the usual way. $var(P)$ is the variance of a set of P, from the population used to calculate standard deviation, also defined in the usual way. A refers to adjacent edges, and Φ_a is the interior angle between adjacent edges.

This allows us to analytically predict the minimum P by minimizing S. S is smallest when Φ_a approaches π.

The result of this model was (in order of increasing $var(P)$):

1. Straight Line with $S = \frac{1}{9}$

2. Forked Line

3. Doubly Connected Forked Line

4. Square

5. Bent Square

6. Tetrahedron or Pyramid with $S = \frac{1}{3}$

2.9.2 The naive computational model

1. Graphs consist of Nodes and Edges with no spacial coordinates enforced

2. All $\delta R_{ij} = 1$

3. All displacements, Δ are small

This is a very general construction of the graphs which has fully independent nodes since every edge length can be varied independently without the effect rippling out to all the connected edges for a particular node. If that is taken into account and added as a further constraint, then the resulting computational solution is found to be identical to the analytic results. The variances of the simpler shapes (in terms of connectivity) are very close together but clearly distinct beyond the variance of the set of variance of P values and trend towards a single value as seen in Figure 2.6.

2.10 The second computational model

The second computational model was developed to exactly mirror the analytic method. Each node in a graph now has a location vector as well as an edge (connectivity) matrix. The location vector for a node is modified rather than perturbing each edge, then the length of the edge matrix is recalculated (preserving connectivity). This model was also made ready for running on multiple CPUs with the ability to integrate the data for later processing on a less capable machine.

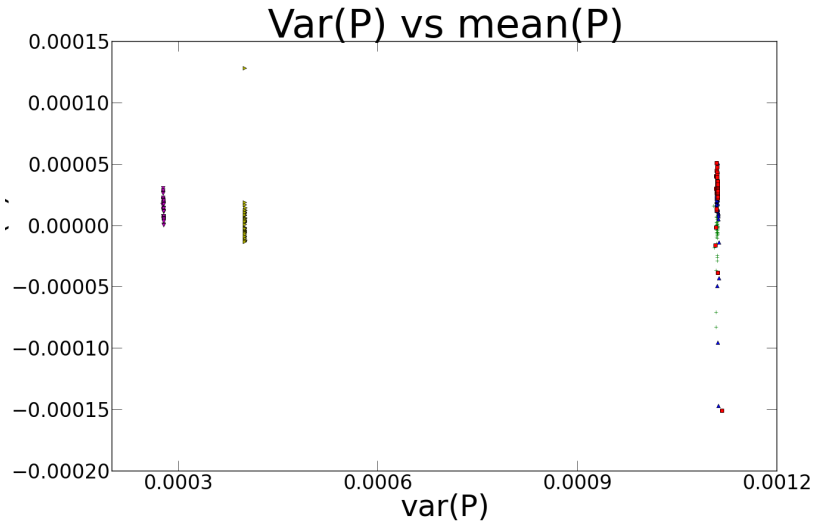

Figure 2.6: 50 independent P values per shape, each with 100000 random perturbations applied to their structure (but not connectivity). Magenta is the Tetrahedron, Yellow is the Bent Square, Red is the Square, Blue is the Doubly Connected Branched Line, Green is the Branched Line, and Black is the Straight Line.

2.10.1 What was done next to improve this model

1. This model can (with the same stability calculation) be used to model spins with the introduction of a coupling constant along the connections $\vec{J}$ to replace $\vec{R}$. In the physical system the bond length is related to the interaction strength (and sign). This spin graph also needs to take into account different spin multiplicities, since Mn_{12} has four Mn^{4+} with spin 3/2 and eight Mn^{3+} with spin 2. In addition, the outer shell of (spin 2) Mn atoms are anti-ferromagnetically coupled to the inner shell of (spin 3/2) Mn atoms. To check this we can model with randomly assigned δR_{ij}.

2. Generate graphs for larger, arbitrary n.

3. Test the inductive (analytic) model for minimizing P for graphs of larger n and show stability of large graphs.

It turns out that having a randomized value for J (and thus a random edge length) is a somewhat challenging computational problem (related to a disordered Ising-like spin-glass[32]).

2.10.2 The published model

The model that was published[30] takes the second computational model and extends its generality slightly. The equilibrium structure of an MM is again kept as a set of vertices and an associated edge matrix represented interacting spin centers (e.g. Mn-O-Mn bridges in Mn_{12}-family molecules). The nearest neighbor interactions are the only ones represented in the spin Hamiltonian we will be constructing. The strength of the interactions between spin centers is calculated by length in the edge matrix. Again we will assume an interaction that is positive (ferromagnetic) but now it can be an arbitrary positive number (we allow varying lengths between nodes). Shape deformation is carried out by adding random vectors to the node locations, where the random deformation is Gaussian with a known standard deviation. A deformation roughly resembles the procedure used in Monte Carlo simulations of the compressible Ising model [32]. Further detail of this model will be discussed in section 7.

2.11 HOPG

HOPG is highly oriented pyrolytic graphite, and comes in several grades. This material is typically used for lateral calibration of STMs because it is easy to cleave planes in $\hat{z}$ *in situ* leaving very large (relative to the effective scales of STM measurement) flat terraces and provides a well understood lattice constant (usually the β lattice, the holes in the center of the carbon rings). For this reason it was believed that this would be a good choice for use in STM experiments. Graphite is conductive meaning we would not need to grow a film before depositing our sample, and there

was a well known ligand substitute of Mn_{12}-Ac which also had this ringed carbon structure. It was believed that this would provide superior adhesion and stability on the surface after deposition. It meant only a change of solvent for preparing samples.

Here is what HOPG looks like via STM in Figure 2.7, and as you can see, the surface is very flat and the bright spots (the β lattice) have a known center to center distance making it is easy to calibrate lateral sizes. Unfortunately it is very challenging to shape or recover a tip while scanning over HOPG because of the softness of the surface compared to the tungsten or platinum-iridium tips used for STMs. More of this will be discussed in sections 4 and 5.

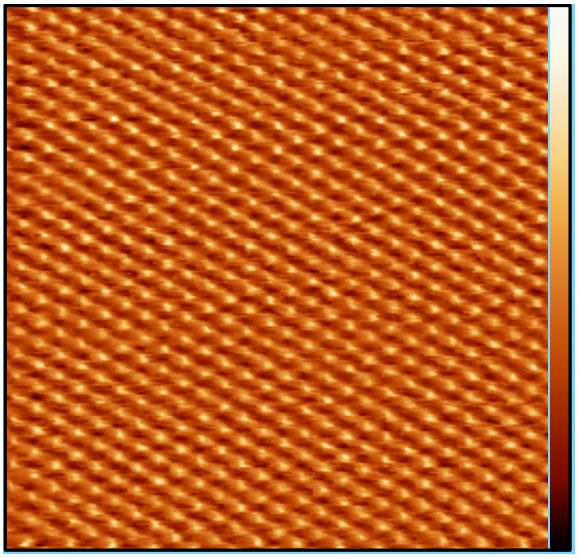

Figure 2.7: HOPG cleaved in UHV. 6.7 nm x 6.7 nm visible area with a total height range of 1.4 Å, taken with a tunneling current of 150 pA at a sample bias of -300 mV. This work was done in collaboration with Patrick Han.

2.12 Cu(111)

Cu(111) is nominally a single crystal of pure Cu with a known crystallographic orientation. This is a very good material for $\hat{z}$ calibration of STMs due to the known step height between terraces as well as the ability to recover usable tip-shapes through field emission from the surface and repeated controlled tip-crashes. This material is not cleaved in vacuum but undergoes repeated sputtering (bombardment by Ar-ions) and annealing (heat cycling up to several hundred degrees Celsius). These techniques will be discussed further in sections 3 and 5. Despite a more involved cleaning process, and being much more expensive this turns out to be a superior sample surface for several reasons. First of all, it is much easier to recover, shape, and quantify tip conditions over Cu (especially when compared to HOPG), and secondly the surface is known to be very reactive increasing the chance of the molecules (or anything else in the chamber) adhering to the surface. Here in Figure 2.8 is a calibration example of Cu(111) .

Figure 2.8: $\approx$ 150 nm x 150 nm, showing four distinct terrace steps of Cu(111) allowing for precise $\hat{z}$-piezo calibration. The tunneling current was 150 pA and the sample bias was -300 mV. This work was done in collaboration with Patrick Han.

3. EXPERIMENTAL METHODOLOGIES

This section will be concerned purely with how to generate samples like those I used and then how to perform the various measurements on those samples similar to the ones I will discuss in later sections. My samples come in two broad categories, powder (or powder in solution) and thin films on surfaces. The powder (and powder in solution) samples consist of micro-crystalline Mn_{12} and a solvent. The measurements fall into two categories also, spectroscopy and probe microscopy (it turns out that these categories are not as distinct as they might appear).

3.1 Sample fabrication

3.1.1 Dip and dry

The older method of sample preparation was to take a known concentration of Mn−12 dissolved in a solvent and use a micro-pipette to place small volumes on a surface and allow the solvent to evaporate (dip and dry), see Figure 3.1. This is the method Seo used and thus my initial methodology as well.

A typical example would be to measure out 1.0 mg of powder (the powder for Mn_{12}-Ac having a molecular weight of 1868.01 $\frac{g}{mol}$ and 100 mL of Acetonitrile (C2H3N) which has a molecular weight of 41.05 $\frac{g}{mol}$, for a solution which is has a 5.35 μMolar density (Figure 3.2. A range of solutions from $\approx 0.1\,n$Molar to 10 μmolar were tested.

These samples, Figure 3.3 were then packed and sent for testing in Japan via UHV-STM or observed locally (by me) via AFM. AFM nominally has the resolution to observe these molecules except that at room temperatures their mobility on the surface seems to be high enough that molecules were never observed except as coffee-stain-ring structures where it is questionable if the molecules were intact.

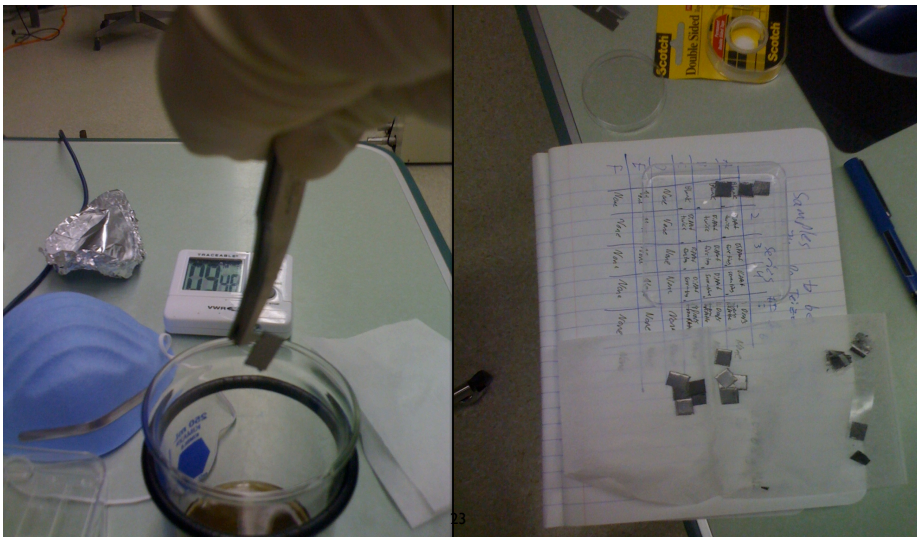

Figure 3.1: Dipping and drying samples for shipment and testing in a UHV STM in Japan. These samples were on exfoliated pyrolytic graphite (which is very hard compared to HOPG) and had droplets of Mn_{12}-Ac in Acetonitrile (CH3CN) added to the surface.

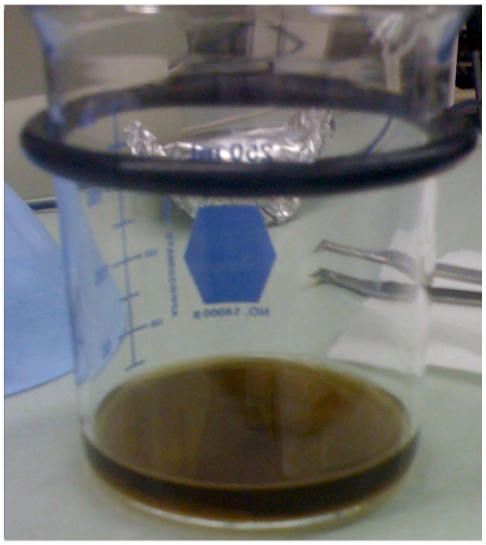

Figure 3.2: An example solution using the older methodology. You can see a uniform, dark, liquid. These solutions required high density to assure that the density on molecules on the graphite surface would be high enough to find *via* STM within a reasonable time. Operating near the saturation point of the solvent meant that care had to be taken to not drop any sedimentation which was present in the solution onto the sample surfaces.

Figure 3.3: Packaging of some samples for shipment to Japan and then testing in UHV STM before my first trip to Japan. This package contained an array of different surface densities of Mn_{12}-Ac and several control samples. Unfortunately there was some miscommunication about the allowable size of samples and all of these were much too large (roughly by a factor of 5), and some combination of dicing these samples to fit within the UHV-STM system and high curing temperatures for the epoxy used to make good electrical contact to the sample holder probably destroyed any useful sample which had survived shipping.

3.1.2 Initial preparation

To prepare a sample for STM we first need a very flat surface and then we need to add our molecule onto that surface in sufficient density that a molecule can be found in a reasonable amount of time but not so dense that the molecules aggregated into 3D structures.

The dip and dry type samples were prepared on graphite. Originally, because we did not have any HOPG. I practiced sample production on pyrolytic graphite (which is very hard graphite due to some covalent bonding between layers resulting from a random grain orientation and other defects) which was mechanically ablated to have locally atomically flat terraces.

Once we used HOPG we could use the 'tape-pull' method of cleaving to obtain a clean, flat surface for our sample. These samples were of a much higher quality.

In both cases, a sample solution was produced and instead of actually dipping the surface into the solution, a micro-pipette was used to add 'drops' of solution onto the surface. To produce thicker films I would place a drop on a surface, allow the surface to dry, and then repeat that procedure.

While using Mn_{12}-Ac I used Acetonitrile as our 'best' solvent, in that it could sustain the highest density of molecules in solution without harming the molecule. Acetonitrile is not a perfect solvent for the micro-crystal however, so a lot of agitation was required to achieve full dissolution. We found that something on the order of $10\,\mu$Molar was the upper limit of solution density for this solvent, beyond which micro-crystal sedimentation could never be stirred into solution.

When I decided to change to Mn_{12}-Ph, on the advice of Dr. Bluemel (a surface chemist who is on the committee for this thesis) after a discussion in my Master's defense talk, I also needed to change solvents for our solution because Acetonitrile

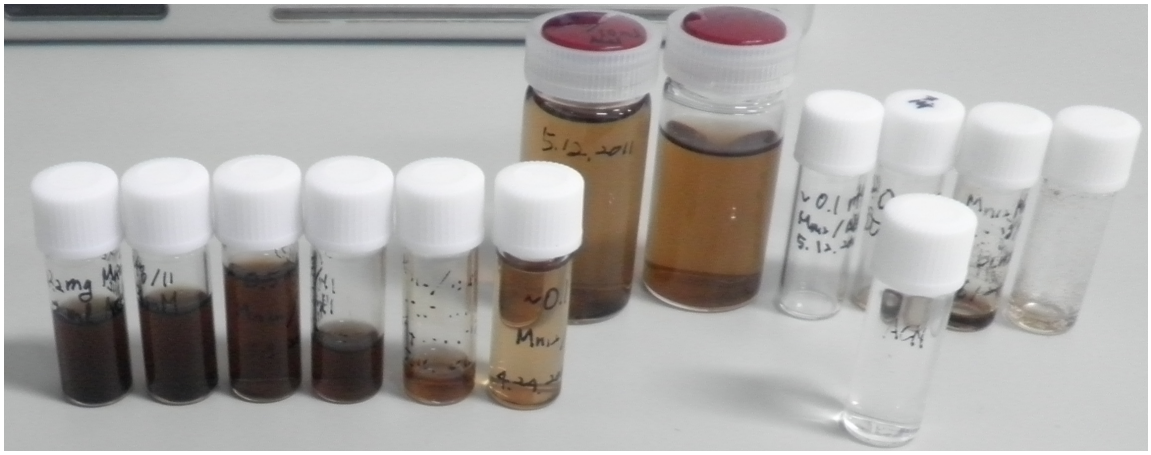

Figure 3.4: This is a series of sample solutions made while doing iterative testing for sample improvement. In particular I was attempting to find an upper bound of solubility of Mn_{12}-Ph in benzene.

would not be a very efficient solvent. I chose benzene after discussing possible solvents with Dr. Zhao (the synthetic chemist producing our molecules), which it happens to be a nearly perfect solvent for the molecule. I never found the upper limit of density in solution for this solvent (see a range of tested solutions Figure 3.4).

As you can see from my testing in Figure 3.5 and Figure 3.6 we obtain a 'coffee stain' like ring from the Acetonitrile and Mn_{12}-Ac solution evaporating most efficiently at the edge of the meniscus and thus having a net flow outwards (carrying our molecule towards the edge). This leads to a large aggregate of our molecule in rings and very sparse coverage inside the rings. For ambient STM where one has good optical access to the sample as the tip approaches the surface this is not a problem. For UHV-STM this means that the tip might come down in a region which fouls the tip, or while scanning we might run into very tall features, fouling the tip. Once we switched to Mn_{12}-Ph and then switched to benzene as a solvent we no longer had a meniscus form on the surface of HOPG because benzene wets very well to the surface. This solved our issue of ring like aggregation entirely by accident.

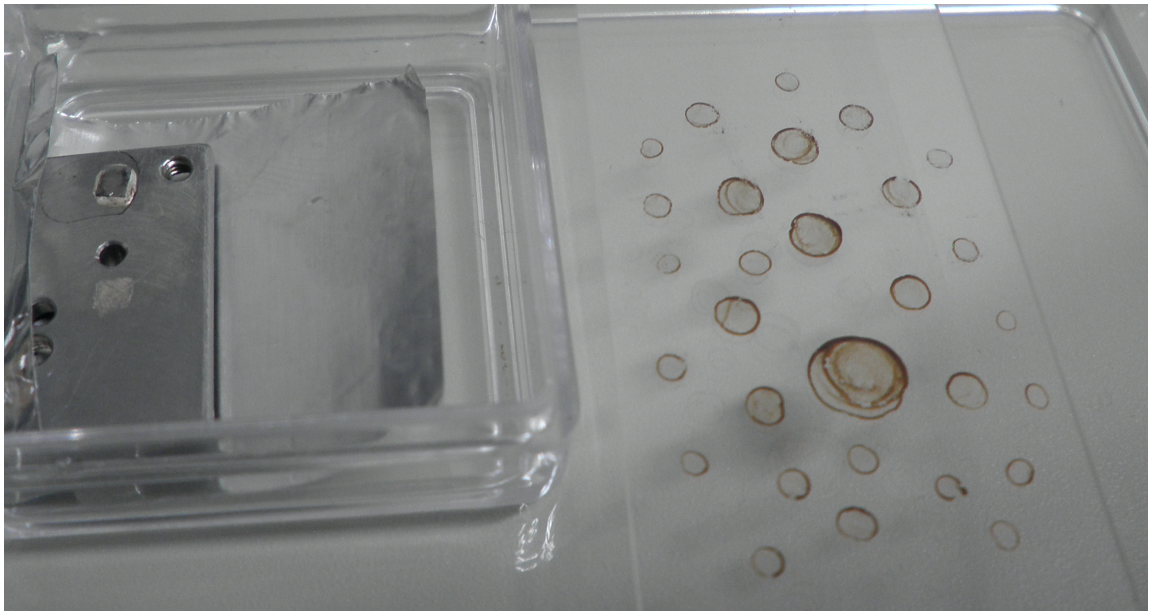

Figure 3.5: On the right in this picture is an example of a droplet produced surface where the solvent does not wet well to the surface, leaving 'coffee stain' rings of Mn_{12} aggregate. On the left in this image is an HOPG sample bonded to an ambient STM sample holder.

3.1.3 Cu crystal preparation

The Cu crystals used were purchased (we purchased 3). In order to use them for the experiment the surfaces required some treatment. Initially Patrick Han and I (who were both using the Cu crystals for different experiments) repeatedly cycled between sputtering Ar^+ at the surface and annealing around 500 C. This brought bulk contaminants in the crystal to the surface (while annealing) and blasted them off of the surface (while sputtering). I will now describe the experimental procedure followed to condition the surface for later sample deposition in Appendix A.

3.2 Vacuum spray deposition

Using the available sample preparation chamber for the STMs we were using (see Figure 3.7), we added a solenoid pulse valve to replace an observation window.

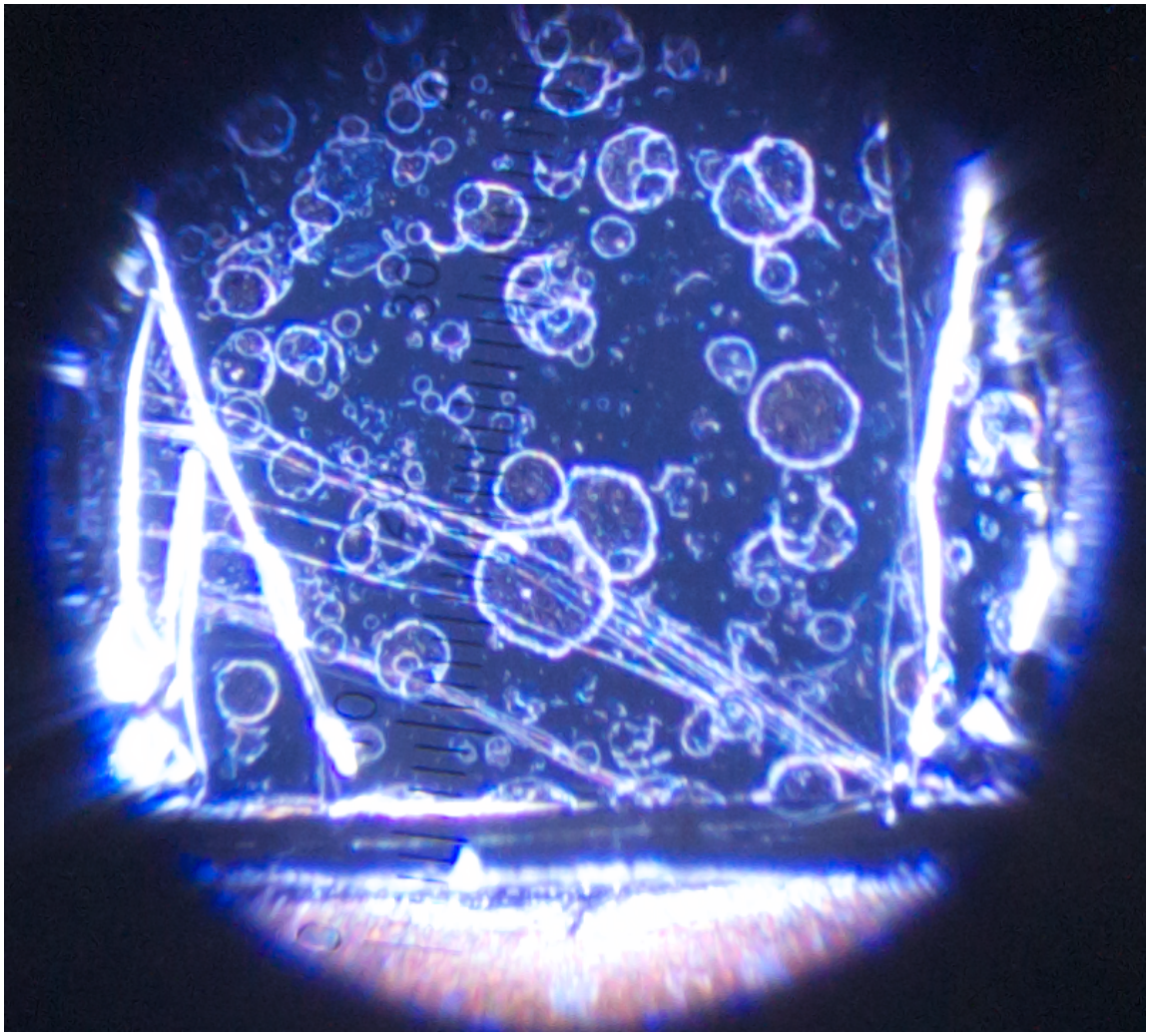

Figure 3.6: This is an optical microscope image 'coffee stain' rings on HOPG under an optical microscope. The bright lines are large vertical steps between graphite planes, and the silver and copper color at the base of the image is the silver epoxy and part of the copper sample holder for UHV-STM.

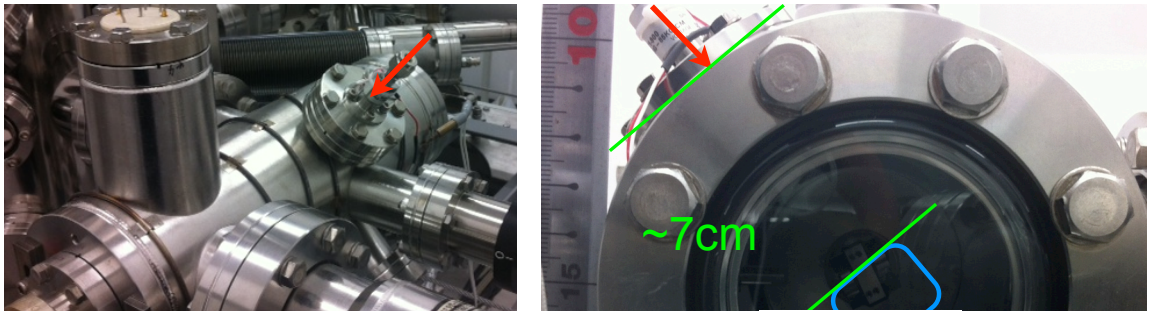

Figure 3.7: Picture of the injector valve assembly installed onto the load-lock chamber of the UHV STM we used for testing. You can see a bar indicating distance between the valve-head and the sample surface.

The preparation chamber was connected to a dry scroll pump and a turbo-molecular pump and could be baked. Using a controlled pulse length to open the injector valve for very short time we could insert very small volumes of our molecule and solvent solution into the chamber. If this is done with the gate valve to the turbo pump left partially open we can maintain the chamber in the molecular flow regime allowing us to use this technique to selectively pump away the solvent molecules more rapidly than the Mn_{12} molecules (see Figures 3.8, 3.9).

To install the spray injector valve, an observation port was removed and the injector assembly added to the preparation/load-lock chamber of the system we were using, to allow for in vacuum transfer of our sample after preparation to the STM. In Figure 3.7 you can see where the injector is located in the system and in Figure 3.10 you can see the mechanical drawing of the injector valve itself. Of particular interest is the 'poppet' which is a plastic or ceramic (we tried both and preferred the plastic) piece and it actually forms the seal face of the valve with the copper flange located below it.

These valves require cleaning and periodic maintenance which was performed in the following way:

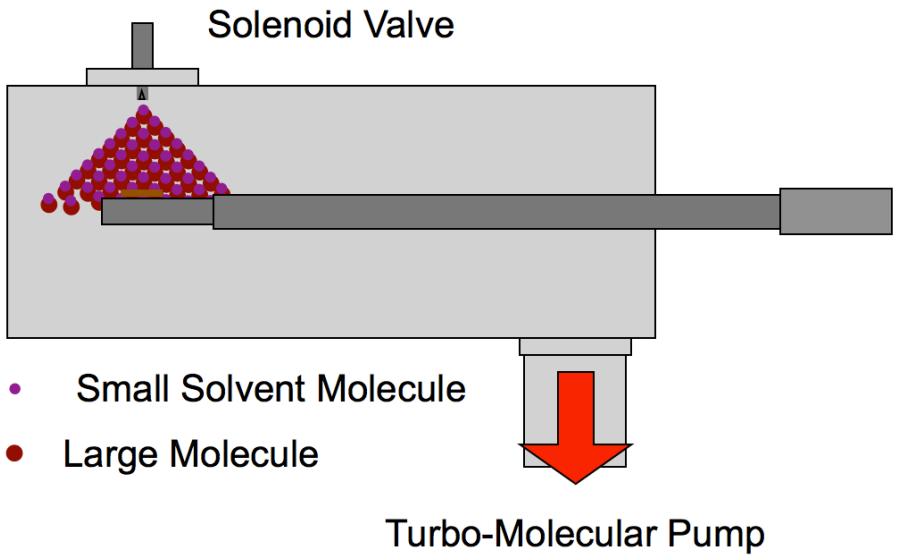

Figure 3.8: Cartoon of a solution being sprayed into a vacuum chamber. The smaller circles are solvent molecules, the larger circles are the molecule we would like to have form a film. This projected cone-path is where we would like to spray our micro-droplets. We know that due to the background pressure of the chamber when the sample is injected that these constituents should be in the molecular-flow regime and thus not a directed micro-droplet-like flow as shown. If, however, we restrict the aperture for injection by including structure for directing the flow we observe micro-droplet formation (and thus possible coffee-stain-rings which we were trying to avoid).

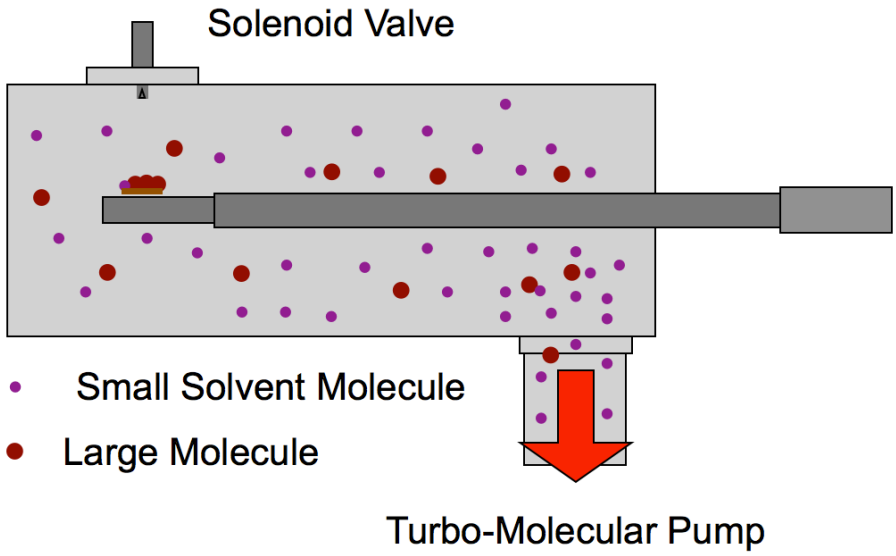

Figure 3.9: Cartoon of differential pumping. The solvent molecules, being less massive are more easily drawn out by the vacuum pump. The more massive molecules have a more classical trajectory towards our sample (though they also diffuse into the chamber and are pumped away). The smaller circles are solvent molecules, the larger circles are the molecule we would like to have form a film. The dark grey rod is a manipulation arm. The down-ward pointing arrow is the direction to the pump for the chamber.

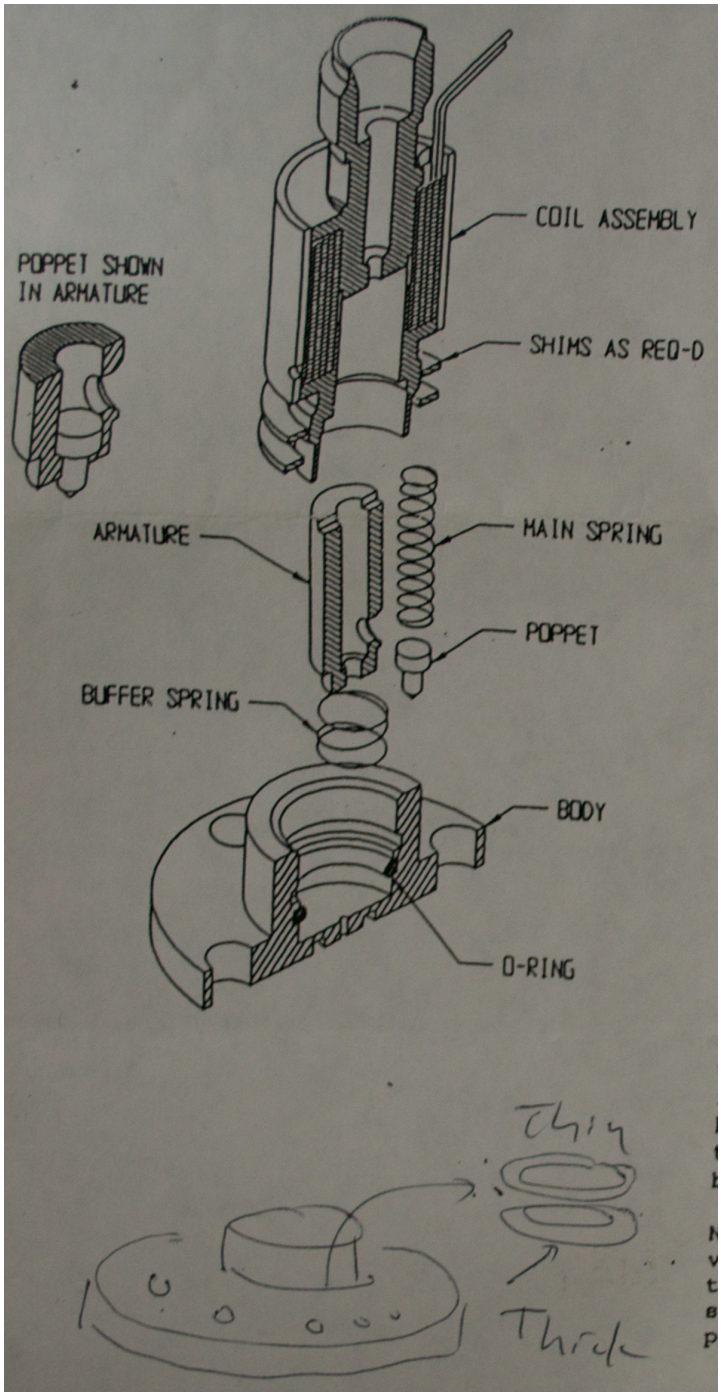

Figure 3.10: Schematic diagram of the pulse valve, supplied by Parker Valves for performing maintenance on the injector valve-assembly

Between uses benzene was flushed through the system by rapidly injecting it into rough vacuum (with the turbo pump not spinning). As much as 50 mL of benzene would be flushed into the chamber and pumped back out by the roughing pump. Since benzene is such a good solvent this should have been more than sufficient to clear the system of any Mn_{12} sedimentation in the valve.

About as frequently as the vacuum system was baked out the valve would be removed from the system and deconstructed. The internal components would be sonicated, first in benzene and then ethyl alcohol. Then the system would be re-assembled. This led to a problem; there is a permanent magnet which provides the force for opening the valve, and repeated sonication of this piece randomized its magnetization. Once this was discovered that piece was no longer sonicated.

A range of valve open times and frequencies of injection were tested in a small vacuum chamber. In the end we settled on $3\,ms$ open time and varied our number of injections. Here you can see the difference in concentration on the surface between a single injection and ten injections of the same solution in Figure 3.11.

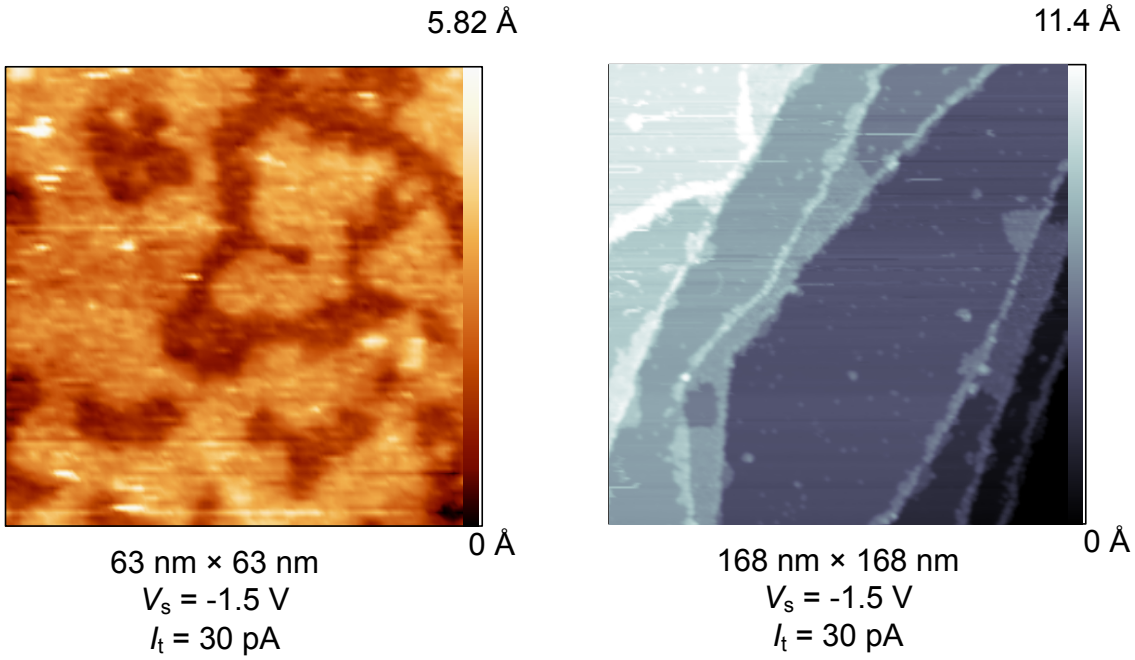

Figure 3.11: Images of variability of film thickness. On the left is ten injections of 3 ms each. On the right is a single injection for 3 ms. These images are not of equivalent size. The left image is very hard to generate because the tip continually picks up molecules from the surface and thus the tunneling gap-distance is very unstable.

3.2.1 Iterative testing and sample improvement

A conscious choice was made to begin iterative testing of samples on instruments which could not accomplish the experimental goals but which could provide faster turn around times for feedback on sample quality. The procedure was to make a sample in the test-chamber, then use an optical microscope to ensure there were no obvious defects as seen previously in Figure 3.6. If the sample passed this stage, then SEM-EDX, Figure 3.12, was used to chemically map the sample surface. The film deposited was so thin that it was unlikely to generate a strong response unless we looked for oxygen (which should not be in abundance except from our sample). If the sample still had no obvious defects AFM was used to look for smaller aggregates on the surface or other sample defects, Figure 3.13. A sample using the parameters which went through all of these steps would then be suitable for use in UHV-STM. Finally, after observing samples at low temperature via STM, we could narrow the parameters for producing optimal samples for our end-goal of observation below 3 K. We will look at STM results in the later sections.

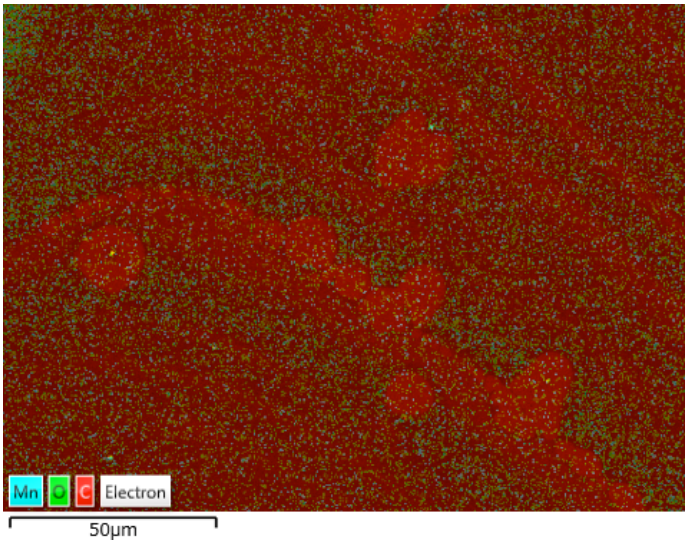

Figure 3.12: On the left is a four layer composite surface map in false color. This is a sprayed surface on a thin film of Au on mica which had been flame annealed.

3.3 SPM

Scanning probe microscopy (SPM) came into existence with the creation of the STM at IBM-Zurich, reported in 1981[**?**], which received a Nobel prize in physics in 1986. An STM functions by measuring tunneling current across a gap (or tunnel junction) and uses piezo-electric materials for spatial manipulation of the location of an atomically sharp metal tip which is held a few Å away from a surface which is held at some bias voltage (see Figure 3.14).

From there the field expanded, so that now there are dozens of SPM techniques across a wide range of sample conditions and exploiting distinct physical interactions. The common elements of these techniques are that they all require piezo-electric actuators (in one or more dimensions) for very fine motion control, and they use a raster-scanning technique to build 2D maps with a false color third dimension. SPM techniques routinely achieve sub-nanometer resolution beating the optical diffraction

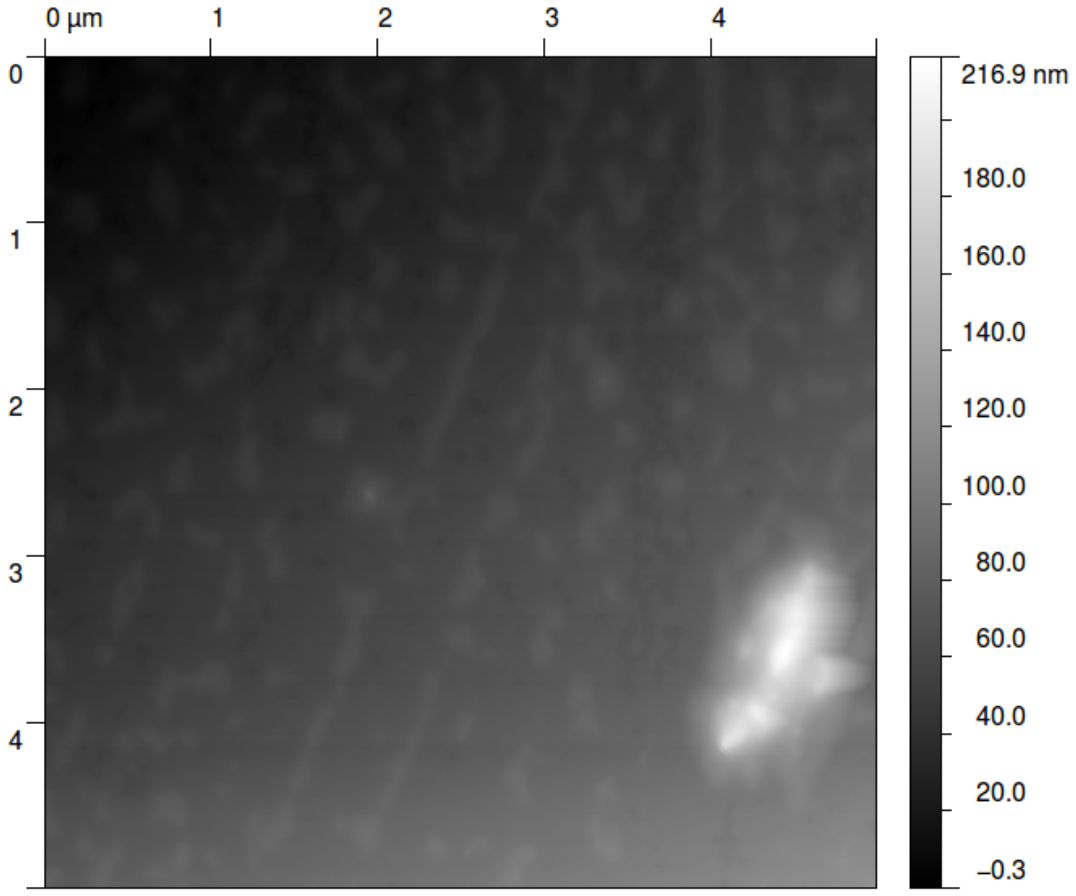

Figure 3.13: Here we see a rejected sample discovered at the AFM stage of the process. This sample was rejected due to the very large feature (relative to the scale of STM images) which was found (the white area of the image).

limit by 4 orders of magnitude. The two SPM techniques I used were atomic force microscopy (AFM) and scanning tunneling microscopy (STM).

3.3.1 STM and LT-STM experiments

STM operates by maintaining a tunneling current, and using that to describe a 'height'. This means of course that our sample needs to be conductive (or at worst a conductive surface with a very thin insulating top layer). The tunneling current can be determined in the following way:

$$I_{tunneling} = \frac{4\pi e}{\hbar}\int_{-\infty}^{+\infty}((f(E_f - eV + \epsilon) - f(E_f + \epsilon))\rho_S(E_f - eV + \epsilon)\rho_T(E_f + \epsilon)|M|^2)d\epsilon \tag{3.1}$$

Where ρ_S and ρ_T are the density of states in the surface and tip respectively.

M is a tunneling matrix element depending upon electrons tunneling to the same or a lower energy level state. ψ is the sample wave function. χ is the tip wave function. S is a distance from a surface (height z, with z=0 at the sample surface):

$$M = \frac{\hbar^2}{2m}\int(\chi * \frac{\delta\psi}{\delta z} - \psi\frac{\delta\chi*}{\delta z})dS$$

f is the Fermi-Dirac distribution function (because we are using electrons as our probe), and is described in the following way:

$$f_i = [e^{\frac{\epsilon_i - \mu}{kT}} + 1]^{-1}$$

Where k is the Stefan Boltzman constant, T is the temperature of the system, ϵ_i is the energy of a single-particle state, and μ is the total chemical potential which for our system is a constant, and $\hbar$ is Plank's constant divided by 2π.

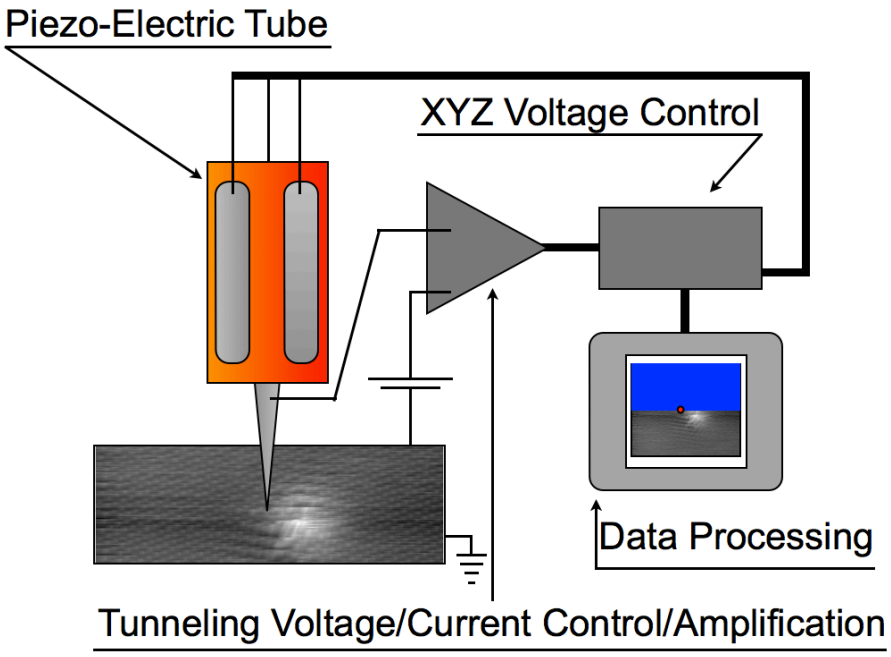

Figure 3.14: Cartoon of an STM. You can see the piezo-electric motion controller, the electronic feedback controls, and the bias voltage held between the sample and the tip.

We can see a schematic of STM operation in Figure 3.14. Something we should take away from the above integral is that as we lower our temperature we get a finer energy resolution for matching wave functions reducing the noise of the system. STM can be operated in two fundamental modes, constant height which returns tunneling current as the $\hat{z}$ value and constant current which returns a map of the local density of states under the tip.

Because of the uncertainties in apparent lengths and heights in STM images calibration is crucial (and temperature dependent). Before beginning any experimental work it is important to calibrate the instrument at the temperature you intend to operate at.

HOPG is the usual choice for lateral calibration. A small piece of HOPG (around

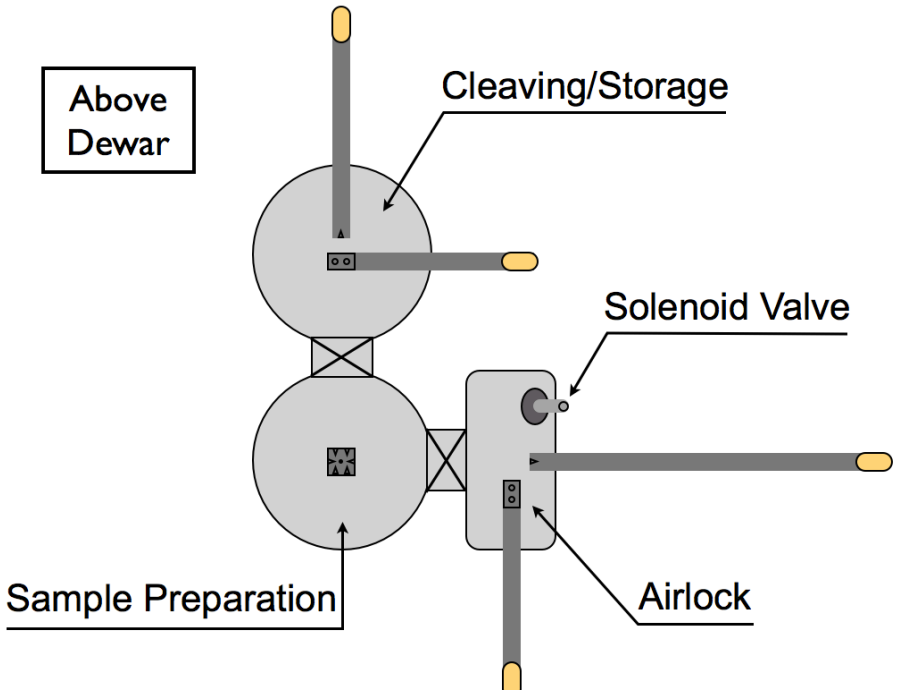

Figure 3.15: Cartoon of a typical set of UHV chambers for preparing a sample and moving it to an LT-STM for observation, including the supporting equipment.

1 mm x 2 mm is attached to a sample holder by some conductive epoxy (usually silver paste). A 'post', which is a metal cylinder with a diameter smaller than the surface it rests on and a large aspect ratio (it is usually approximately 1 cm in length) is epoxied to the upper surface of the HOPG. The HOPG sample with post is transferred into the system, taking pains to maintain good vacuum and not introduce contaminants into the system. The sample is then held in front of a mobile armature with a wedge-tip and is carefully used to push just above the base of the post. This causes the HOPG to cleave along some plane below the epoxied surface. If a clean cleave is not achieved (flakes hang on or the wedge touches the new surface) a different calibration sample must be used. This fresh surface is then moved to the STM and imaged promptly. An example of this was seen previously, see Figure 2.7.

Calibration in $\hat{z}$ can be done in several ways. Since we were using Cu(111)

crystals anyways, we had a convenient $\hat{z}$ calibration method of measuring the step height between terraces. To prepare the Cu surface, we would anneal the crystal at approximately 500 C (as determined by an IR-Pyrometer through an observation window) and then sputter argon ions against the surface, then repeat the process with a lower temperature and a shorter sputtering interval. This process was repeated approximately ten times, followed by one last annealing phase. The temperature and time intervals annealing can change the frequency of terraces on the surface. The sputtering is largely a cleaning step to remove impurities which move to the surface of the Cu or were introduced by the background in the chamber. An example calibration surface was shown previously, see Figure 2.8. Cu also offers us a different method of calibration. We can use known common contaminants like CO molecules on the surface which have a known apparent size for given tunneling conditions. This will be discussed again in later sections.

3.3.2 AFM

Atomic force microscopy can be done several ways. The most common techniques are 'tapping mode' and 'contact mode'. Contact mode is exactly what it sounds like, the tip approaches a surface and then applies some force into the surface deflecting the tip. Contact mode works best with very hard surfaces and the measured feedback is usually the force required to keep the tip in some constant position. Tapping mode is used to overcome some of the problems inherent to contact mode's requirement to drag the tip across a surface. First the tip does not need to come in contact with the surface but only come close enough for Van der Waals forces to be attractive, though tapping mode can be done with an amplitude large enough to guarantee repeated intermittent contact with the surface. The tip is driven with a known vibrational frequency at or near the resonance frequency for the tip and the deflection from the

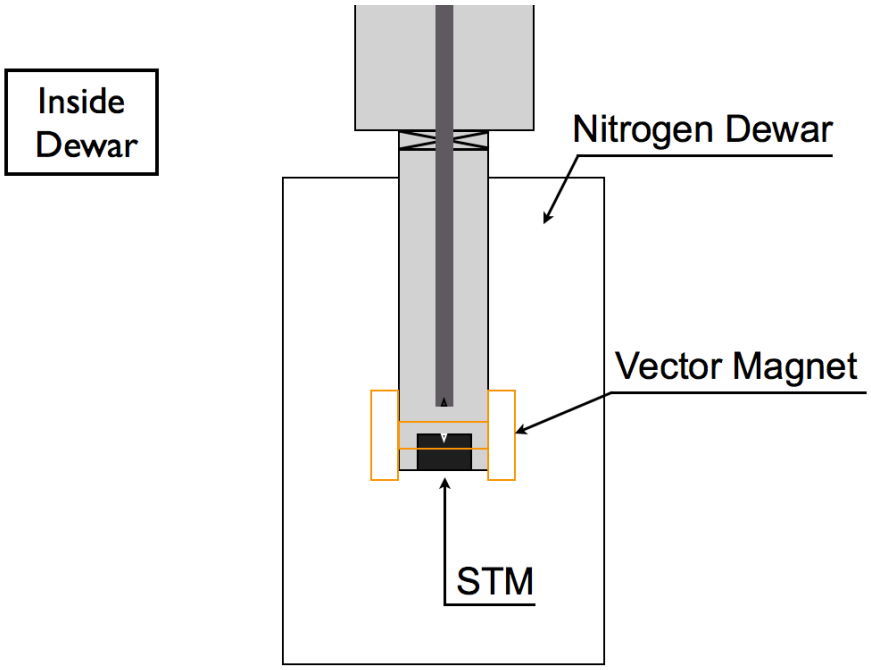

Figure 3.16: Cartoon of the STM and vector-magnet coils in a dewar, located physically underneath the top chamber in Figure 3.15.

surface interaction causes phase shifts in the oscillation (as well as briefly changing the amplitude of oscillation). Tuning between contact and non-contact tapping mode is accomplished by changing the driving frequency from below to above the resonant frequency for the tip (changing the amplitude of oscillation from the order of tens of nanometers to the order of single nanometers. We can see a schematic of an AFM in Figure 3.17. AFM can be used in a very broad set of conditions and on nearly any sample. The sample need not be conductive.

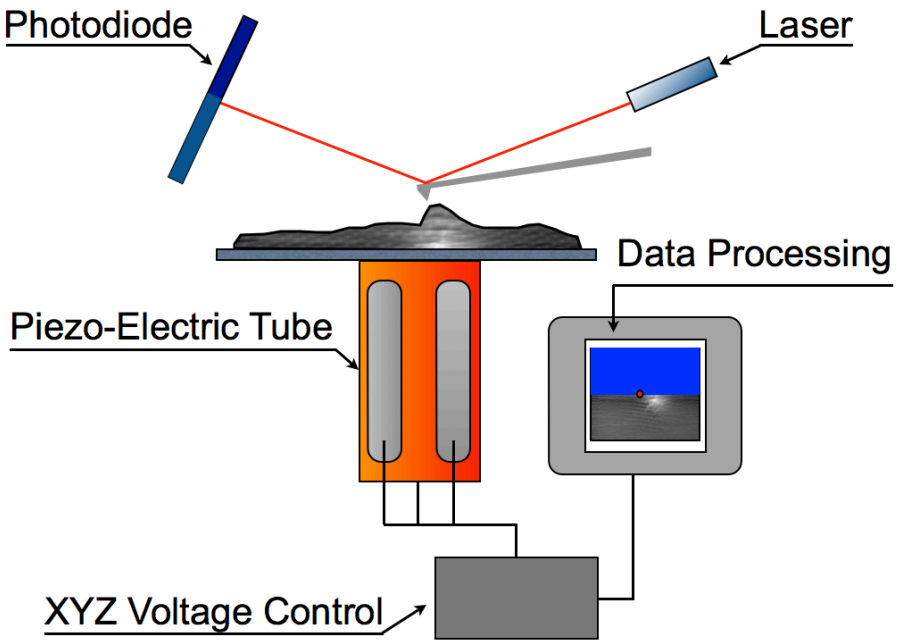

Figure 3.17: Cartoon of an AFM. You can see the piezo-electric motion controller, the scanning tip, the incident laser beam and its refection path, the photo sensor detecting the beam oscillation, and the feedback electronics.

3.4 SEM and EDX

Scanning electron microscopy is similar to SPM in that a probe is rastered across a surface to produce a false color 2D map; though as the name suggests, the probe is an electron beam, a beam which has been highly confined and whose energy is known. These primary electrons penetrate the sample surface and excite secondary electrons and x-rays from a volume of the material under the beam. Typically one uses secondary electron intensity as a map of surface topography. The surface needs to be conductive or charge builds up and begins to distort the image (and probably destroy the surface from local heating). Most secondary electrons remain in the bulk of a sample, and tilting a surface is a simple way to increase the number of secondary electrons that escape. A schematic SEM can be seen in Figure 3.18 and in this case there is an x-ray detector which can be moved to a fixed 'working distance' from the surface. By knowing the initial beam energy a map of the x-rays emitted can be classified against known emission spectra, and the intensity versus beam energy and collection time can allow you to estimate abundance of the elements detected by the intensity of emission. This is known as energy dispersive x-ray spectroscopy (EDX), and if measurement times are high and films are thick, can be a very accurate method of mapping a surface by chemical location. Some examples of these data will be shown in later sections.

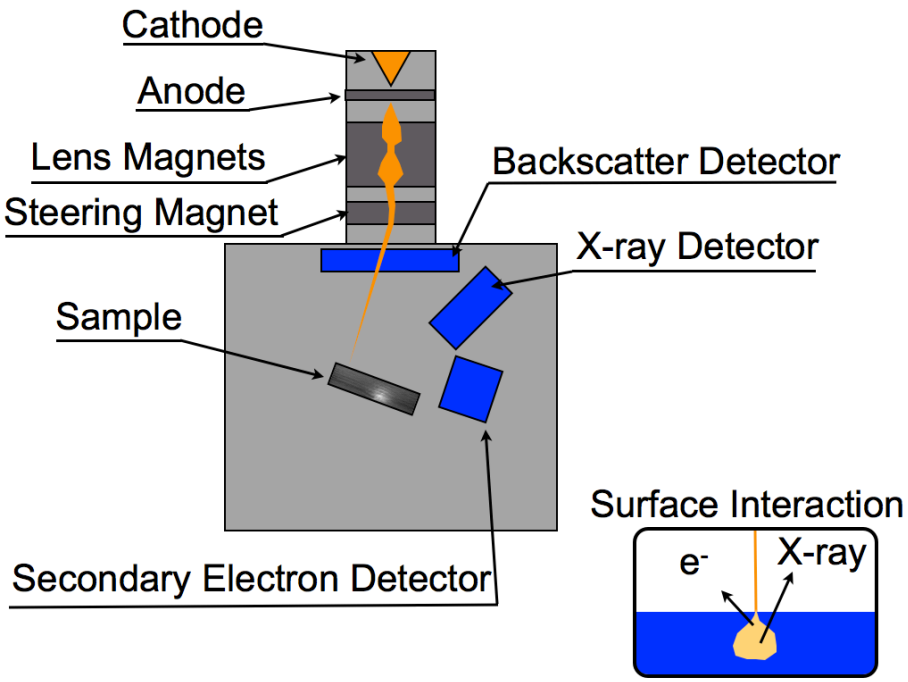

Figure 3.18: Cartoon of an SEM that might be used for EDX. You can see the electron-beam creation and collimation, steering magnets, a sample stage and stage motion controls, and then secondary electron and x-ray detectors.

3.5 SQUID magnetometry

Superconducting quantum interference device (SQUID) magnetometry involves a superconducting loop with at least one constriction, called a Josephson-junction and a known applied magnetic field (which can be altered). SQUID measurements can be taken in DC or AC mode. DC SQUID relies on measuring a bias voltage across the loop and a symmetric set of two junctions and the applied magnetic field biases the current direction in the loop. These Josephson junctions behave with the DC Josephson effect and have a diode-like behavior with a critical current, and exploiting these two things the voltage bias becomes dependent on the magnetic flux through the loop (so long as the input current is always above the critical current of the junctions)[35]. This is seen in Figure 3.19. AC SQUID relies on the AC Josephson effect and requires only one junction in its loop. Changes in frequency from the driving current are measured and attributed to a change in inductance which is related to the magnetic flux through the loop[36].

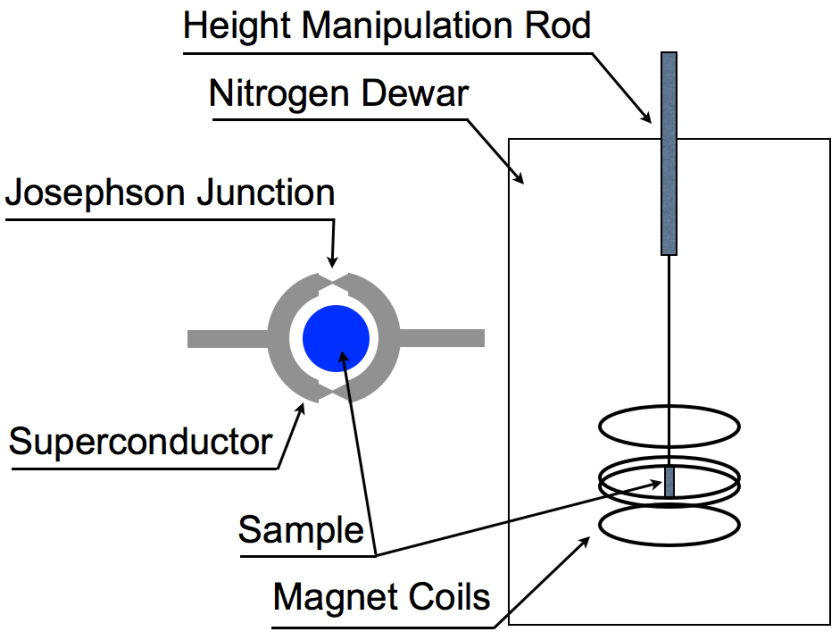

Figure 3.19: Cartoon of a SQUID magnetometer with an inset diagram of the detector loop and josephson junction.

4. EXPERIMENTAL STUDY OF MN_{12}-FAMILY MOLECULAR MAGNETS IN ISOLATION WITH HIGH SPATIAL RESOLUTION

4.1 Background experiments

As the previous sections indicated, a series of background experiments were conducted in an effort to produce high quality samples for low temperature study in more detail. Here are some of the key results of the background experiments.

4.1.1 SQUID

With Mn_{12}-Ac we performed a lot of SQUID experiments, but the key result is Figure 4.1, where you can see that above the blocking temperature (roughly 3 K) there is no hysteresis observed and below the blocking temperature we observe hysteresis and the vertical steps which are the indicators of thermally assisted spin-tunneling, the hallmark behavior of single molecule magnets.

For Mn_{12}-Ph, most of our experiments were performed in this range of $4.0 \leq T \leq 10K$ and so I will show curves at 5 K and 10 K , Figures 4.2, and 4.3 respectively, (both are above the blocking temperature for the molecule, and so no hysteresis is expected or observed).

You can see from these figures that in the temperature regime in which most of our testing was conducted the molecules maintained their paramagnetic (actually super-paramagnetic) behavior.

Further SQUID testing was going to be pursued but instrument availability and reliability became an issue. Since the only information we felt compelled to try and find was a more precise location of the blocking temperature for our molecule it was deemed unnecessary to continue.

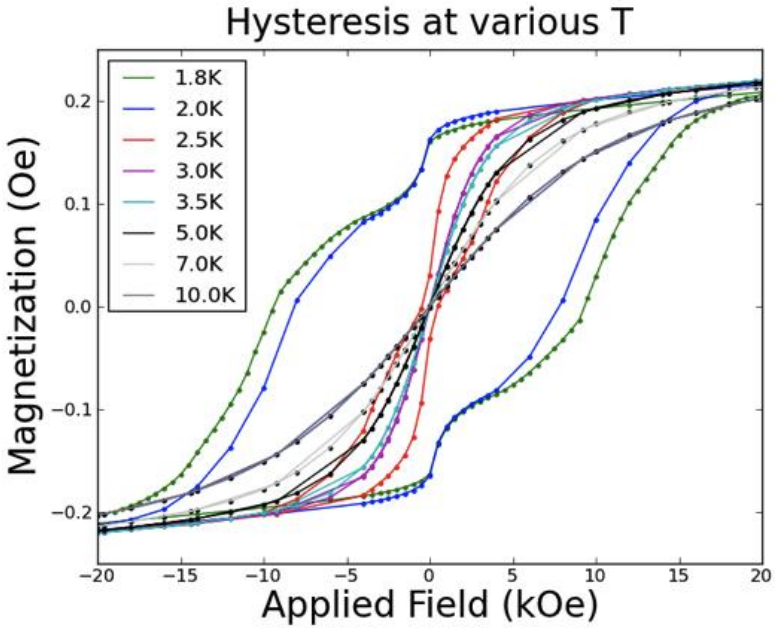

Figure 4.1: Hysteresis at various temperatures plotted with respect to applied field for a micro-crystalline powder sample of Mn_{12}-Ac.

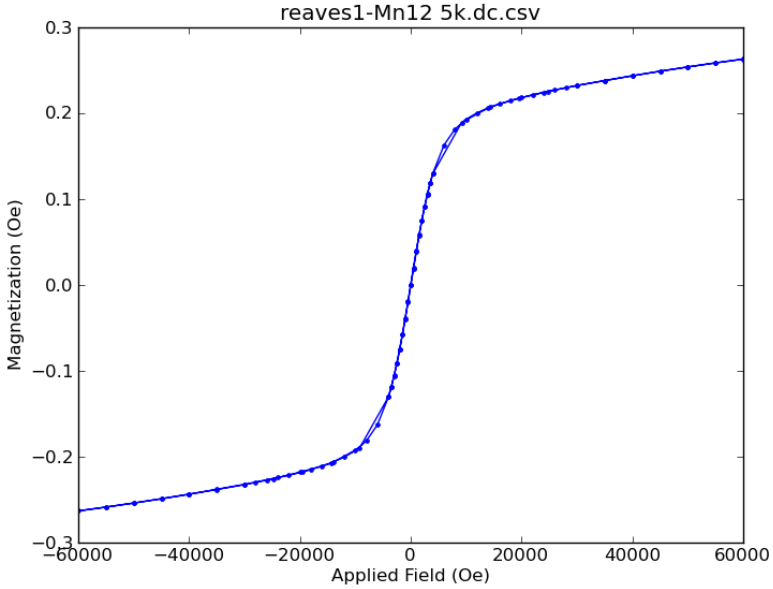

Figure 4.2: Magnetization plotted with respect to applied field at 5 K for the same micro-crystalline powder sample of Mn_{12}-Ac as shown in Figure 4.1.

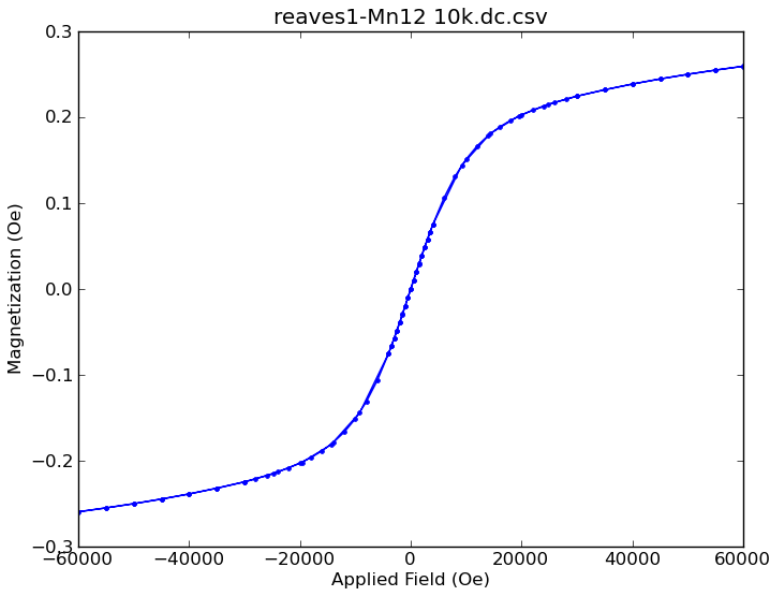

Figure 4.3: Magnetization plotted with respect to applied field at 10 K for the same micro-crystalline powder sample of Mn_{12}-Ac as shown in Figure 4.1.

4.1.2 Ambient STM

The early STM work was done with a VeeCo/DI NanoScope II, SPM Figure 4.4 which was very simple to use compared to the vacuum systems but lacked some of the precision of the more difficult to use instruments. Testing various depositions produced results which were convincing enough (Figure 4.5) that we could justify the time and expense of using the more complicated systems.

Ultimately, ambient STM was not convincing enough in its results for us to rely upon it for our purposes though it is the closest analogue to our experiment which could be performed outside of a UHV chamber and as such was an excellent method of validating sample preparation techniques. There were many factors which make it not-suitable for the kinds of careful investigation we were intending (aside from our inability to do low temperature measurements in a controlled magnetic field with the

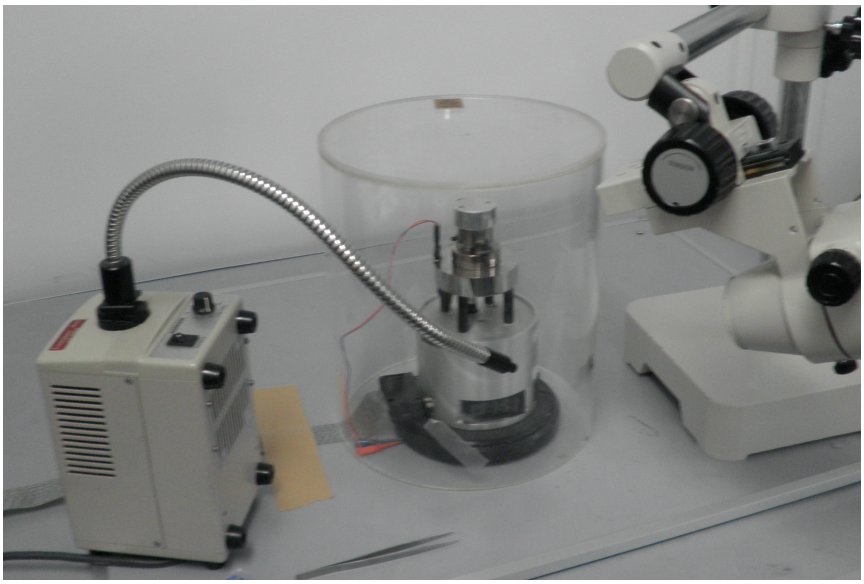

Figure 4.4: Picture of a Digital Instruments NanoScope II configured for ambient STM or STM in ionic solution (which requires a more specialized sample holder than shown). In addition to the SPM you can see a light and a microscope for performing the coarse approach (by hand) as well as an enclosure for the instrument itself.

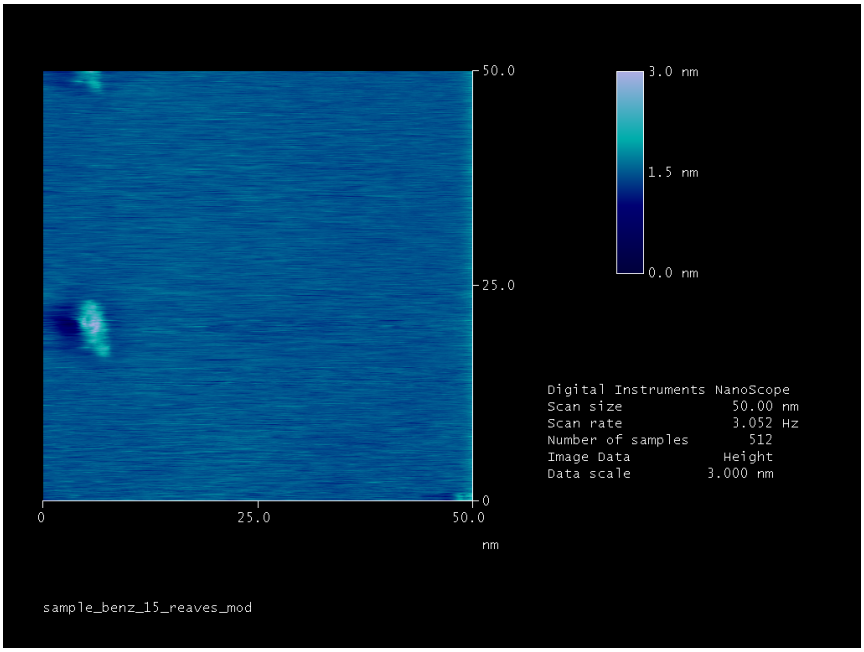

Figure 4.5: Example ambient STM image of a sample with a dilute solution of Mn_{12}-Ph in benzene on HOPG. Isolated molecule-like features are seen.

instrumentation we had available). For an ambient STM, tip shape is much harder to quantify (and the shape is less stable), contamination is more difficult to control, and energy resolution is poor at such high temperatures. In addition to all of that, any STM is significantly more difficult to set up, use, and change samples (or tips) while testing large batches of samples with different parameters than similar SPM techniques (*e.g.* AFM).

4.1.3 AFM

AFM was used as a surrogate for STM testing with a faster turn around speed for discarding poor samples. The samples produced needed to be 'good' on the scale of hundreds of nanometers and not suffer from sharp step-like features or contamination introduced in the production process. AFM resolution is high enough that we could validate the quality of samples for STM without having to take the time to break vacuum and without the need to worry about the condition of our probe tip. AFM does suffer from some of the same validation issues as ambient STM, namely our inability to strictly control (or measure) contamination. The method used to reduce this effect was to measure samples quickly after production.

The first figure 4.6 shows the importance of where one's tip lands on the surface for producing quality samples. If the tip had been over the sheared edge in the lower left which was peeling back from the layers below it (a feature which was not obvious without the aid of the microscope the camera was mounted on) any STM tip would have crashed into the surface and become fouled. In the next image, 4.7 we have the same surface now under the AFM we see other indications of the surface being poorly cleaved. The blurry diagonal line is probably a grain-edge which is exfoliating from the remaining HOPG.

In Figure 4.8 we see a surface which has many terraces and steps, but the terraces

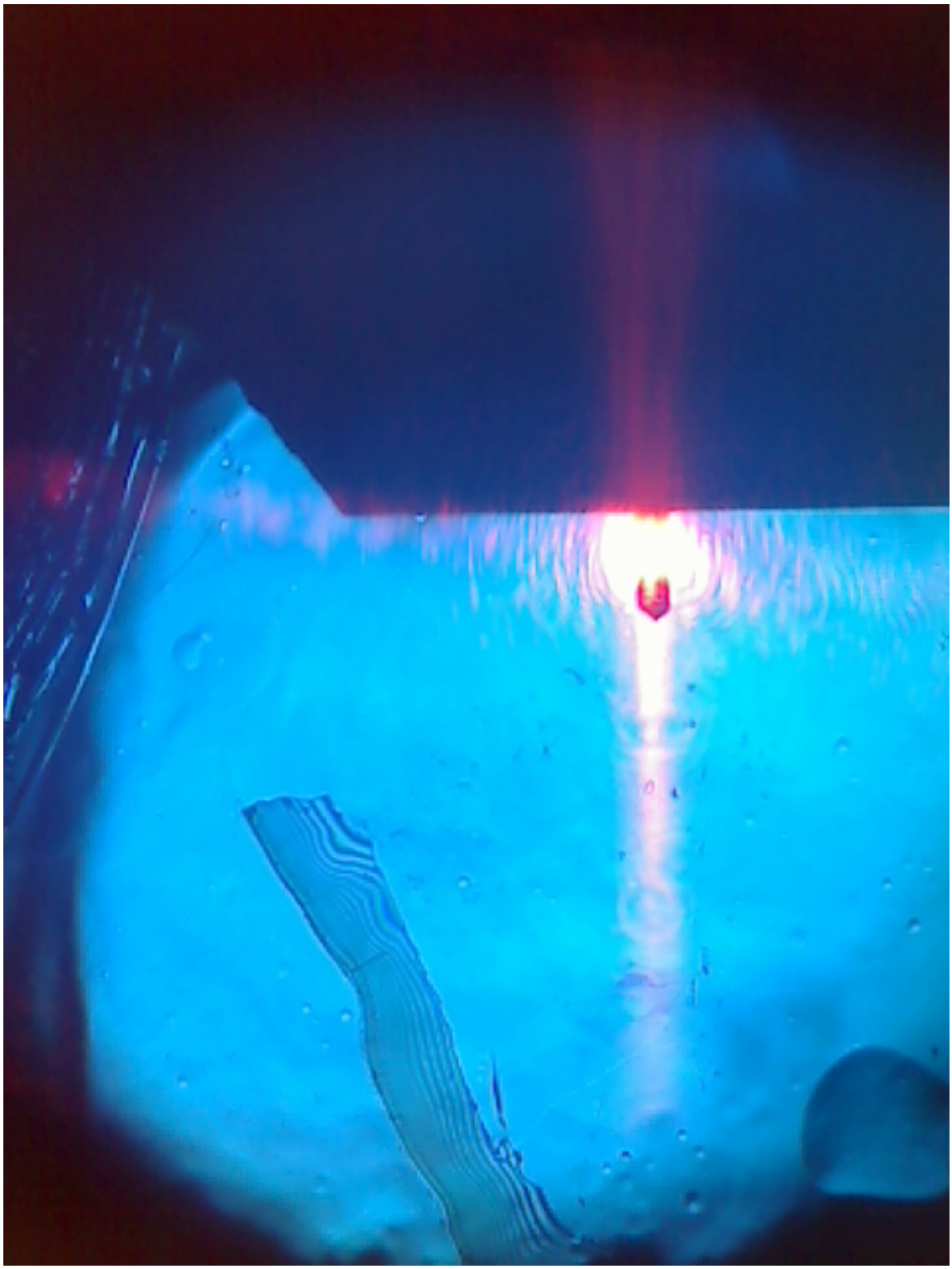

Figure 4.6: Optical microscope image of a surface being scanned by AFM. This HOPG surface is atomically flat in many regions, but at the macro-scale you can see there are obvious surface defects even after cleaving the sample.

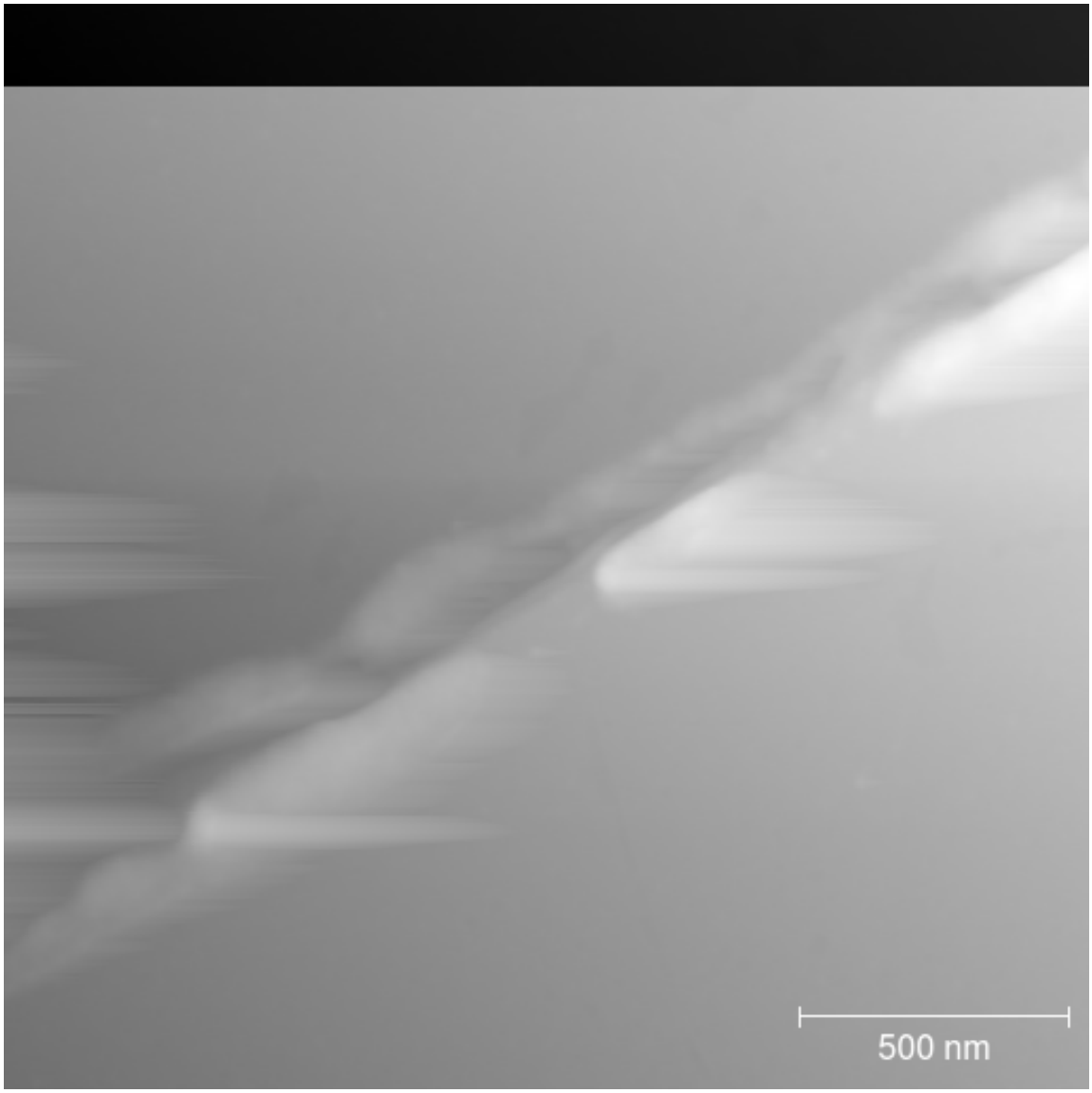

Figure 4.7: AFM image of the sample surface from Figure 4.6, the surface was seen to be flaking (the diagonal blurry lines) and would be rejected from further processing.

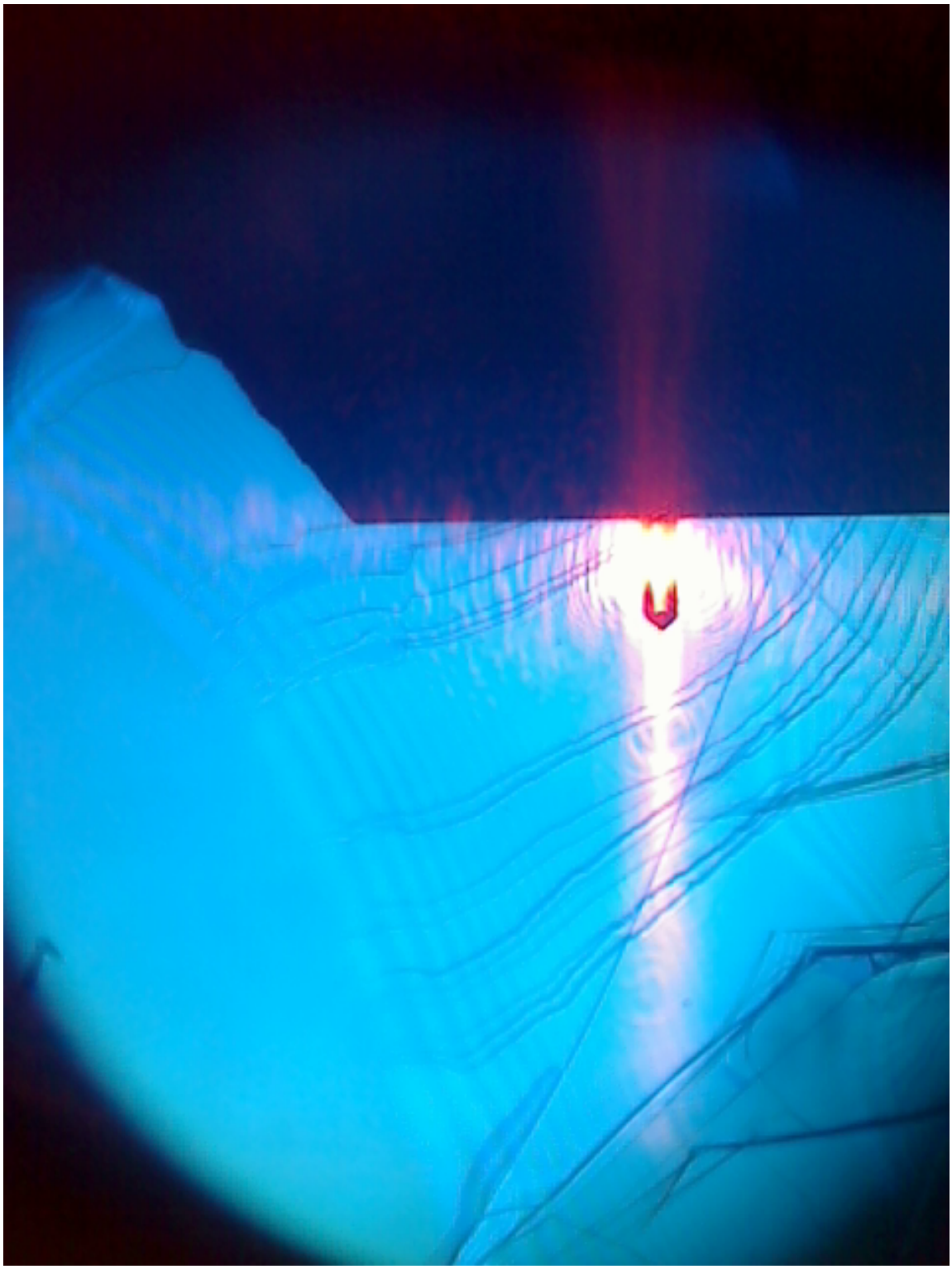

Figure 4.8: This is an optical image of an HOPG surface being scanned by AFM. At first glance this might appear to be a sample to be discarded, but the terraces visible in the image are actually very large on the scales an STM operates at.

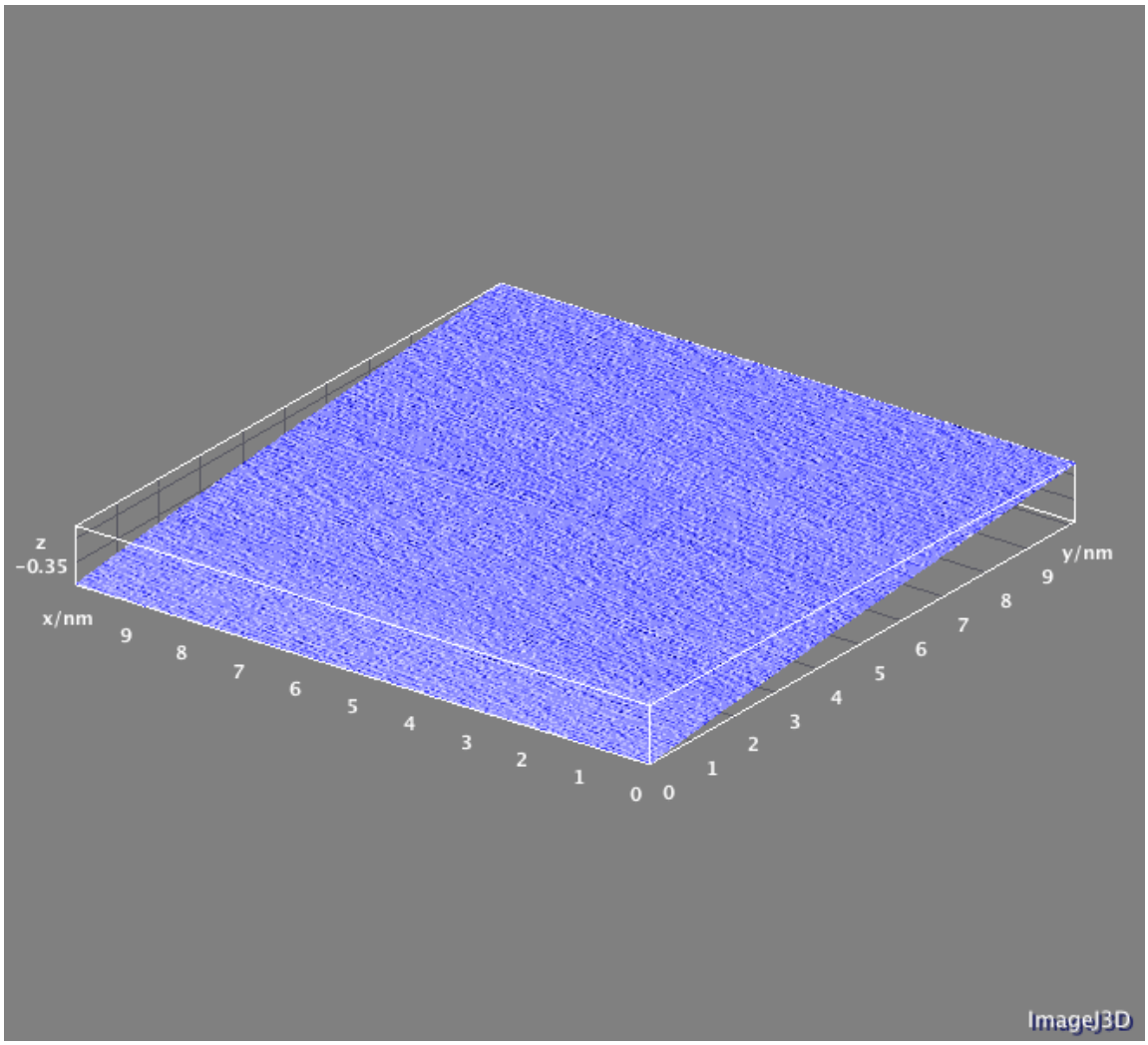

Figure 4.9: This is an AFM image of the sample in Figure 4.8. You can see a very flat plane (though it does have a slope) with perhaps some very small corrugation of the surface (which we would expect on HOPG). This figure is 10 nm x 10 nm x 0.35 nm and is much more representative of the scale we are interested in.

are actually very large for the scales of AFM or STM probes and so we need to then look at Figure 4.9 to see a picture at the relevant scale to judge the sample quality. This sample would pass the AFM validation stage of testing. There were no large surface defects, and the sample was locally very flat and contaminant free.

From this we can see the progress in improving surfaces but it is not obvious if there are Mn_{12} on any of these surfaces because at room temperatures the molecules are almost certainly too mobile on the surface to image even though AFM could technically achieve the required resolution (and ambient STM did seem to localize isolated molecules). So we would need some way of chemically mapping the surface to continue validation (or rejection) of samples before proceeding to UHV trials.

4.1.4 SEM-EDX

Scanning electron microscopy with energy dispersive x-ray spectroscopy allows us to chemically map a surface by looking for x-ray emission peaks after being bombarded by an electron beam with a known energy. This testing would certainly be destructive for our samples and is also very slow, so it was the last step in pre-UHV validation.

To make SEM-EDX measurements, we would follow the same procedure for SEM measurements, and move our stage to a working distance (dictated by the instrument) from an x-ray detector. The software for the system we used then would take over control of the SEM, and allow us to specify scan times, scan size, and beam energy. We could then tailor our search for specific energy ranges (which dictates penetration depth into the sample) and scan times (longer times allowing for detection of lower abundance elements) to our needs. Because it is well known that typical SEM beam-energies penetrate microns into a surface, and our films are less than 10 nm in thickness, we would need a signal 100 times stronger than the background noise (or

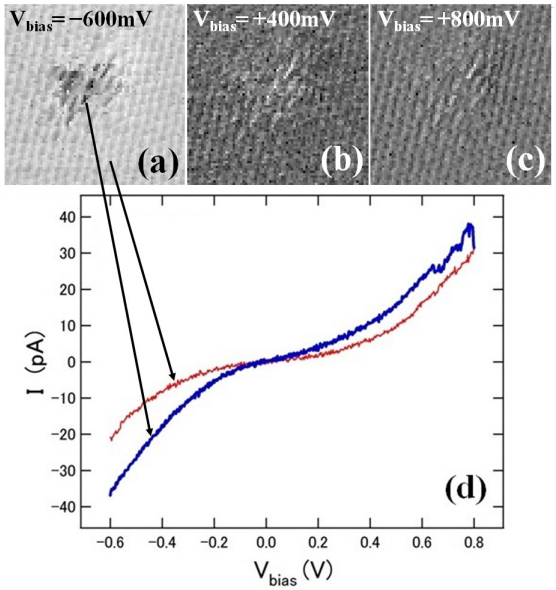

Figure 4.10: Two-dimensional current mapping obtained at a location including an isolated object at three different bias voltages, $-600\,mV$ (a), $+400\,mV$ (b), $+800\,mV$ (c) Tunneling current (pA) with respect to bias voltage (V) measured at two locations marked by arrows (d). Scan size: $4.5\times4.5\,nm^2$. STM chamber temperature: $\sim4.9\,K$.

more) to be able to detect our sample. Luckily for us, the molecule we are using has a high oxygen content and the sample surfaces and SEM environment do not. Oxygen has very strong x-ray peaks even at relatively low incident beam energies (*e.g.* < 5 keV). This allowed us to see aggregations of our molecules on surfaces (Figure 3.12 after spray deposition and approximate film thickness (by looking at the abundance of oxygen versus the area and assuming a close-packed 2D island growth mode).

4.2 STM

4.2.1 On HOPG

This sample were produced by dropping a small ($\sim 1\,\mu$l) droplet of $\sim 0.2\,mM$ solution of Mn_{12}-Ph in benzene via micro-pipette onto freshly cleaved (in ambient conditions) HOPG which had been diced and bonded via silver epoxy to STM sam-

ple holders. After drying, the samples were loaded into the LT-STM system for observation at $\sim 80\,K$ and $\sim 4.9\,K$. Once a molecule was located on the surface the tunneling conditions were altered to acquire, in the range of $\pm 1\,V$, tunneling current vs. voltage (IV) data for each point in a 128×128 pixel grid in a given topographic region near several molecules at $\sim 4.9\,K$ (see Figure 4.10).

In Figure 4.11 we see a representative result from this experiment. This method of sample preparation, however, did not provide homogeneous films of isolated molecules in significant density. The sample preparation method was therefore altered in an effort to produce samples with more consistent and denser coverage of isolated molecules using a common technique[25]. For this, a $\sim 100\,mMolar$ Mn_{12}-Ph in benzene solution was sprayed into vacuum ($\sim 10^{-7}$ torr) onto HOPG which had been cleaved in ambient conditions.

High resolution STM images of Mn_{12}-Ph molecules on the surface show distinct internal features which appear qualitatively similar across different locations and on different samples. In Figure 4.12 the XY resolution is 0.195 nm per pixel and the total Z between white and black covers a range of $1.99\,nm$.

Some further examples of single molecules in isolation on HOPG after vacuum deposition are shown in Figures 4.13,4.14, and 4.15. Figure 4.13 shows a 5 nm x 5 nm image of Mn_{12}-Ph on HOPG taken at liquid nitrogen temperatures. The scan image has an obvious line-defect (the horizontal line approximately halfway 'up' the figure) as the tip tries to step over what is locally a very tall feature compared to the background surface features. This could have been caused several ways, but the simplest explanation is simply that our STM tip was too close to the molecule and did not step far enough away fast enough to avoid touching the molecule, and thus unsettling the tip (and the molecule) slightly. Figures 4.14 and 4.15 are from the same sample surface, but of a different molecule like-feature (because our STM tip

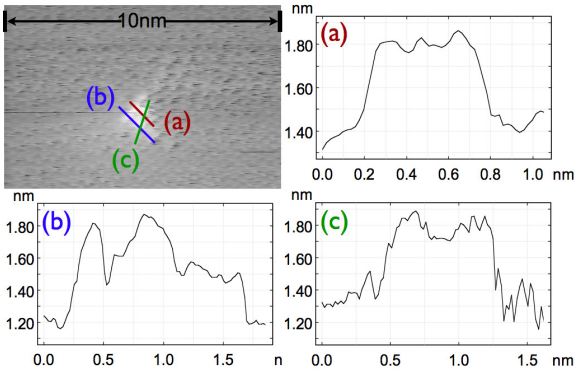

Figure 4.11: STM topographic image of molecular objects isolated on a HOPG surface at $\sim 4.9\,K and\ V_B = -500\,mV$. Inset: Height profile with respect to displacement along the vertical (red) line. The horizontal (black) line is a scanning artifact.

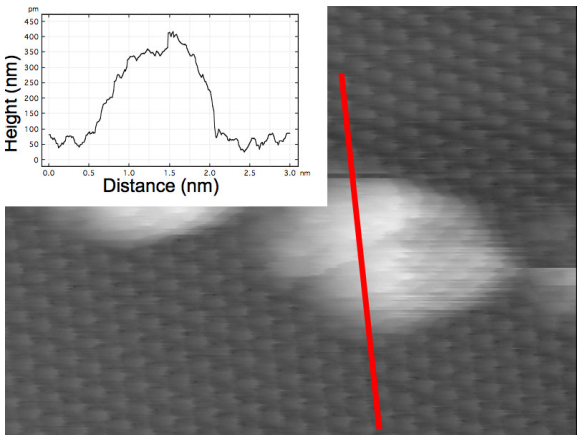

Figure 4.12: Topographic image, $10\,nm \times 10\,nm$ STM image at $\sim 80\,K$ of a molecule like feature with an overlaid line-cut (the red line corresponding to the height map in the upper left corner).

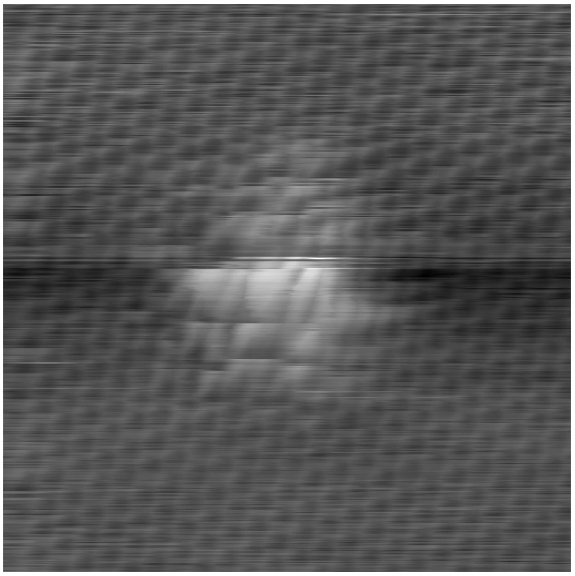

Figure 4.13: Topographic image, 5 nm × 5 nm taken at ∼80 K of a molecule like feature at -800 mV. This sample was a dip-and-dry sample of Mn_{12}-Ph on HOPG made with a very low surface density.

shed onto the surface near the previous image after the scan was taken). In these images, which are slightly larger (6 nm x 6 nm and 10 nm x 10 nm respectively) you can see the molecule has a strong bias voltage dependence for its apparent height (from the color change versus the background in the image). This indicates that the molecule has its own set of states and was not simply a wrinkle in the HOPG surface. The complexity of the dependence argues in favor of a more complex molecule. This by its self would not be conclusive, but control experiments were performed which did not find these features, and that make the result more convincing.

4.2.2 On Cu(111)

Once we switched away from HOPG to Cu(111) we needed to iteratively improve samples again. Here are a few examples from the end result of that process, Figures 4.16, 4.17, and 4.18. You can see that our overall sample now looks quite different

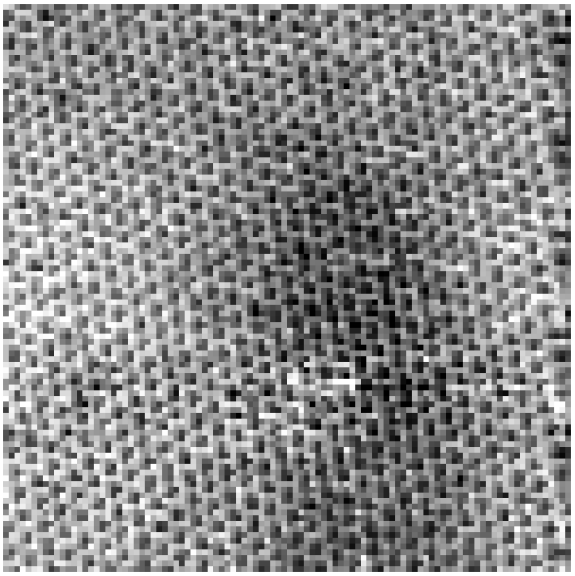

Figure 4.14: Topographic image is from a 6 nm × 6 nm STM image at ∼80 K of a molecule like feature at -800 mV. This sample was a dip-and-dry sample of Mn_{12}-Ph on HOPG made with a very low surface density.

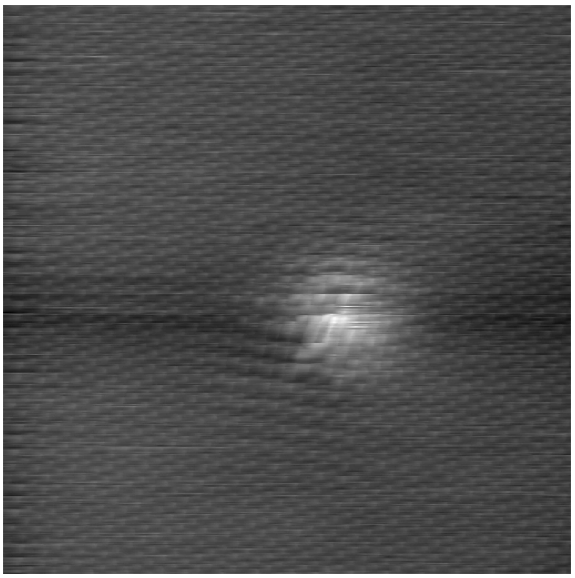

Figure 4.15: Topographic image, 10 nm × 10 nm taken at ∼80 K of a molecule like feature at +700 mV. This sample was a dip-and-dry sample of Mn_{12}-Ph on HOPG made with a very low surface density.

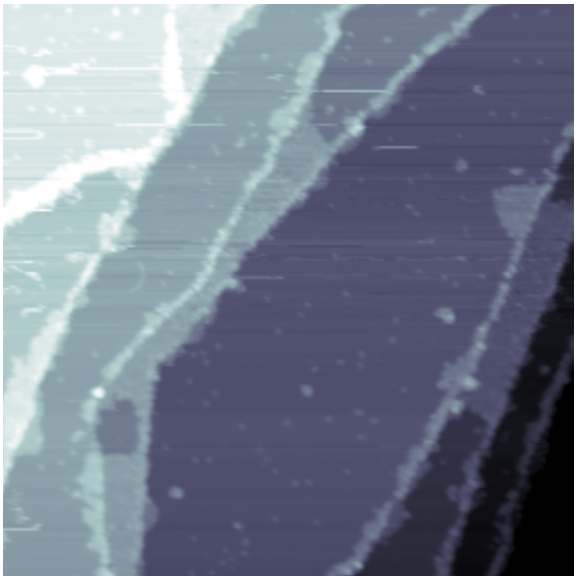

Figure 4.16: 168 nm x 168 nm STM height map of spray-deposited Mn_{12}-Ph on Cu(111), taken at -1.5 V and 30 pA tunneling current. We can clearly see several steps and a large terrace in the center of the image. The aggregation along the edges as well as the small bright dots on the terrace are Mn_{12}-Ph molecules. The height of the aggregate is the same as the isolated molecules, and so from this it appears the molecules simply tend to diffuse towards the step edges during deposition.

(Figure 4.16) due to several factors. First we are producing a much more uniform (and random) deposition after moving away from droplets which needed to evaporate, and our surface seems to much more strongly adsorb our molecules. If the surface was more inert we would have expected to see a random coverage and no film growth associated with the substrate. In figures 4.17 and 4.18 you can see isolated molecules along with the background surface. Unlike our images on HOPG, our molecules are now much more distinct (probably from being much more strongly adsorbed to the surface) and we can now see some of the background contamination from our UHV chamber (*e.g.* CO molecules).

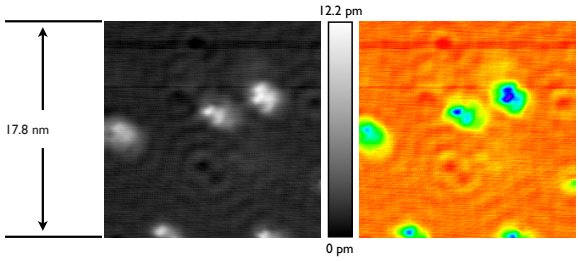

Figure 4.17: The same 17.8 nm x 17.8 nm images taken at -2.0 V and 30 pA tunneling current where several isolated Mn_{12}-Ph and several CO molecules are apparent. The right-most image has been color-table adjusted to provide a higher contrast for the features we find interesting. We have a good indication that the surface is very clean (other than our molecules) because the rings around the CO molecules which are Friedel oscillations resulting in the surface electrons scattering from the molecules on the surface of the copper are distinct, and from any given point source we can count multiple rings.

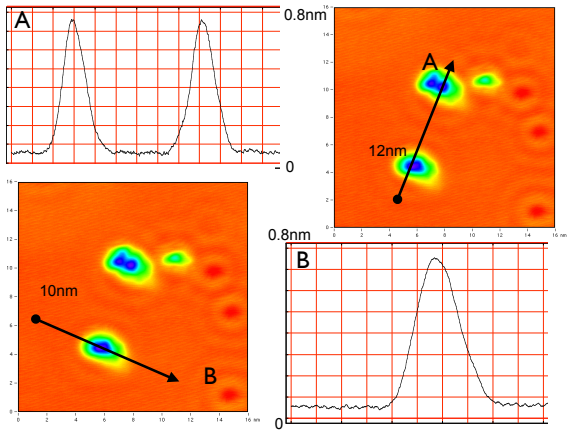

Figure 4.18: The same 16 nm x 16 nm images taken at -2.0 V and 30 pA tunneling current where several isolated Mn_{12}-Ph and several CO molecules are apparent. Line-cuts have been made across these molecules to show internal features as well as lateral-size. The measured sizes are within the expected parameters for our molecule.

5. LT-STM STUDIES OF MN_{12}-FAMILY MOLECULAR MAGNETS IN ISOLATION WITH HIGH SPATIAL RESOLUTION

This section will concern itself with the low temperature STM work that was done. The majority of this is done at liquid helium temperatures, then with a brief look below 1 K.

5.1 Surface features and their interpretation

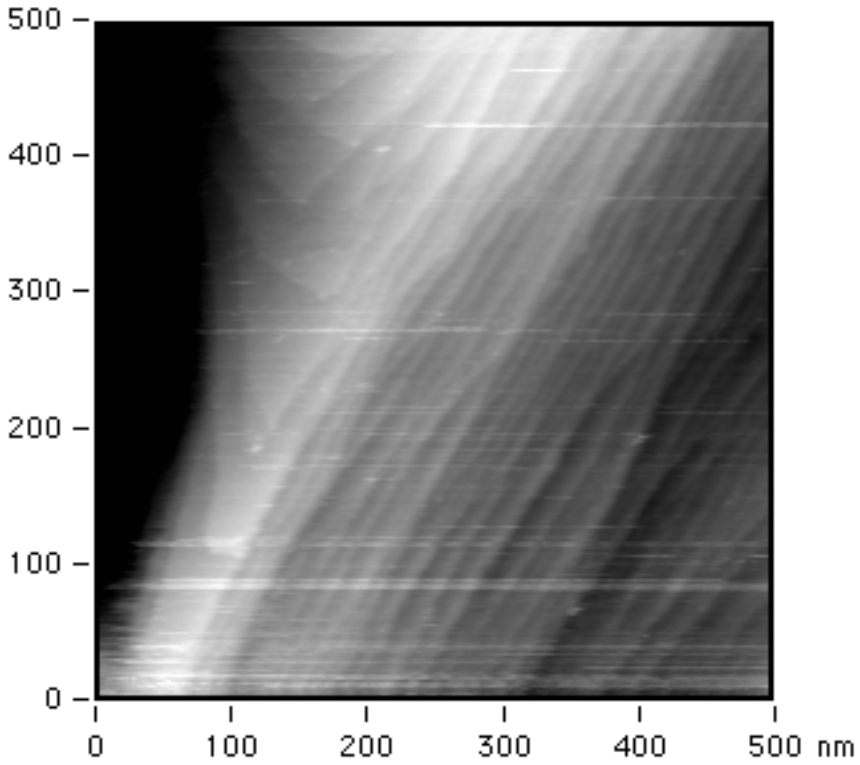

Figure 5.1: 500 nm x 500 nm area topographic view of Cu(111) with many terrace steps visible taken early in the surface-pre-processing stage of sample preparation to check the crystal preparation process parameters (see Appendix 1).

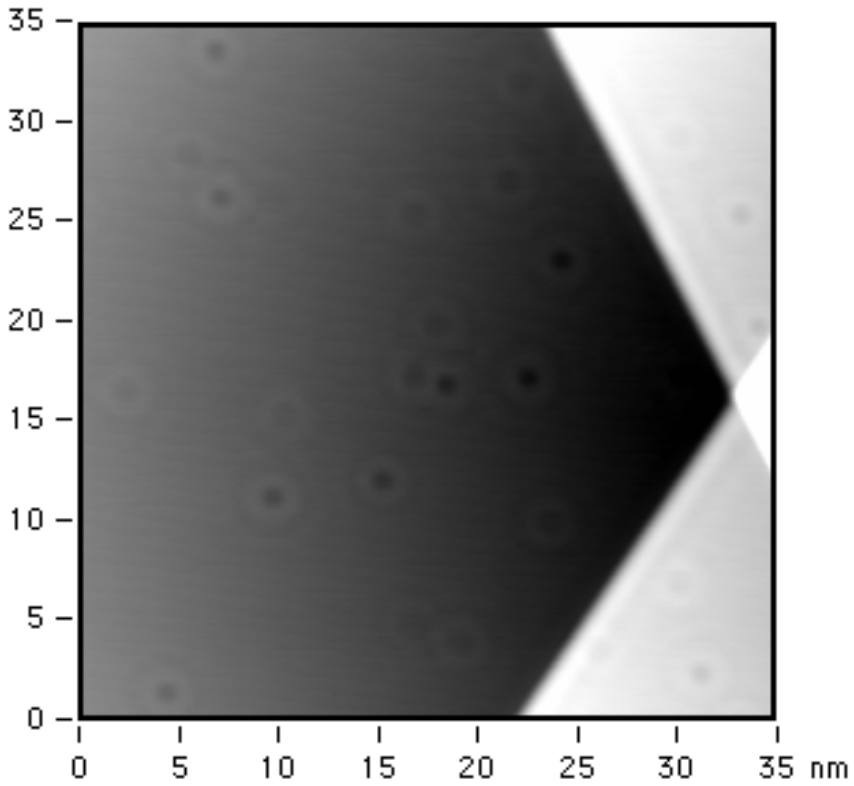

Figure 5.2: Topographic view of Cu(111) near a step edge with only CO contaminants visible. The CO molecules are the dark spots on the lighter background. They appear as spots because they stand vertically on the surface but offer a poor conducting path (and so the look like a hole). This sample had benzene injected into the sample preparation chamber as though a sample was being deposited, then the sample was left exposed to the turbo-molecular pump for approximately an hour before being moved into the STM chamber. No benzene is observed on the surface.

First we will look just at Cu(111) and then Cu(111) control samples (spray injection of only benzene), as shown in Figure 5.1 where we can see many terrace steps and then from a control experiment Figure 5.2 CO contaminants on the surface (the black circles) though no hints of our benzene solvent are apparent.

After reliably producing Cu(111) with a clean surface, and performing control experiments with our injection valve and benzene we can begin to produce very dilute films of Mn_{12}-Ph in benzene for deposition onto the Cu(111). Figure 5.3

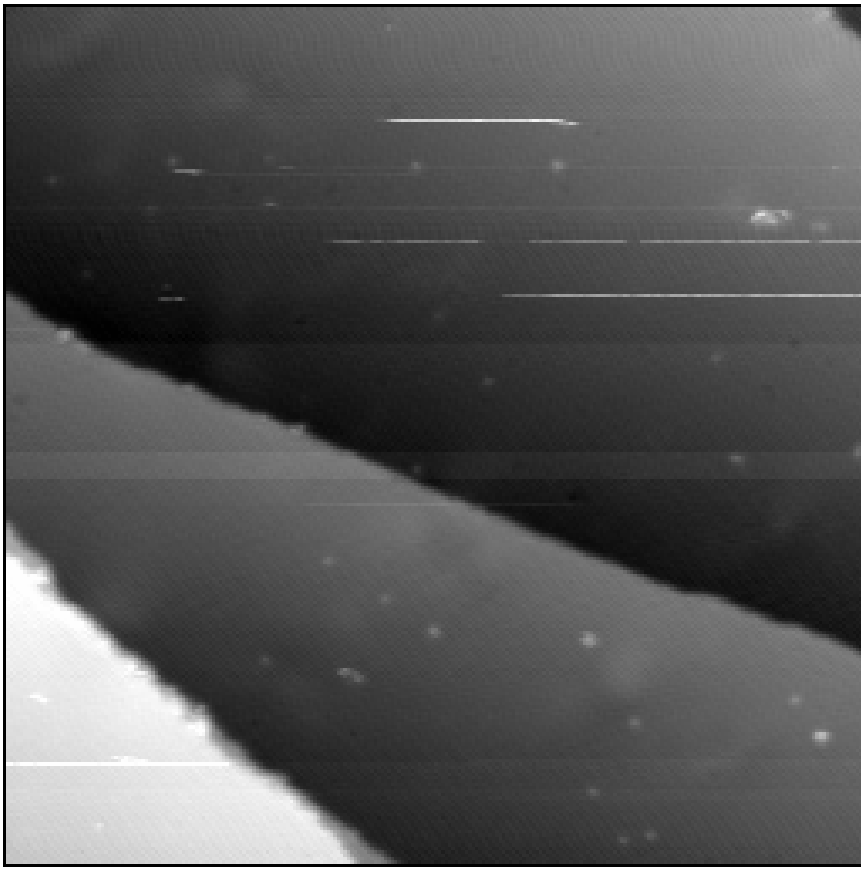

Figure 5.3: Topographic view of Cu(111) with a very sparse coverage of Mn_{12}-Ph. We can see some aggregation along the step edges of Cu(111) and occasional isolated molecules on the terraces. It was determined this density was too low for our purposes.

shows a very dilute film. We can see from this image very clear step edges, but the edges appear to have knobby features on them. These features on closer inspection are our molecules adsorbing along the step edge trying to form 2D films. We also see that if we intend to study isolated molecules that this film density is too low to guarantee many candidates as most of the molecules migrated to the step edge.

To increase our odds of finding isolated molecules we chose to maintain the density in solution but spray additional injections into the system (the equivalent of multi-

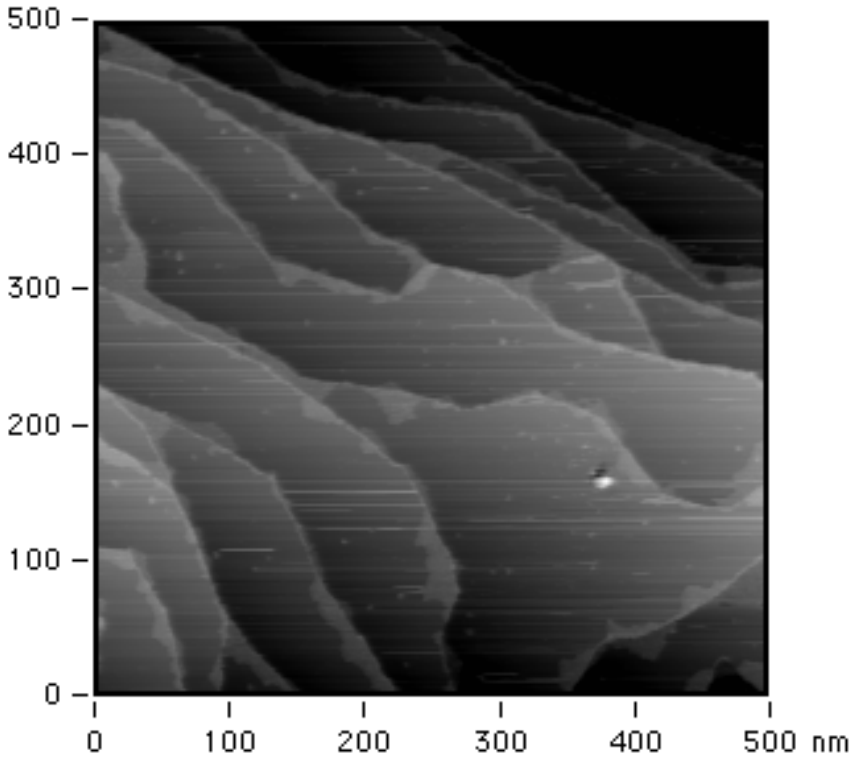

Figure 5.4: Topographic view of Cu(111) with a enough coverage of Mn_{12}-Ph to have completely filled the many available step-edges. The bright spot in the right side of the image on a terrace is a piece of the STM tip which shed onto the surface. We can see that the films grow out into the terraces when the edges are filled, this gives us some insights into the film growth mode and some estimates for the energy of adhesion of the molecule onto the surface.

ple drops in our drop-and-dry methodology) producing increasingly thicker films as shown in Figures 5.4, 5.5, which is ultimately tunable to full coverage (or beyond). These were all made with the same density of solution, only varying the number of injections to the chamber during deposition. In Figure 5.4 we see the continuation of our film growth along edges, and deeper into the terraces. We also see an increase in the isolated molecules and islands in the terraces. There is a large bright spot in the figure which is from the STM tip shedding onto the surface, but the overall image quality was high and the tip remained otherwise stable over this surface density of

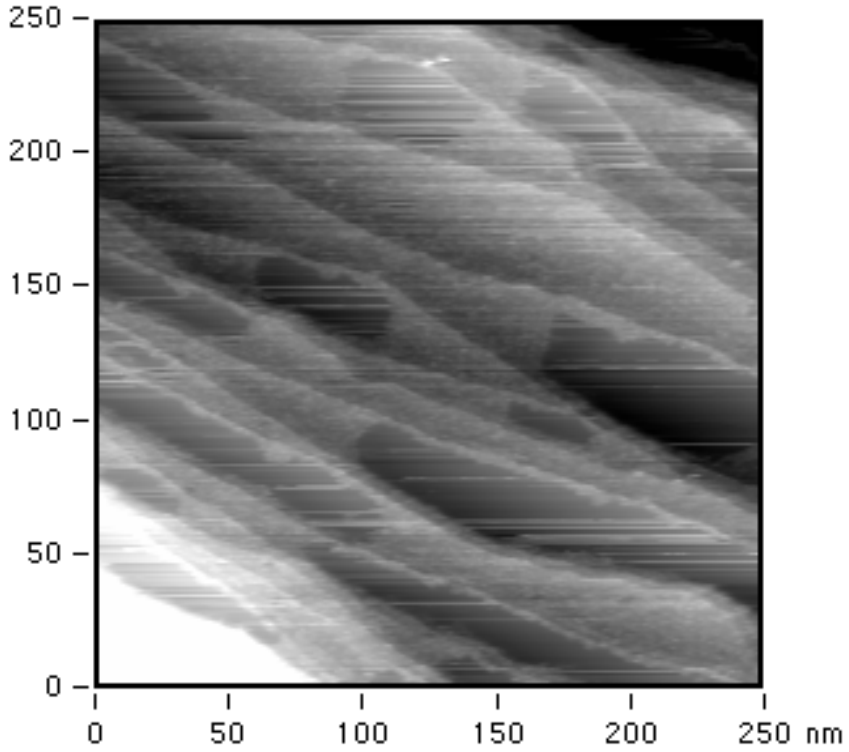

Figure 5.5: Topographic view of Cu(111) with a enough coverage of Mn_{12}-Ph to have completely filled the available edges and into the terraces; we can also see 2D island growth on the terraces. This density was judged to be too great, there are very few unoccupied areas of the Cu surface. You can see the many line-artifacts from scanning over this near monolayer film (the horizontal lines which look like smearing) caused by the instability of the tip over this surface.

molecules. Continuing to probe this parameter space, I increased the surface density again (see Figure 5.5) where the film coverage is now almost complete. There are only isolated patches of Cu terrace unoccupied. The quality of the image begins to degrade because the tip-interaction with the molecules is not as stable as over bare (or mostly bare) Cu.

The previous images have already bracketed the density I would ultimately choose to work at, but to further explore the flexibility of the deposition technique I will show a full film coverage (Figure 5.6) We can see cloudy features over a step-edge

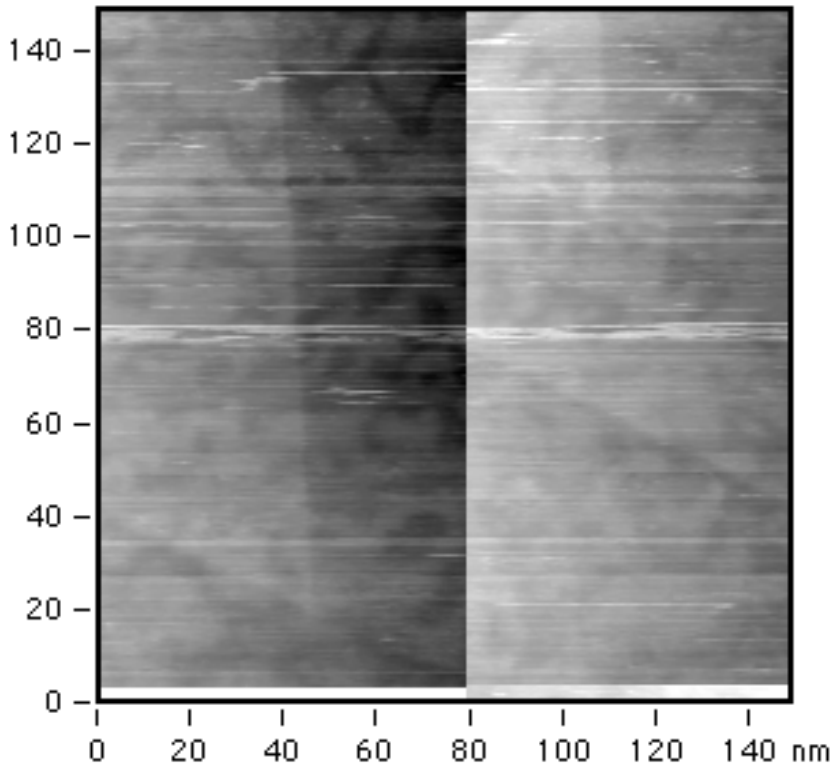

Figure 5.6: Topographic view of a full coverage film (perhaps several layers deep) of Mn_{12}-Ph on Cu(111). Because hints of the step edges are still visible it is assumed that this film is not very thick (the step edges are slightly shorter than the molecule height on the surface). The generally poor quality of this image results from the tip continuously picking up and putting down molecules and generally being unable to maintain the feedback cycle of tunneling current in a stable region over this surface.

and its two terraces (the edge is along the dark portion of the image and is somewhat 'v' shaped). The image quality is very poor, and it is extremely difficult to avoid crashing the tip into the surface at this surface density. If we did crash the tip there is nowhere to clean it because crashing it into the surface intentionally is one of the better tip-cleaning methods.

With this solenoid valve we have an easily tunable way of injecting a known volume of solution into vacuum and depositing on our surface to produce a predictable

surface density. Having experimentally bracketed the useful surface densities (trading open Cu which is good for setting up experiments with higher coverage allowing more candidate isolated features to study) we settled on one set of deposition parameters similar to Figure 5.4.

5.2 Adhesion and growth of films

Now that density in solution and density on our surface are under control we can address film growth more directly.

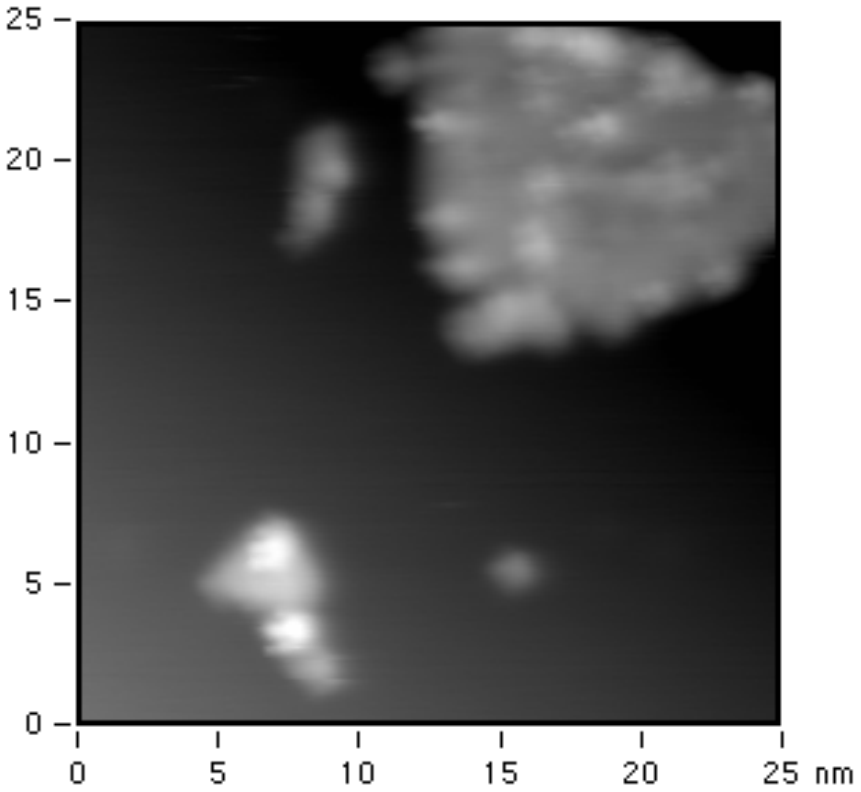

Figure 5.7: Topographic view of a 2D island growth of Mn_{12}-Ph in the middle of a Cu(111) terrace. We can see individual molecules forming the close-packed aggregate.

At low density we mostly see accumulation along step edges (see Figure 5.4 as a

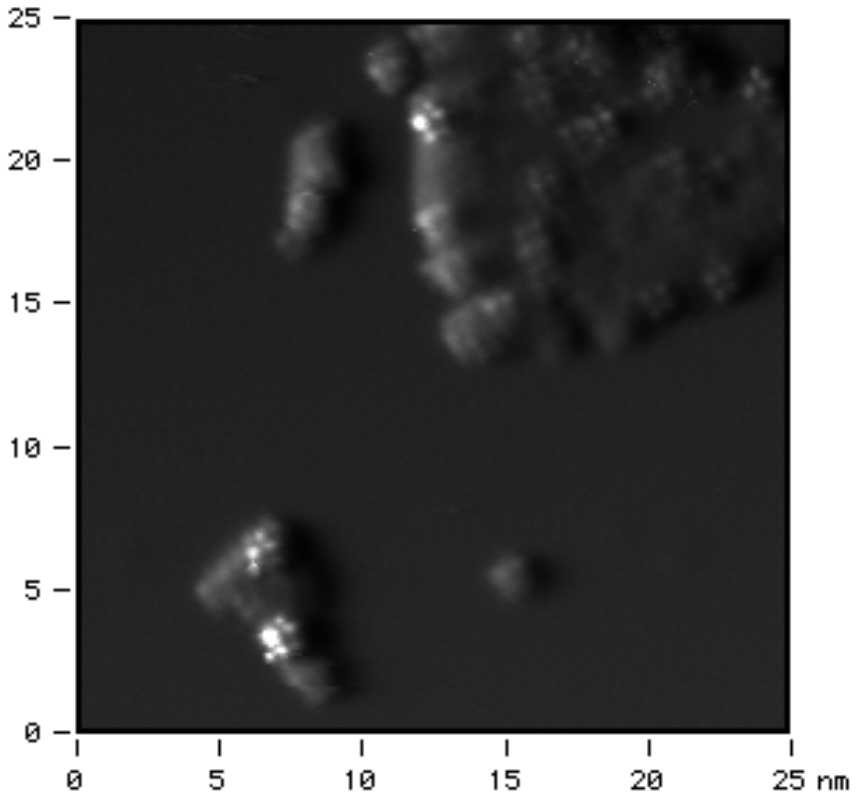

Figure 5.8: Current map image of the same 2D island growth of Mn_{12}-Ph in the middle of a Cu(111) terrace as in 5.7, note the sharply defined, very bright spots of inside the molecular perimeter (indicating a more strongly metallic behavior than the surroundings).

good example of this), and the step edges fill completely. So there is clearly some mobility on the surface during deposition for the molecules to condense into close packed films. At higher densities we start to observe 2D island growth, Figure 5.7, also in close packed films and isolated molecules. It is also interesting to look at the current map for Figure 5.7, Figure 5.8 and notice the molecules appear to be distinct, and have distinct metallic spots inside the molecular perimeter. The height of the individuals and the films is observed to be the same, and the internal features seen in the current map (Figure 5.8) appear to be qualitatively identical.

5.3 STS experiments

Having succeeded in obtaining images of isolated molecules and thin close-packed film areas, I proceeded to attempt to obtain spectroscopic data. STM images, as I have discussed before, can mislead one with apparent sizes because the size of an object is also related to how efficiently the tunneling process happens near it. To have convincing evidence of our molecule on the surface we would need to show Cu(111) spectra, and then something distinct from that which could be argued to be Mn_{12}-Ph from its spectroscopic behavior. To that end, roughly 2 months of data (approximately 35 STS) scans were completed, slightly more were attempted. For an STS scan to complete successfully the STM tip needs to not only be sharp and without noise in the voltage range you intend to scan at, but it must also remain stable for several days. This leads to a moderately high failure rate. Failures also tend to destroy the local surface (from tip shedding) and so a new desirable area needs to be found, the tip shaped, and then the process begun again. To compound this problem, the helium dewar has a maximum useful life (at helium temperatures) of less than seven days before it needs to be refilled (and this time is less if we intend to use the magnet). So, given those restrictions I tended to try STS scans that would complete in one to three days which limited my pixel resolution typically to something less than 128 x 128. This pixel density is independent of the image area, but I tried to keep the area and pixel numbers integer divisible and to maintain as much resolution as I could.

5.3.1 IV curves

STS data can best be expressed (at least in this format) as IV curves associated with pixel locations in an STM topographic image. Here are a representative family of IV curves for an STS scan of a single molecule (Figure 5.9) like Figure 5.10. Each

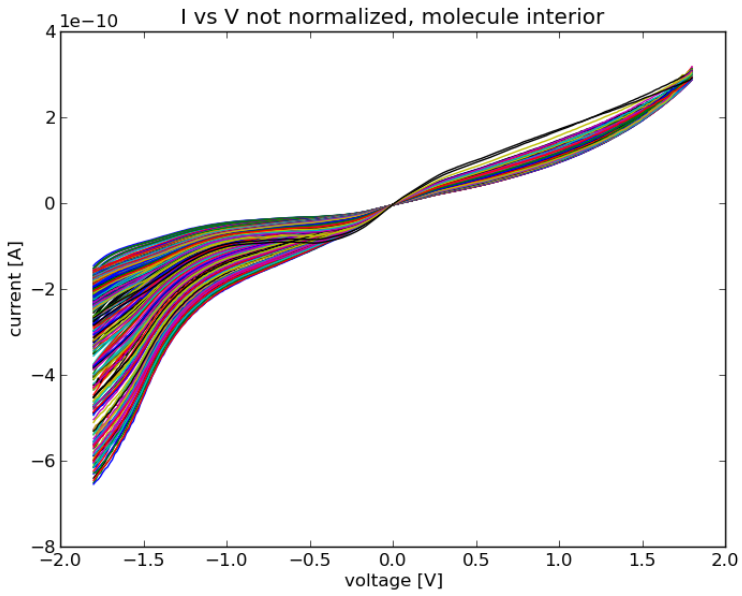

Figure 5.9: Family of IV curves ($\frac{1}{9}^{th}$ of the total number of forward-sweep curves, taken from the bottom left corner of Figure 5.11) each curve representing a single pixel of the STS scan they were extracted from.

pixels from Figure 5.10 looks like this as one slice of the IV curve (like our topographic image), Figure 5.11. This data can be hard to interpret because it incorporates both spatial and electronic information. I will create regions from applying a gradient to Figure 5.11 at some fixed voltage value to generate the regions in question (see Figure 5.12).

Outside the molecule is clearly Cu from our STM work, and so here is what my Cu IV curves look like from this spectroscopic study (Figure 5.13 and a reference Cu curve from a collaborator, Yoshinori Okada, Figure 5.14).

Inside the inner perimeter of the molecule we are tunneling into an organo-metallic object and our IV curves start to distinguish themselves from the Cu background, Figures 5.15, 5.16, 5.17. We see a decrease in overall tunneling current and the disappearance of the 'kink' feature. At first (Figure 5.16 we see that the total tunneling

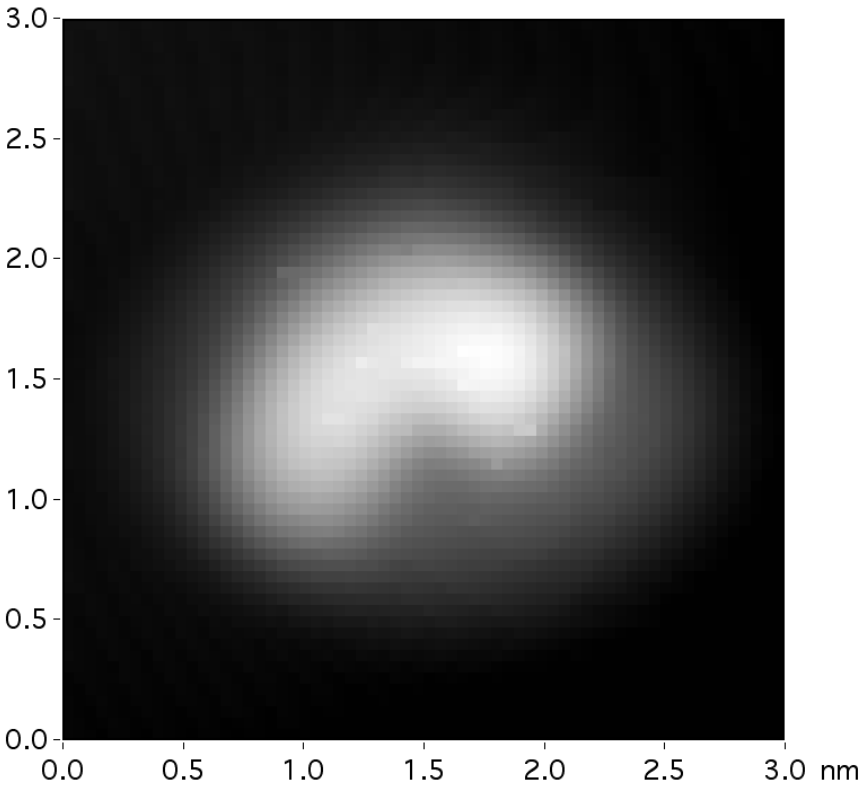

Figure 5.10: Topographic view of a typical isolated molecule and surrounding Cu surface, this is the molecule used for STS study.

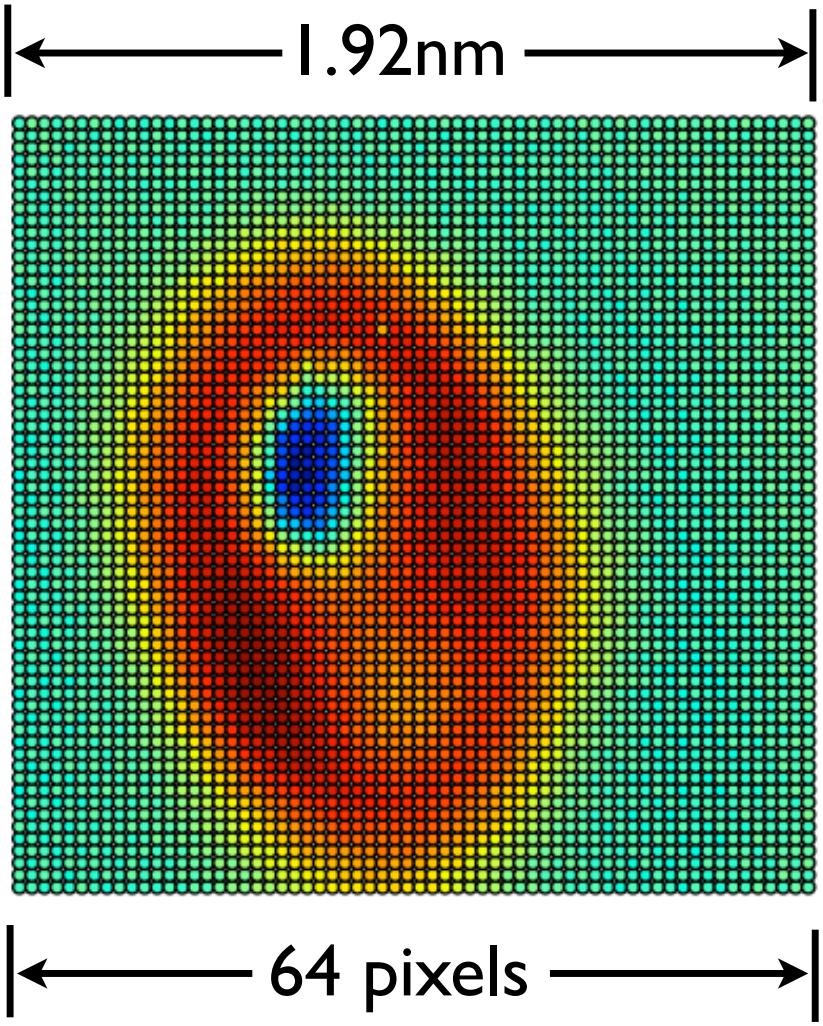

Figure 5.11: $I_{tunneling}(v_{bias})$ versus x,y; STM image analogue from an STS scan, this is every tunneling current pixel in the STS forward-sweep of bias voltages at a single voltage, -1.8 V in this case.

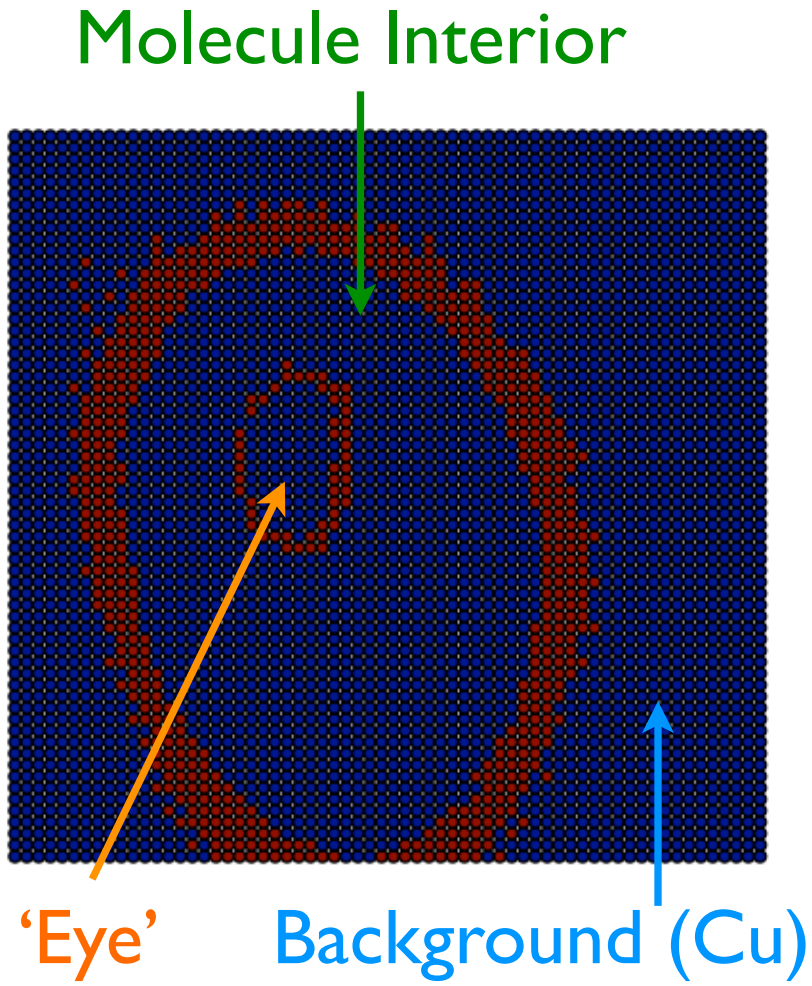

Figure 5.12: Boundary region cartoon: a gradient function applied to 5.11, this separates the molecule into regions by boundary regions. Similar colors are not intended to convey similar behaviors (in fact we will see that they are not similar) but similar content. The outer region is Cu(111), then there is a boundary inside of which is our Mn_{12}-Ph. Inside the Mn_{12}-Ph we see there is another distinct region which appears at some bias voltages.

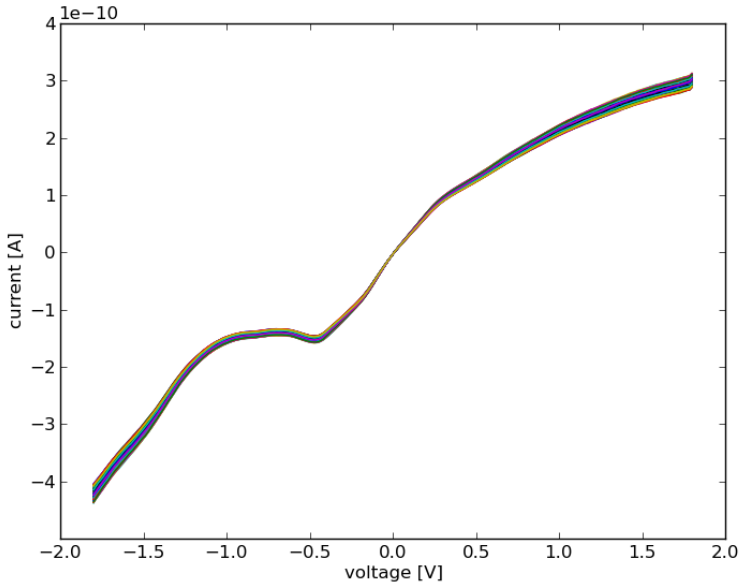

Figure 5.13: IV curve for Cu extracted from STS scan of Figure 5.11. We can see the distinct Cu 'kink' feature around $-0.5\,eV$ which will be our indication of copper like behavior when looking at IV curves.

current at high bias voltages is suppressed by approximately a factor of two from the pure Cu. The Cu 'kink' feature is also noticeably diminished (or perhaps entirely absent). Then as we move deeper into the molecular interior we start to see some areas which behave with some Cu like features (higher tunneling currents at high bias voltages, hints of the 'kink' feature). This interior region is most notable for the inconsistency of the IV behavior across what in our gradient image appeared to be a uniform region. The IV curves of Figure 5.17 are near the boundary with the molecular 'eye' (from Figure 5.12) and the tunneling current near high negative bias voltages begins to exceed that of pure Cu. This tail region of the IV curve is strongly non-linear and there are no hints of the Cu-like 'kink'.

The IV curve of Figure 5.18 is taken near the center of the molecular 'eye' and shows a return to the full Cu tunneling current in the $+eV$ side of the curve and

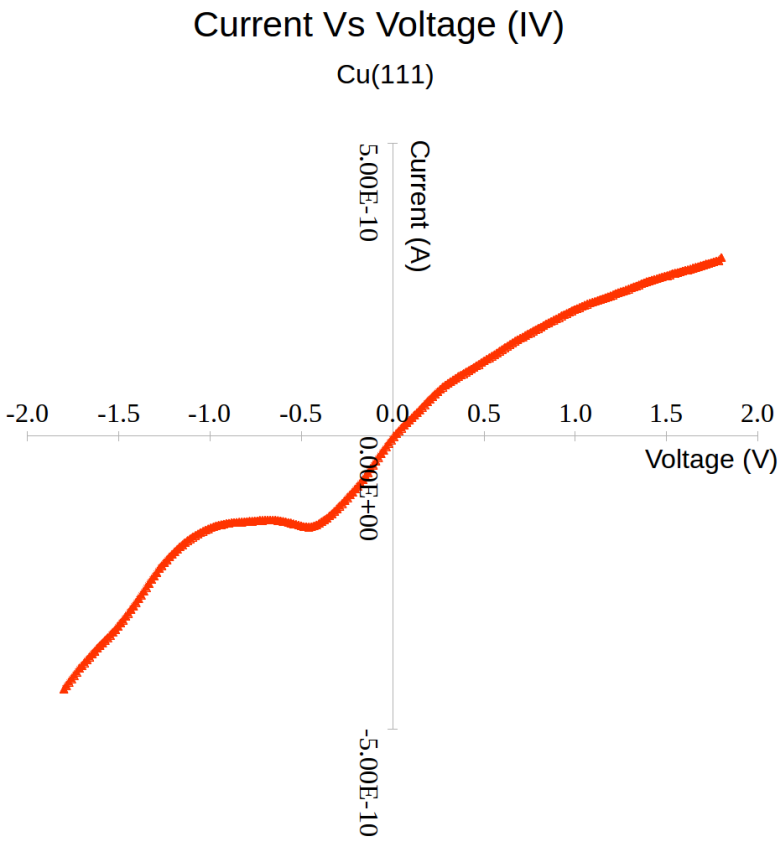

Figure 5.14: IV curve for Cu from my collaborator (OKADA Yoshi), the copper expert in the lab. We can see the same 'kink' feature.

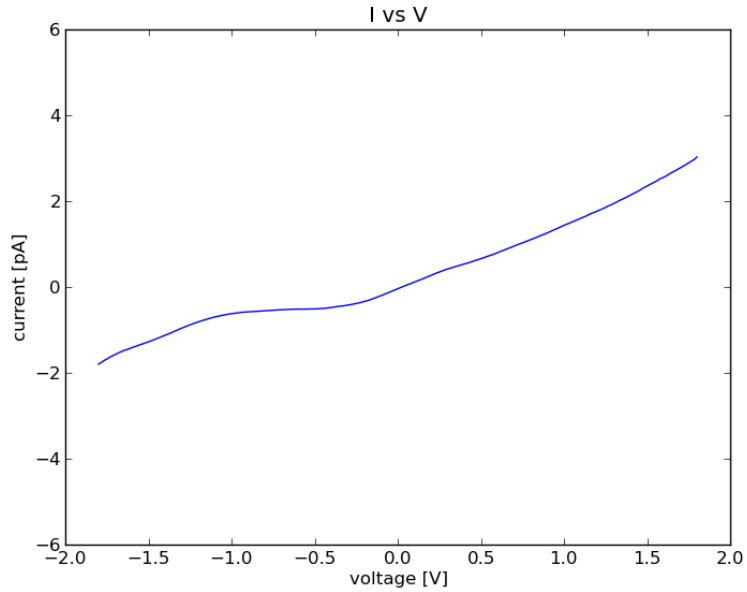

Figure 5.15: Interior IV curve, note the lack of Cu features, and the generally metallic (linear across v = 0) behavior. You can see that the total tunneling current is lower at either tail than in our Cu IV curves.

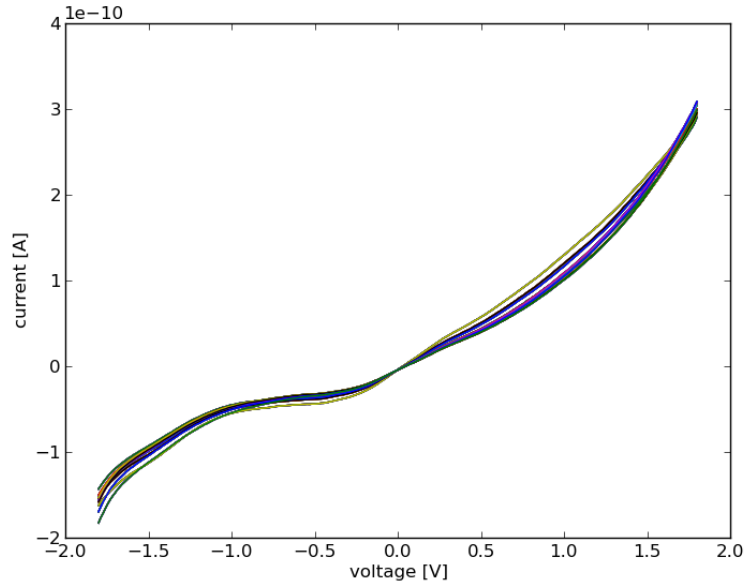

Figure 5.16: IV curves for some pixels in the interior region (a family of related curves from Figure 5.15.

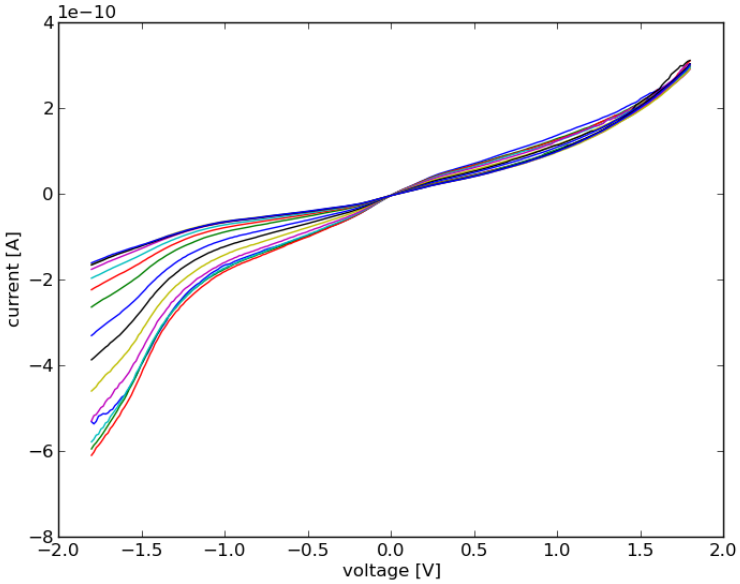

Figure 5.17: IV curves in the interior region as they approach the eye boundary (the curves that are lower on the left side are closer to the boundary). You can see the re-emergence of 'kink' like features but not located where the Cu kink should be, as well as a higher tunneling current (near the Cu(111) tunneling current) at high $-v_{bias}$.

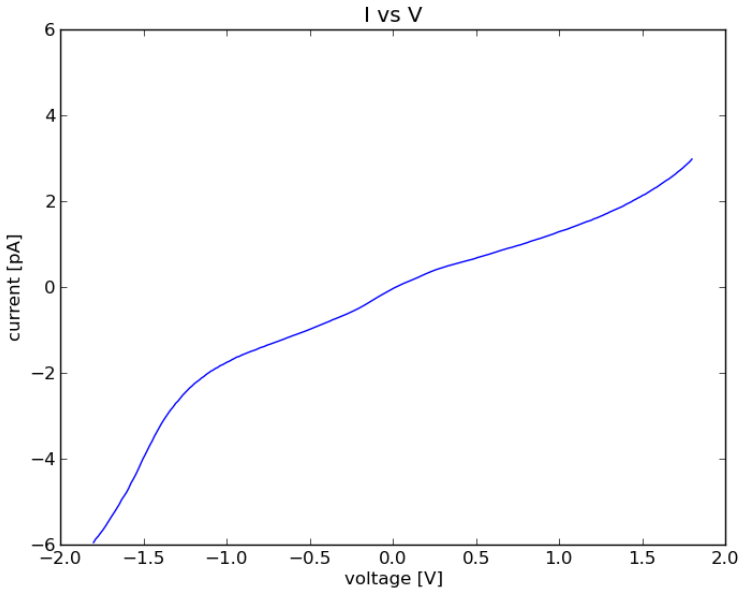

Figure 5.18: 'eye' region IV curve, note the lack of Cu features and the distinct asymmetry of the tails (across 0 eV). Overall tunneling current exceeds that of Cu(111) and a 'kink' like feature is present.

exceeds the tunneling current of Cu in the $-eV$ side of the curve. There are changes of slope in the curve near where the Cu kink should be, but no obvious signs of the feature itself.

The last figure of this section, Figure 5.19, is on the 'eye' side of the boundary with the upper 'molecular interior' region in Figure 5.12. The non-linear $-eV$ feature of the IV curve is still present but is less extreme, the overall maximum tunneling current is closer to symmetric across $0\,eV$ than in the interior of the eye.

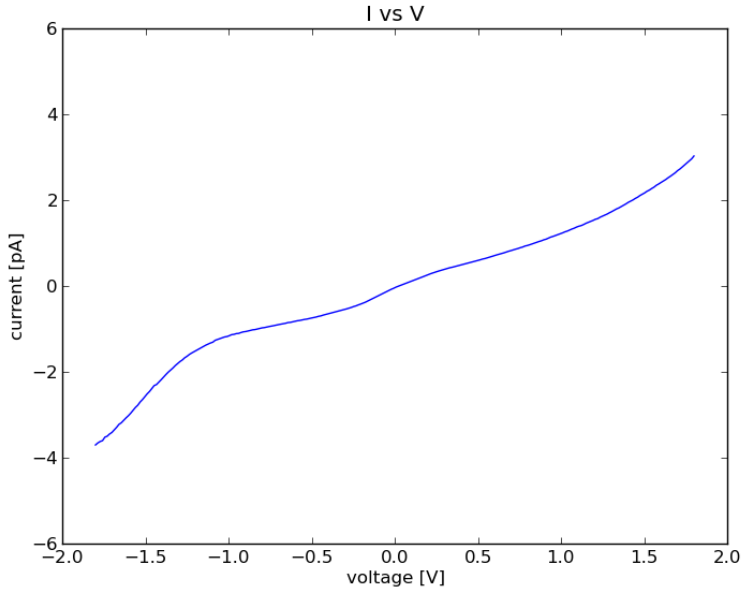

Figure 5.19: 'eye' region IV curve near the boundary with the interior region, note the lack of Cu features and the return towards symmetry in the maximum tunneling current at high bias voltages (near the Cu(111) values again).

6. PHENOMENOLOGICAL EXPLANATIONS OF SPECTROSCOPIC BEHAVIOR

6.1 IV curves and junction impedance

From the IV curves we generated in our STS scans, we can calculate DC resistance from Ohm's law: $R = \frac{V}{I}$. We can then plot this as R vs V to try and characterize where impedance changes with respect to voltage in our images. This should allow us to discuss how metallically a given pixel is behaving, or if we have a mode diode-like behavior, or something else entirely.

An RV curves for the Cu(111) background is shown in Figure 6.1.

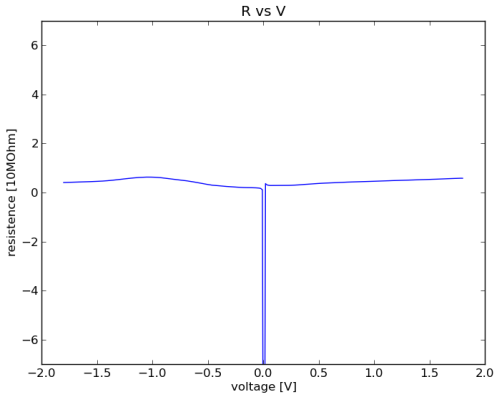

Figure 6.1: R vs V over the copper background from 5.12.

Then we progress to RV curves for a location inside the molecular interior region, shown in Figure 6.2.

Finally we can look at RV curves for the 'eye' region, shown in Figure 6.3.

Figure 6.1,6.2, and 6.3 share a discontinuity at zero, as we would expect, but are

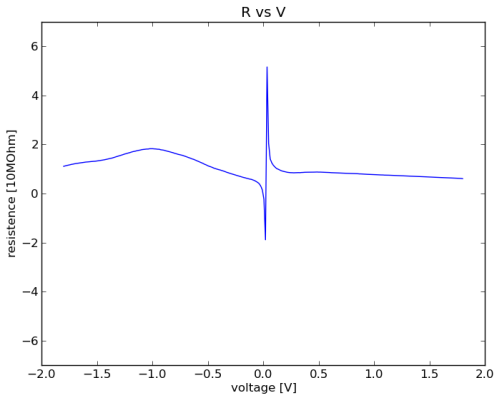

Figure 6.2: R vs V over an area in the molecular interior (from Figure 5.12).

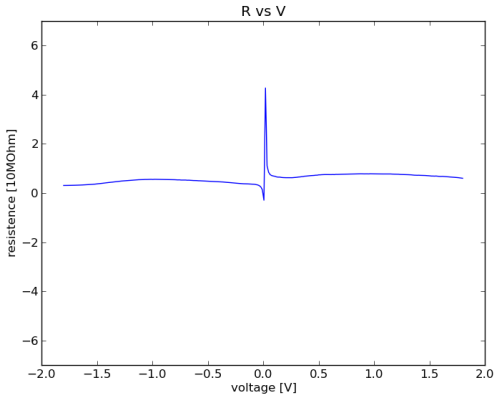

Figure 6.3: R vs V over the 'eye' region of the molecule (from Figure 5.12).

otherwise quite distinct. The copper is very flat, and symmetric across $0V$, as you would expect from a metal, the resistance does not depend greatly on the voltage applied. The molecular interior has distinct features on the $-V$ side of the graph, this should correspond to the lowest unoccupied molecular orbitals (LUMO) filling and then the voltage having to overcome this set of filled states to find a state to tunnel into. The 'eye' has a metallic like behavior but an asymmetry across $0V$.

6.2 Tunneling phenomena

I have already discussed the mathematical model behind STM junctions (Equation 3.1 expresses the full integral form, but we can simplify the expression to something like $\frac{dI}{dv} \approx C \cdot \rho_S$ where the constant C absorbs the constant density of states of the tip and the energy smearing from being at a finite temperature and having Fermi distributions), but we should also recognize that that the integral I expressed is the one which obeys the principle of least action and allows for multiple equivalent paths to be indistinguishable solutions. To make matters worse, we are not tunneling a single electron from an atomically sharp object into a perfect plane, and so there are likely many equivalent, or near equivalent paths for the electrons to 'choose' from. Each of these creates a local field and interferes with the others. This causes a blurriness in the observed energy level for a given a pixel of IV data and its corresponding location in space in our tunnel junction. In fact our instrument is so precise in its movement (pixels in our STS scans that are sub-angstrom in size) that we can be fooled into thinking that our interaction volume is as small as our pixel small, but it almost certainly is not. To that end, I propose a few tunneling phenomena which might explain what we are seeing with the IV curves we have produced.

First of all, we should look at what the ideal tunneling situation would be. If we were tunneling from a tungsten tip into a tungsten surface for instance, we should get a perfectly straight line in IV with a constant slope that passes through zero. However, we are tunneling from Pt-Ir into a molecule and Cu (or perhaps just Cu in some cases) (see Figure 6.4).

We know we do not have ideal tunneling behavior (for many of the reasons discussed previously), so let us think about a more realistic picture of our junction. We have a molecule in intermittent contact with the surface, only partial overlap of wave

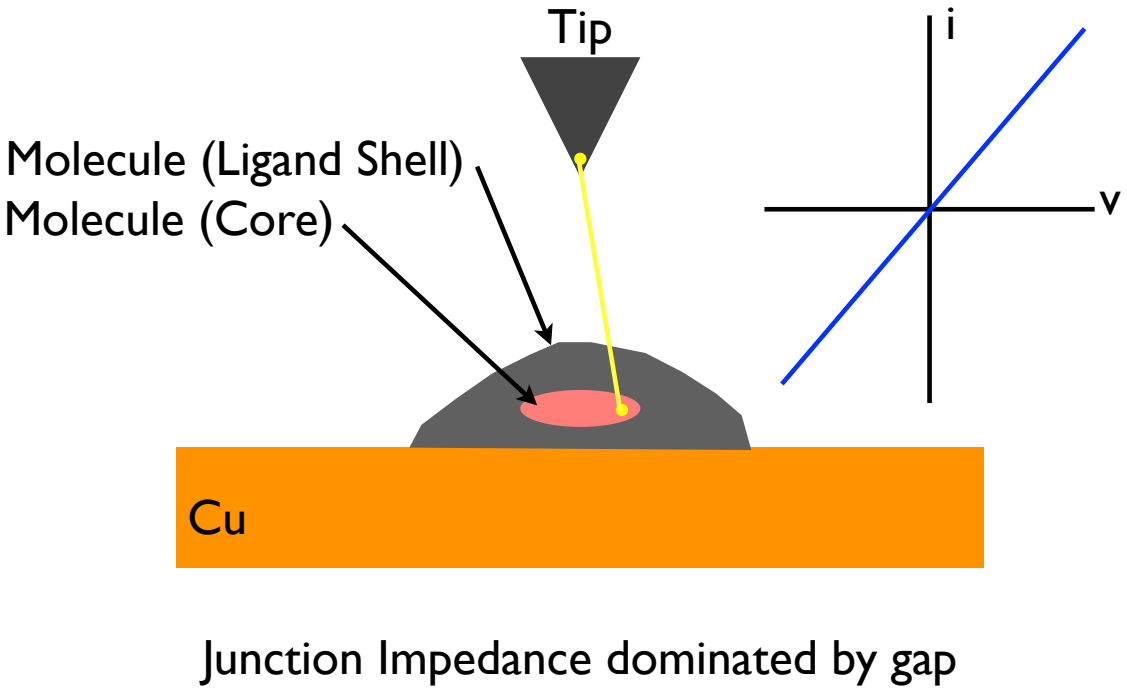

Figure 6.4: Cartoon depiction of an ideal tunnel junction for this system. The molecule is in perfect electronic contact with the surface (a large overlap of their wave functions), and we would tunnel into well localized areas of the molecule from a single point on the tip.

functions, almost certainly through the ligand π electrons. In addition to that, we have multiple self-interfering paths for tunneling, made worse by the near four-fold symmetry of the molecule and the very small size of the junction. Compounding that we have a mismatch of work-functions between the metal tip and the molecule under it, making it harder to overlap wave functions (the highest occupied molecular orbitals and lowest occupied molecular orbitals in the junction have a substantial gap between them) suppressing tunneling current, effectively increasing the junction resistance. Figure 6.5.

Last we have to consider that we are not observing single tunneling events, or at least not only single tunneling events. These events must be more rare, because

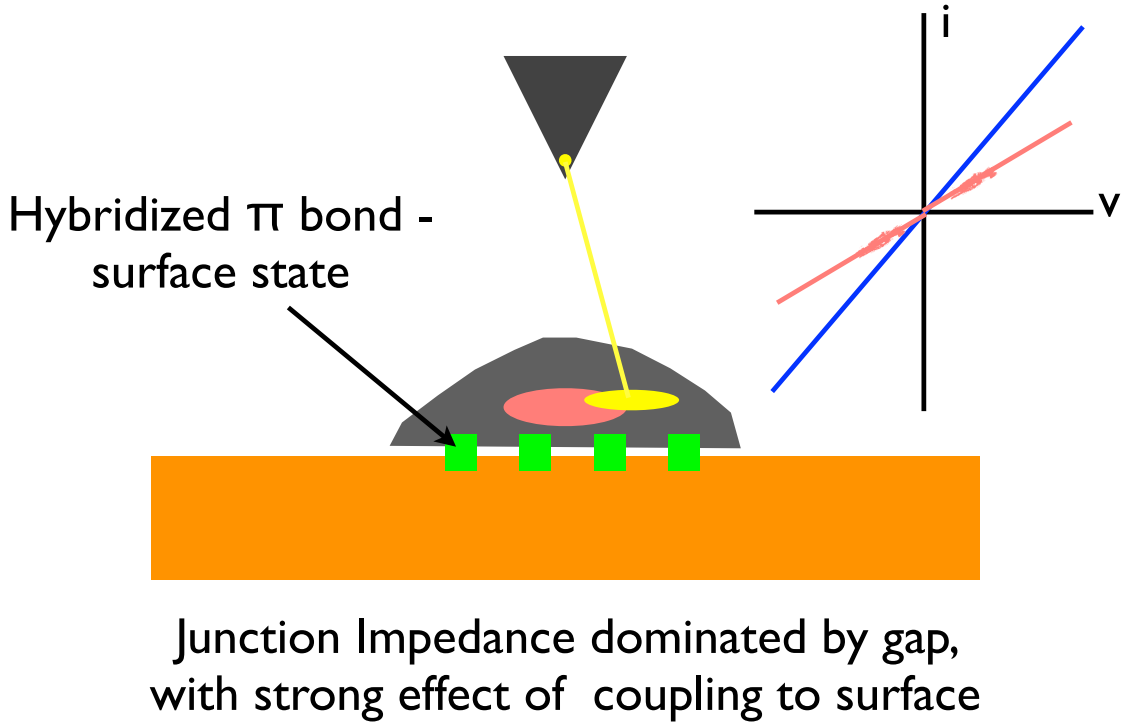

Figure 6.5: Cartoon of a more realistic tunnel junction for this system. We see intermittent contact between the molecule and the surface, and a more diffuse tunneling zone.

tunneling probability is distance dependent, and conductance is possible, though restricted, in our molecule which must usually be energetically favorable. Double tunneling, like in Figure 6.6 also effectively increases our junction impedance.

Below 1 K we managed to make some observations, but achieved no meaningful spectroscopic results. Here are a few of our observations, Figures 6.7, 6.8

To work at sub-kelvin temperatures required a change to the instrument with a dilution refrigerator. This also meant changing around the orientation of some of the support structure for the spray injections, etc. Amongst the changes was working with a different annealing filament, which had less precise temperature control. The Cu crystal had 'step bunching' and so it was more difficult to grow films along step

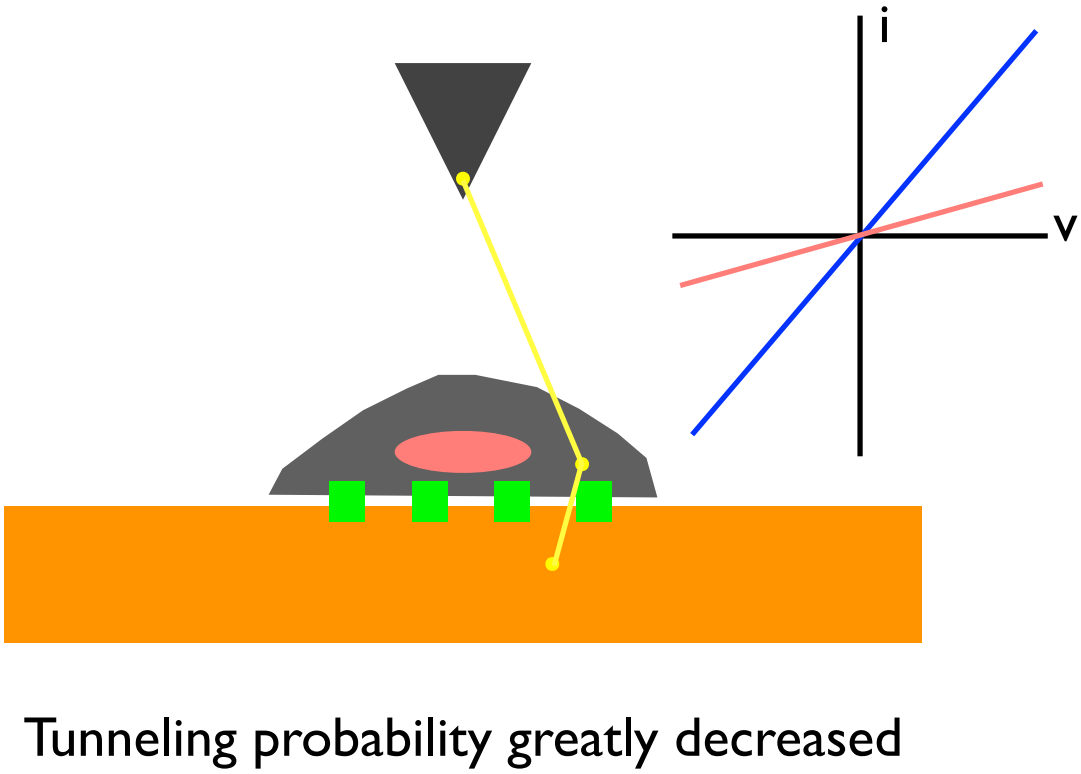

Figure 6.6: Cartoon of a double tunneling path, skipping our conductance path out of the molecule and into the Cu entirely.

edges, so our depositions seemed less ordered.

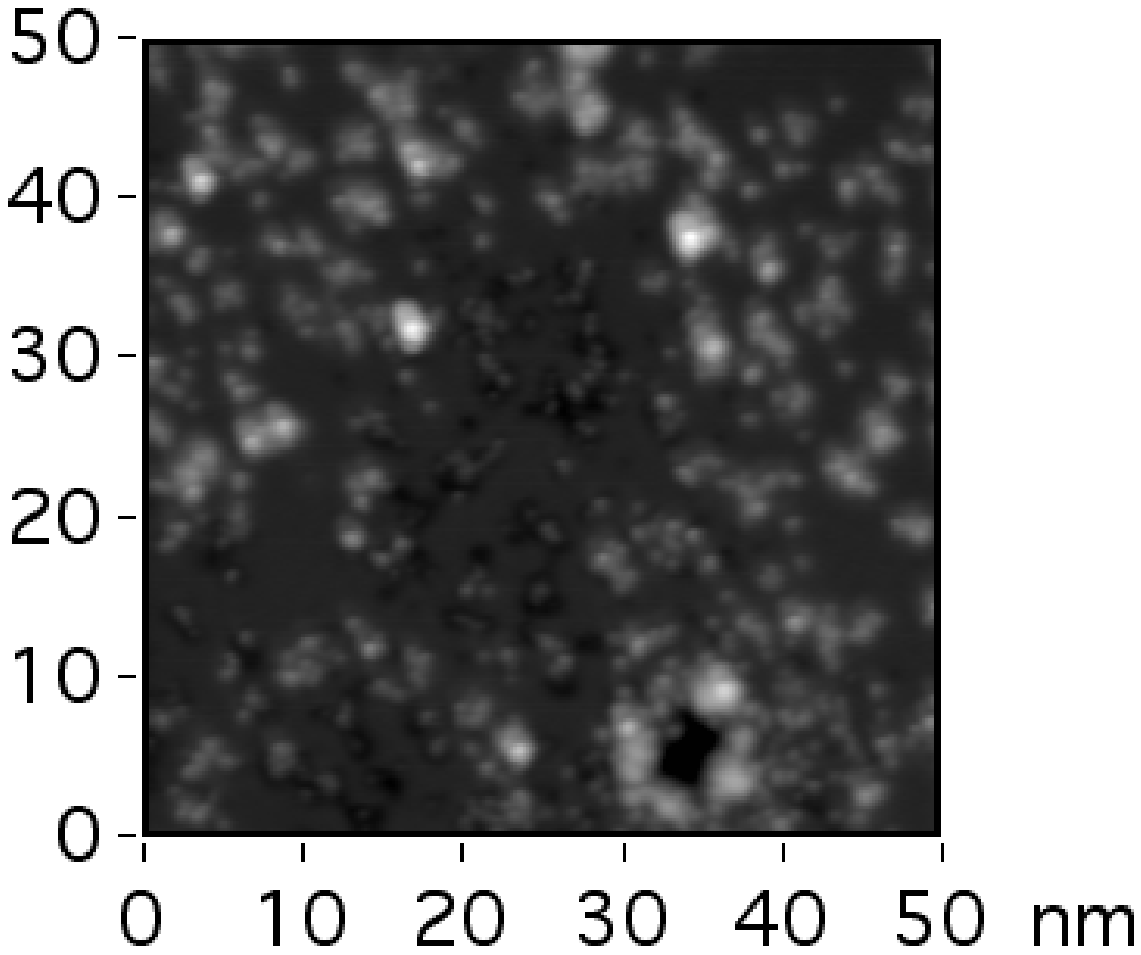

Figure 6.7: Topographic image of film aggregate on a Cu(111) terrace, imaged at 300 mK with a tunneling current of 30 pA at -0.5 eV sample bias.

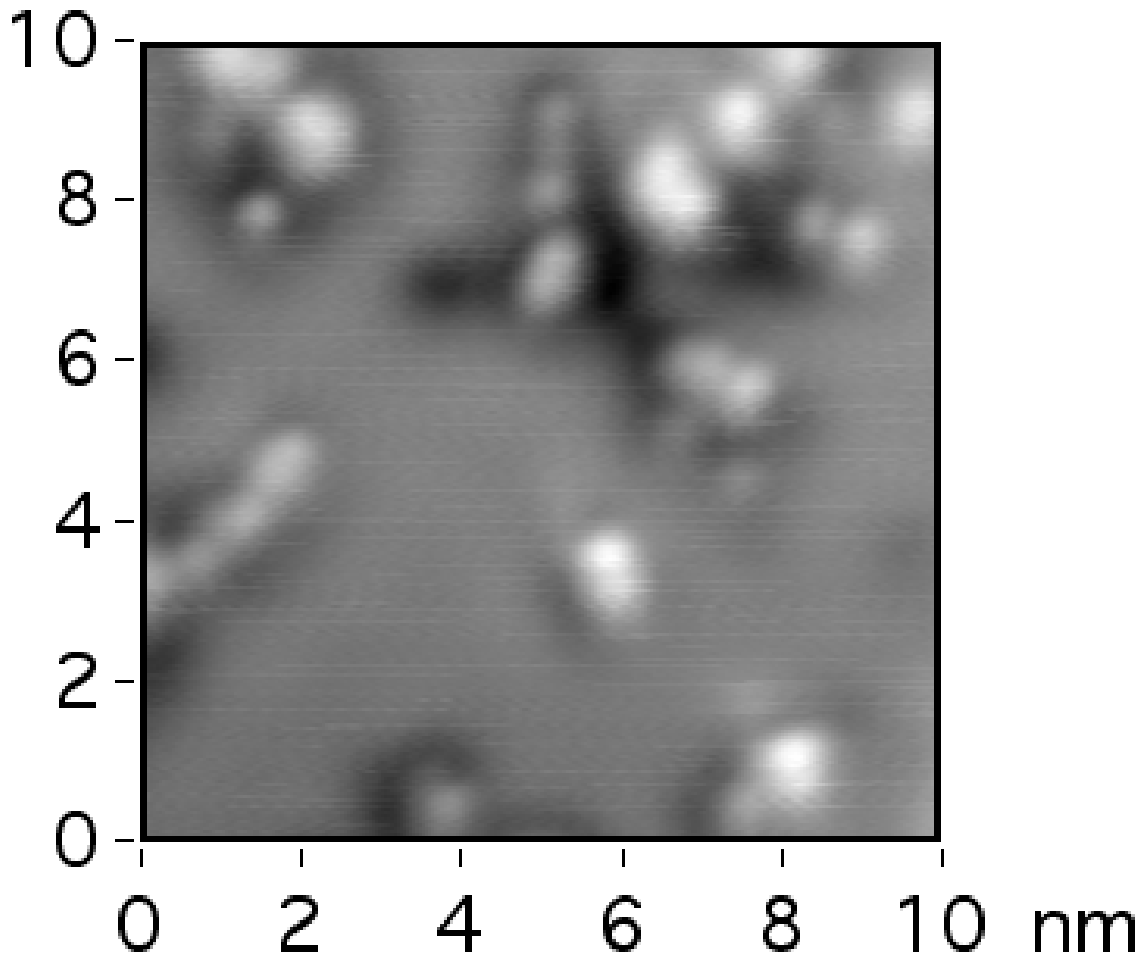

Figure 6.8: Topographic image of isolated molecules on Cu(111) on a terrace, imaged at 300 mK, with a tunneling current of 30 pA at -0.5 eV sample bias.

7. THEORETICAL WORK AND MODELING

Because modeling our system is hard, due to the many interacting electrons and the magnetic field, I developed in collaboration with Daniel Packwood and others[30] a method of treating a spin state as coupled set of node and edge matrices, or graphs.

So rather than solve this problem:

$$\hat{H} = -\sum_{i,j} J_{ij} \hat{\mathbf{s}}_i \cdot \hat{\mathbf{s}}_j, \tag{7.1}$$

We attempt to solve this optimization problem instead:

$$R = \frac{c}{n_e J} \sum_{(i,j)\in E} \Delta r_{ij}, \tag{7.2}$$

Where R is a fitness function indicating stability of a spin state in an arbitrary edge-matrix of interactions J between nodes i and j. Now we can begin to test the probability that our spin is robust under random deformation by forming a statement about the probability P of deformation of R beyond ϵ (some small deformation):

$$P\left(|R| < \epsilon\right) > 1 - \epsilon \tag{7.3}$$

And we arrive at the following result:

$$var(R) = \sigma_x^2 (\frac{c}{j})^2 Q \tag{7.4}$$

Where,

$$Q = \frac{1}{n_e} + \frac{1}{n_e^2} \sum_{\phi\in A} \cos\phi. \tag{7.5}$$

Equation 7.5 therefore shows that the total spin of a molecular magnet, con-

structed according to our parameters will be stable to shape deformations if the factors $|c/J|$ and Q are small. $|c/J|$ measures the degree to which the spin-spin interaction strength within the MM changes under an arbitrary deformation.

Discussing $|c/J|$ turns out to be its own hard problem, because J is dependent upon bond length, angle, and so on which in a real molecule are subject to change. We will treat it as a small constant here for the purposes of our model.

Considering this model for a toy system, Platonic solids (the tetrahedron, octahedron, cube, dodecahedron and icosahedron), as an example calculation we can compute $P(|R| < \epsilon)$ using the formula below:

$$P(|R| < \epsilon) = P(R < \epsilon) - P(R < -\epsilon). \tag{7.6}$$

To quote from our paper on this subject[**?**]: "Using $\epsilon = 0.05$, $\sigma_x = 0.15$ (i.e., deformations that shift the spin centers a distance of 15 % of the edge lengths on average) and the formula for var(P) and Q above, we find that $P(|R| < \epsilon) = 0.16$ for the tetrahedron ($n_e = 6$), $P(|R| < \epsilon) = 0.31$ for the cube (n_e =12), $P(|R| < \epsilon) = 0.23$ for the octahedron ($n_e = 12$), $P(|R| < \epsilon) = 0.70$ for the dodecahedron ($n_e = 30$), and $P(|R| < \epsilon) = 0.48$ for the icosahedron ($n_e = 30$). We would therefore expect that the total spin of a ferromagnetic MM with a tetrahedral arrangement of spins to be much more sensitive to shape deformations to the molecule than the total spin of a MM with a dodecahedral arrangement of spins. However, in none of these cases is $P(|R| < 0.05) > 0.95$, and therefore none of these molecules has a weak topological invariant total spin."

So we can move on to a slightly more realistic model, of an object consisting of arbitrarily connected polygons of spin centers, defined in the following way:(n_v, n_e, N), where n_v is the number of vertices in an object, n_e is the number of edges in our

object, and N is the number of polygons in an object.

We can write the maximal structure for this class of objects in this way:

$$T^*_{(n_v,N)} = \begin{cases} P_{n_v-2(N-1)}|(N-1)P_4 & \text{if } (N-1) - A_{(n_v,N)} \leq 0 \\ (A_{(n_v,N)} - 1)P_4|P_{n_v-2(N-1)}|P_4^{N-A_{(n_v,N)}} & \text{if } (N-1) - A_{(n_v,N)} > 0, \end{cases} \tag{7.7}$$

Now if we manage to find our P(R) for this class we will have an upper bound for all such objects.

$$P(|R_{(n_v,N)}| < \epsilon) \geq P(Z_{(n_v,N)} < \epsilon) - P(Z_{(n_v,N)} < -\epsilon), \tag{7.8}$$

Where $Z_{(n_v,N)}$ is a Gaussian random perturbation with centered on 0 and with a variance of $\text{var}(R) = 2\sigma_x^2(c/J)^2 Q^*_{(n_v,N)}$.

If we were to then prove our bounds rigorously (see the appendix A of the published work[**?**]) you would see that at around 20 spin centers a weak topological invariance to perturbation arises that is robust to perturbations on the order of about 15% shift in location of any nodes in the network.

8. ANALYSIS AND CONCLUSIONS: TYING THE THREADS TOGETHER

We compare our STM results to those in the literature for related molecules in the Mn_{12} family and have quantitatively (size, general profile, and bias dependence) similar results[15] in our topographic images, although we are comparing related (not identical) molecules. I can achieve tunable densities of isolated molecules on the surface, and have achieved greater isolation than has been reported using electro-spray deposition or solution spray deposition[21, 25]. The care taken with the surface and solvated molecule solution introduced to the surface implies that the observed objects are either related to the solvent or the solvate (or some combination of both). The size of the objects coupled with the local density of states (LDOS) behavior of the interior of the molecules indicates that the molecule-like objects are metal-centered large molecules with an organic shell. Control experiments were performed using clean (freshly cleaved) HOPG and freshly prepared Cu substrates with no solvent or molecules deposited, and also HOPG and Cu substrates with only solvent (benzene) added. No comparably-sized molecule-like objects were observed in the control experiments, though on Cu we can always image CO molecules. The bias evolution dependent behavior indicated that the molecules are physisorbed to the surface, as expected. Coupled with the control experiments this indicates that the objects are not surface defects or contaminants. Further the background contamination in our STM was mostly ionized argon from our sputtering system which had been cryo-pumped into the dewar, Figure 8.1.

Characteristics of Mn_{12}-Ph on HOPG and Cu(111) show distinctly different IV behavior when compared to the graphite and copper backgrounds. As can be seen in the previous sections. These findings are consistent with the observed behaviors

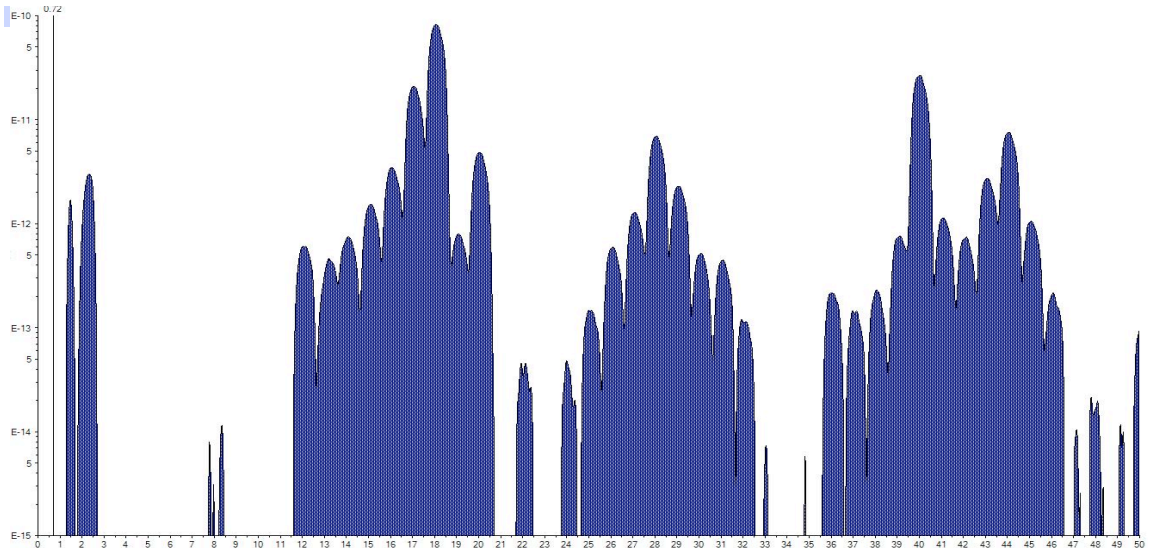

Figure 8.1: This is a residual gas analyses measurement taken, in collaboration with Patrick Han of the chamber contaminants. In the Y axis is frequency, and in the x axis is atomic mass/z, note that the mass determination has a charge dependence due to the method of measurement.

of similar organo-metallic cluster molecules[16].

Mn_{12}-Ph is not the most commonly studied from the Mn_{12} family of molecules, but the relative ease of changing functional (or inert) organic ligand groups is an added incentive for studying the family of molecules for later adaptation to applications like q-bits or spin-sensitive transistors. I have shown Mn_{12}-Ph in isolation, in small clusters, and complete films as well as the ability to tune between those surfaces as desired.

In addition to the purely topological observations of the molecule, we have presented spectroscopic data which show a strong bias dependence in behavior which is distinct from the Cu(111) background the molecule is physisorbed to. Here I will show some plots where the Cu behavior is normalized out.

The observed behaviors of these molecules strongly implies that they are physisorbed to the surface which leads to difficulties in maintaining consistent tip con-

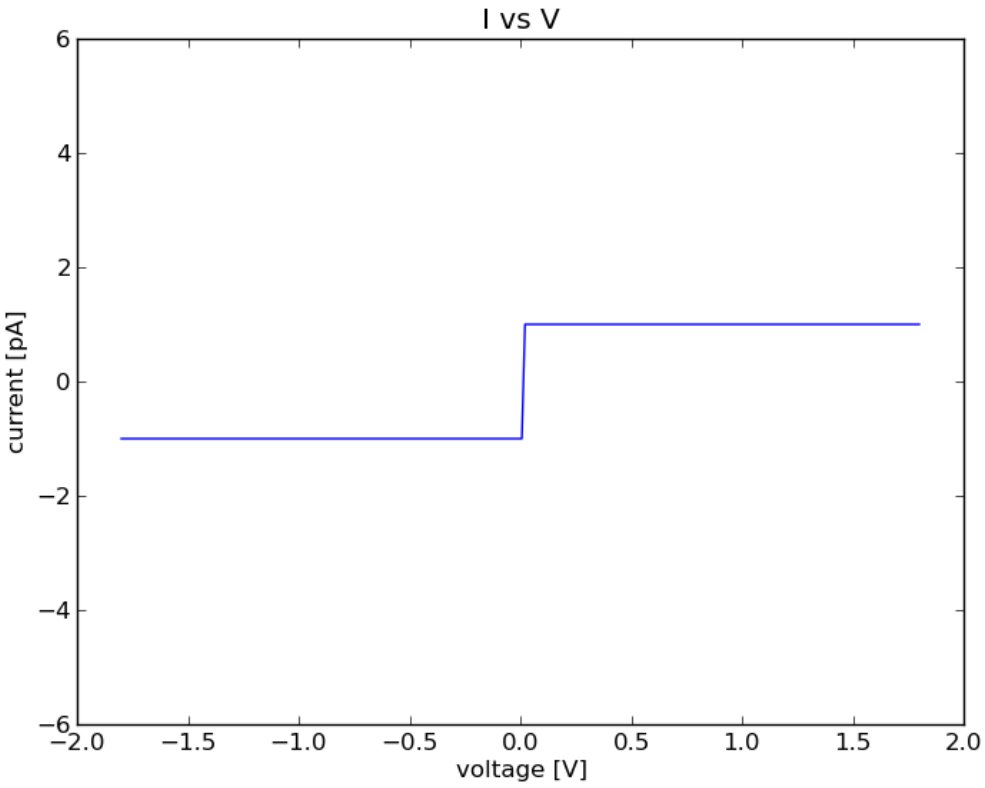

Figure 8.2: Here is the Cu IV curve normalized to itself. We have an antisymmetry around $0\,V$, but see a perfectly metallic behavior.

ditions during imaging and only partial wave function overlap (poor conducting paths out of the molecule).

When we compare Figures 8.2 and 8.3 we notice that they are similar except for the central region near zero bias (extending out to approximately $\pm 0.5\,V$, indicating that near zero bias the molecular states and the surface states are not strongly overlapping.

When we compare Figures 8.2 and 8.4 we notice that they are not substantially similar except indicating that the molecular states and the surface states are not strongly overlapping in any bias region. This supports the conclusions from the

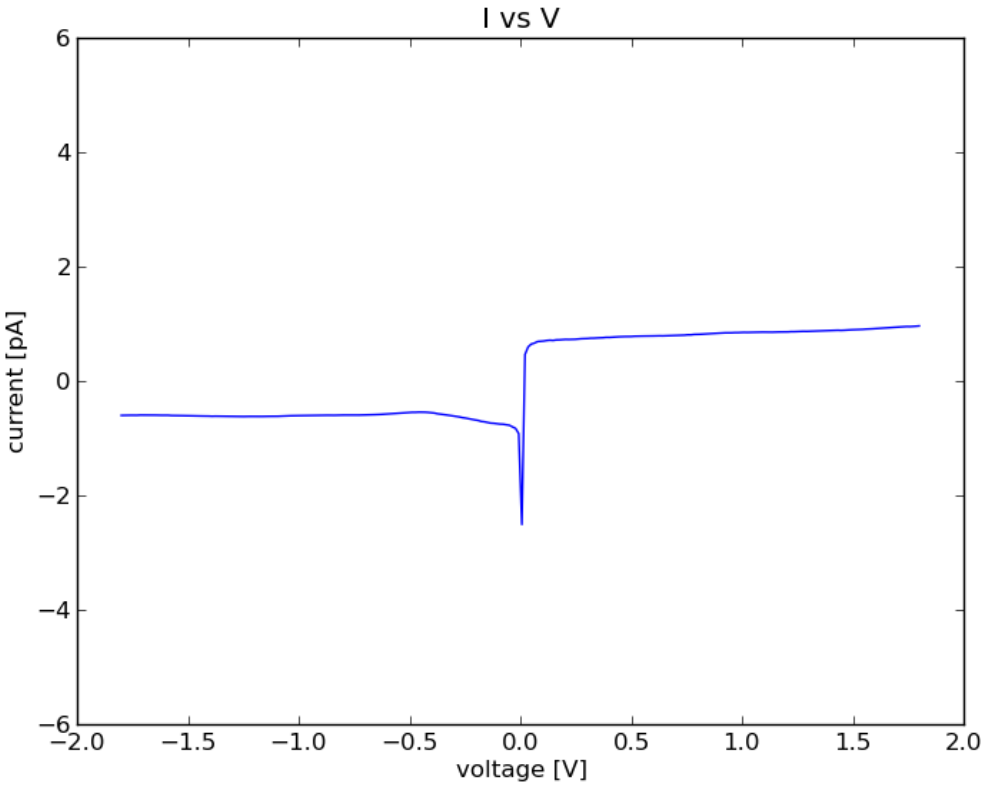

Figure 8.3: This is a typical interior region IV curve normalized by the Cu background curve. We see that there must have been a fair overlap of wave functions, but there are distinct behaviors in the low bias voltage region leading to asymmetries.

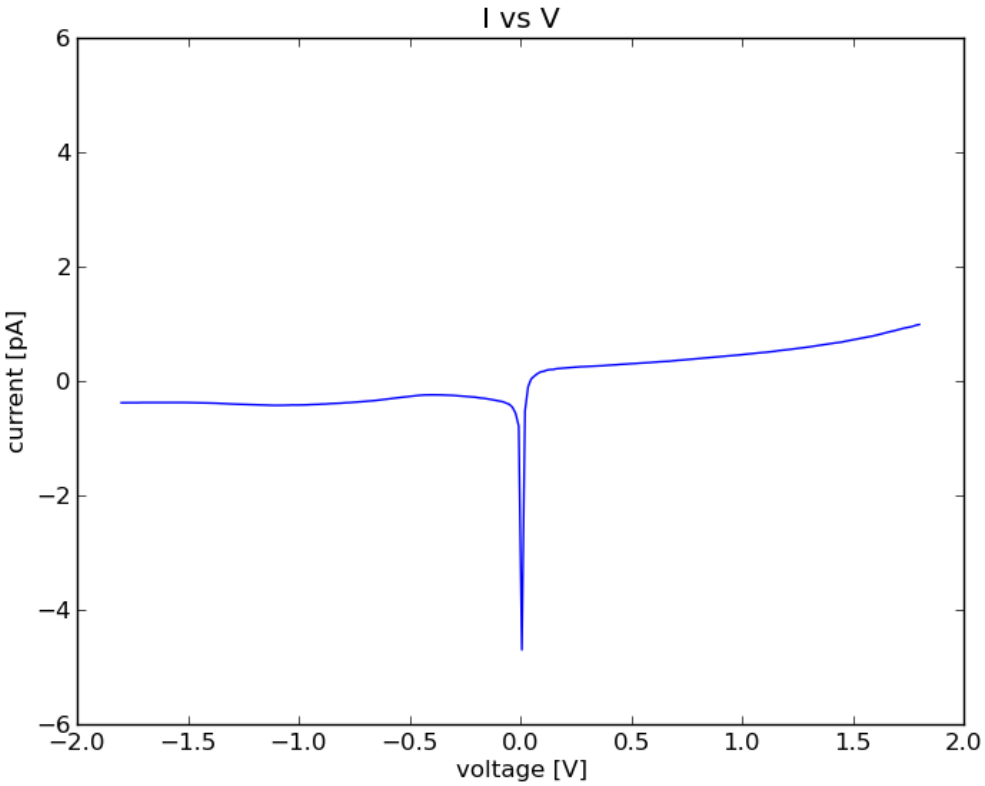

Figure 8.4: This is the eye region IV curve normalized by the Cu background cure. We notice immediately that there is almost no overlap, so the molecular core must have been strongly isolated from the surface wave function by the organic shell. This is as we would have expected.

literature regarding the isolated nature of the molecular core by the organic shell.

Our data below 1 K was insufficient in quantity to draw conclusions from.

Beyond our experimental results we produced meaningful collaborations with theorists to predict a class of molecular magnets whose spin states would be invariant under noise from the strain of landing on an uneven surface or small thermal fluctuations. This work involved intensive computation and an iterative approach to building physical models followed by tearing them into rigorously solvable mathematical models.

REFERENCES

[1] D. Seo, *Alignment of Micro-Crystals of MN12-Acetate and Direct Observation of Single Molecules Thereof*, Dissertation, Texas A&M University, 2007.

[2] Salvador Barraza-Lopez,* Michael C. Avery, and Kyungwha Park, Phys. Rev. B, 2007, **76**, 224413.

[3] J. R. Friedman and M. P. Sarachik, Single-Molecule Nanomagnets, Annual Review of Condensed Matter Physics, 2010, **1**, 109.

[4] R. Sessoli and D. Gatteschi and A. Caneschi and M. A. Novak, Nature, 1993, **365**, 141.

[5] A. Candini, G. Lorusso, F. Troiani, A. Ghirri, S. Carretta, P. Santini, G. Amoretti, C. Muryn, F. Tuna, G. Timco, E. J. L. McInnes, R. E. P. Winpenny, W. Wernsdorfer, and M. Affronte, Phys. Rev. Lett. **104**, 037203, 2010.

[6] D. Gatteschi, A. Cornia, M. Mannini, and R. Sessoli, Inorg. Chem. 2009, **48**, 3408.

[7] B. Wen, P. Subedi, L. Bo, Y. Yeshurun, M. Sarachik, A. Kent, A. Millis, C. Lampropoulos, and G. Christou, Phys. Rev. B, 2010, **82**, 014406.

[8] L. Thomas, F. Lionti, R. Ballou, D. Gatteschi, R. Sessoli, and B. Barbara, Nature VOL 1996, **383**.

[9] W. Wernsdorfer, Int. J. Nanotechnol. 2010, **7**, 497.

[10] N Regnault, Th Jolicur, R Sessoli, D Gatteschi, and M Verdaguer, Phys. Rev. B., 2002, **66**, 054409.

[11] Theocharis C Stamatatos, Khalil A Abboud, Wolfgang Wernsdorfer, and George Christou, Angew. Chem. Int. Ed. 2008, **47**, 6694 .

[12] J. R. Friedman, J. Supercond., 1999, **12**, 689.

[13] J. R. Friedman, M. P. Sarachik, J. Tejada and R. Ziolo, Phys. Rev. Lett., 1996, **76**, 3830.

[14] R. Sessoli, H.-L. Tsai, A. R. Schake, S. Wang, J. B. Vincent, K. Folting, D. Gatteschi, G. Christou, and D. N. Hendrickson, J. Am. Chem. Soc. 1993, **115**, 1804.

[15] A. Saywell, A. J. Britton, N. Taleb, M. del C. Gimenez-Lopez, N. R. Champness, P. H. Beton and J. N. Oshea, Nanotechnology 2011, **22**, 075704.

[16] N. Domingo, E. Bellido and D. Ruiz-Molina, Chem. Soc. Rev. 2012, **41**, 258.

[17] J. Yoo, E. M. Rumberger, D. N. Hendrickson, A. Yamaguchi, H. Ishimoto, E. K. Brechin, and G. Christou, J. Appl. Phys. 2002, **91**, 7155.

[18] W Wernsdorfer, N Chakov, and G Christou, Phys. Rev. B, 2004, **70**, 132413.

[19] R. Wiesendanger, H. J. Güntherodt, G. Güntherodt, R. J. Gambino, and R. Ruf, Phys. Rev. Lett. 1990, **65**, 247.

[20] A. Saywell, G. Magnano, C. J. Satterley, L. M. A. Perdigao, A. J. Britton, N. Taleb, M. del C. Gimenez-Lopez, N. R. Champness, J. N. Oshea and P. H. Beton, Nat. Commun. 2010, **1**, 75.

[21] S. Kahle, Z. Deng, N. Malinowski, C. Tonnoir, A. Forment-Aliaga, N. Thontasen, G. Rinke, D. Le, V. Turkowskix, T. S. Rahman, S. Rauschenbach, M. Ternes, and K. Kern, Nano lett. 2012, **12**, 518.

[22] Kai Sun, Kyungwha Park, Jiale Xie, Jiyong Luo, Hongkuan Yuan, Zuhong Xiong, Junzhong Wang, and Qikun Xue, ACS Nano, 2013, 7 (8), 6825

[23] Engelhardt L, Schroder C. Singapore: World Scientific., 2012, 241.

[24] Tsai SH, Lee HK, Landau DP. Am. J. Phys., 2005, **73**, 615.

[25] R. Moroni, R. Buzio, A. Chincarini, U. Valbusa, F. Buatier de Mongeot, L. Bogani, A. Caneschi, R. Sessoli, L. Caviglid, and M. Gurioli, J. Mater. Chem., 2008, **18**, 109.

[26] K. Reaves, K. Kim, K. Iwaya, T. Hitosugi, H. G. Katzgraber, H. Zhao, K.R. Dunbar, and W. Teizer, SPIN 2013, **03**, 01, 1350004.

[27] D. M. Seo, V. Meenakshi, W. Teizer, H. Zhao, and K. R. Dunbar, J. Magn. Mater. 2006, **301**, 31.

[28] K. Kim, A. Ford, V. Meenakshi, W. Teizer, H. Zhao, and K. R. Dunbar, J. Appl. Phys. 2007, **102**, 094306.

[29] M. Ruben, J.-M. Lehn, and P. Mller, Chem. Soc. Rev. 2006, **35**, 1056.

[30] D. M. Packwood, K. T. Reaves, F. L. Federici, H. G. Katzgraber and W. Teizer, Proc. R. Soc. London, A, 2013, **469**, 20130373.

[31] G. Binnig, H. Rohrer, Ch. Gerber, and E. Weibel, Phys. Rev. Lett. 1982 **49**, 57.

[32] L. Cannavacciuolo and D. P. Landau, Phys. Rev. B, 2005, **71**, 134104.

[33] Dante Gatteschi, Roberta Sessoli, and Jacques Villain, *Molecular Nanomagnets*, Oxford University Press, 2006.

[34] W. Wernsdorfer, Adv. Chem. Phys. 2001, **118**, 99.

[35] R. C. Jaklevic, John Lambe, A. H. Silver, and J. E. Mercereau, Phys. Rev. Lett.,1964. **12**, 159.

[36] S. N. Erné, H.D. Hahlbohm and H. Lbbig, J. Appl. Phys., 1976, **47**, 5440.

APPENDIX A

PRE-CONDITIONING OF CU SUBSTRATE

Load the sample in the usual way: Sonicate the new Cu Crystal in ethanol and DI water. Load into load-lock, pump to an acceptable pressure to transfer to the sample-prep chamber ($\approx 10^{-7}$ torr).

A.0.0.1 Preparation of the chamber to sputter and anneal (in the presence of the sputter gas)

1. Close the gate valve which connects the sample prep chamber to the load-lock chamber (where the pumping is occurring). See Figure A.1.

2. Shut off the Ion pump by pressing 'OFF' and then 'POWER' on the Ion Pump Controller (Rack mount above STM controller, labeled 'PREP'). See Figure A.2.

   Pressure will rise in the sample-prep chamber, which is indicated via the ion pump gauge (which is the black pressure gauge rack mounted above the TC gauge for the turbo pump in the load-lock chamber. See Figure A.3.

3. Walk to the Argon gas leak valve, the black mark should be 'up' at 12 o'clock. This indicates that it is closed. Rotate the valve less than two turns (about 1 hour 50 minutes rotation). The valve should end in the 2 o'clock position. See Figure A.4.

   Check the pressure gauge, the target pressure is $2 * 10^{-5}$ torr, reaching this pressure follows a logarithmic curve, so the last part of the approach is slow. Be patient. The whole process takes approximately one minute.

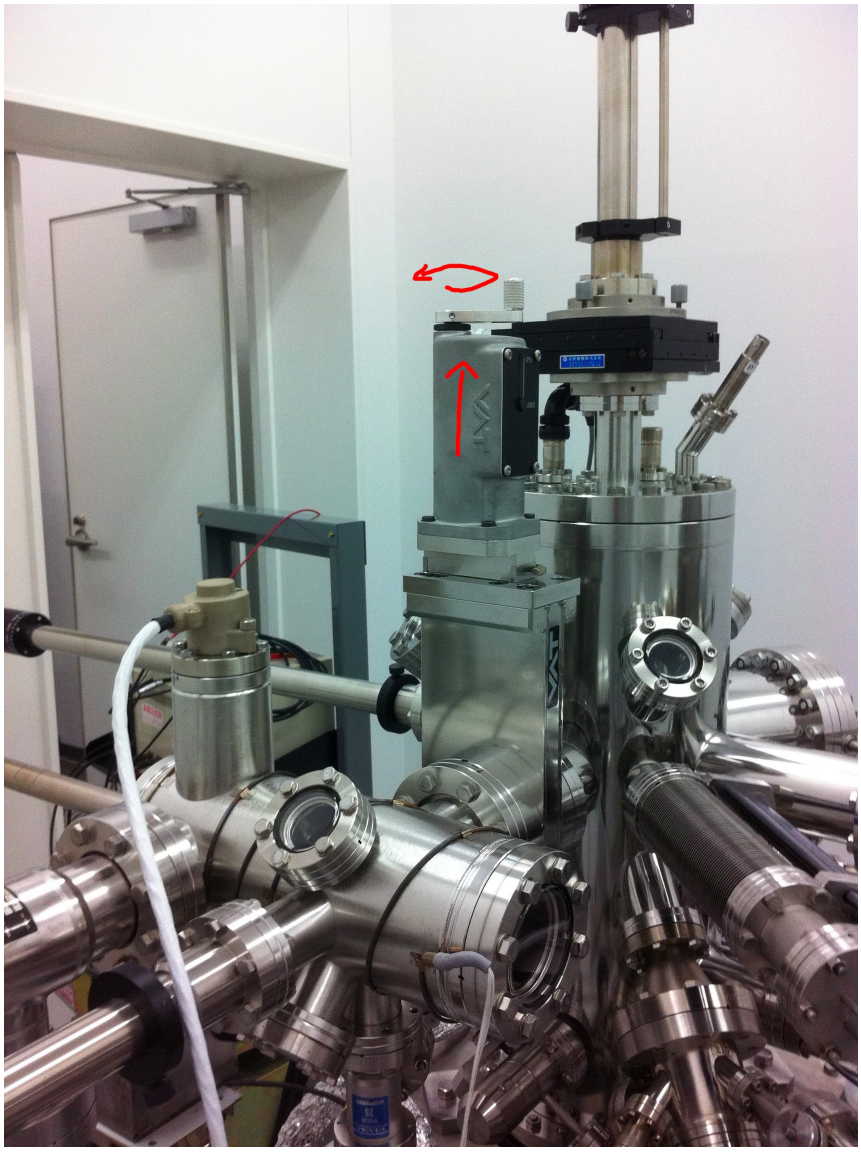

Figure A.1: This is the gate valve between the load-lock and sample-prep chambers.

4. After having filled the prep chamber with Argon, quickly close the leak valve and then turn off the pressure gauge by pressing the 'EMIS' button.

5. The preparation to sputter and anneal is complete,

Figure A.2: This is the Ion Pump Controller panel, located above the STM controller.

A.0.0.2 Sputtering

1. Attach the feed through leads (which are connected to the sample) to the ion gun controller box (second to bottom rack on the mobile rack near the door, inside the STM room). See Figure A.5.

2. Turn on the ion controller box by pressing 'ON' in the lower left corner.

3. Turn the 'Emission' knob all the way to 10.0 (all the way on), can be done quickly.

4. Turn the 'Filament' knob to 6.1 slowly.

Figure A.3: This is the pressure gauge for the sample-prep chamber, located above the gauge for the load-lock chamber.

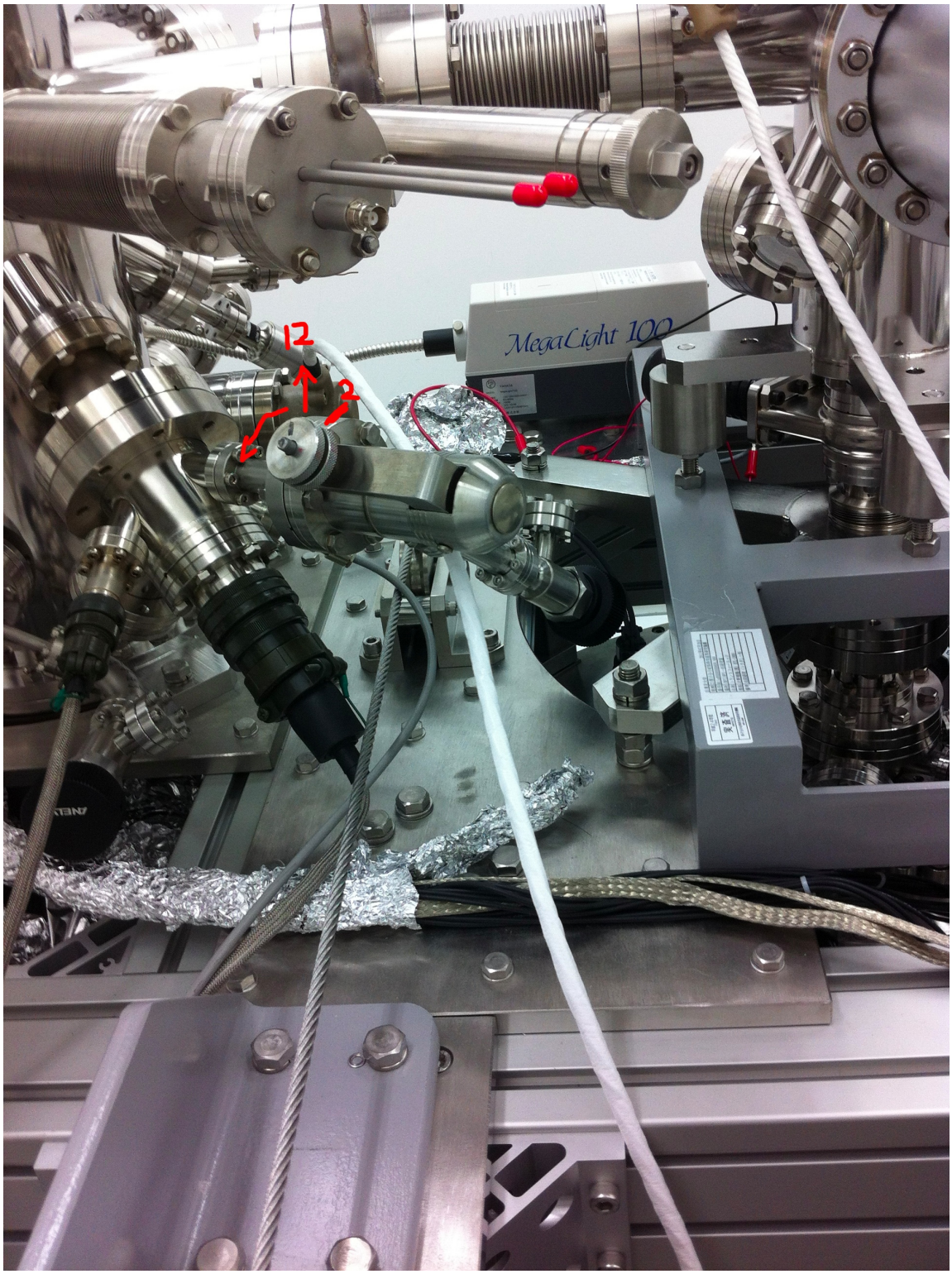

Figure A.4: This is the Argon leak valve into the sample-prep chamber for sputtering.

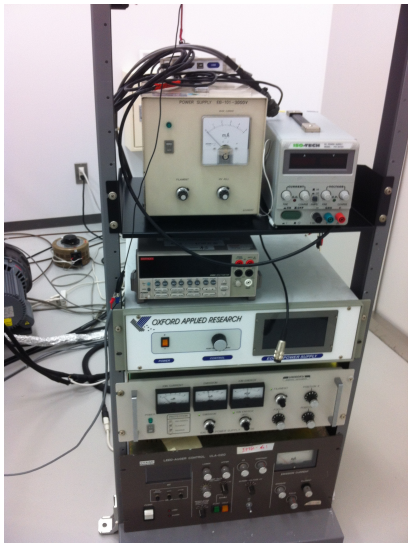

Figure A.5: This is the mobile rack containing the Sputter Gun controller and the DC power supply.

5. Turn the 'Energy' knob up until the Energy Gauge reads 1.5KV. The current should go up as this is done. This can be done quickly.

6. Let the sputtering process continue for 20 minutes.

7. Turn off sputtering by following these directions in reverse.

A.0.0.3 Annealing

1. If changing the sputter gas: open the gate valve to the load-lock chamber (to allow pumping through the turbo pump), then turn on the pressure guage by pressing 'EMIS' on the black pressure gauge panel, rack mounted above the pressure gauge for the load-lock chamber. Then turn on the ion guage by pressing 'POWER' and then 'ON Lock.' See Figure A.6.

2. Connect the feed through leads to the DC power supply (which should be off). Connect one lead to the '+' terminal and one to the '-' terminal.

(a) Rear Panel (b) Front Panel

Figure A.6: This is the rear panel and front panel of the DC power supply, note the current knob turned all the way up.

3. To ensure voltage limited rather than current limited performance, while at 0V turn the current knob all the way up.

4. Turn the voltage up to 19V and the corresponding current should be approximately 0.3A

5. Wait 10 minutes.

6. Turn off in reverse order.

APPENDIX B

BUILDING OUR DATABASE

This code was written by Ross McDonald:

This is the script for forming the MySQL Database:

```
#!/usr/bin/python


import os




for root, dirs, files in os.walk('.'):
   for name in files:
      iterator = 'python scanLoader.py'+ ' '+ os.path.join(root, name)
      os.system(iterator)
```

This script obviously requires *scanLoader.py*, which is given here:

```
#!/usr/bin/python
import struct
import math
import md5
import sqlalchemy
import os
import sys
import hashlib
import re
```

```
import datetime
import sqlalchemy.orm
import sqlalchemy.ext.declarative
from PIL import Image


db = sqlalchemy.create_engine(
'mysql://root:password@localhost/scanDB?charset=utf8&use_unicode=0',
    echo=False)
tableMetaData = sqlalchemy.MetaData()
tableMetaData.bind = db
scanTable = sqlalchemy.Table('Scans', tableMetaData, autoload=True,
    autoload_with=db)
scanPointsTable = sqlalchemy.Table('ScanPoints', tableMetaData,
    autoload=True, autoload_with=db)

Base = sqlalchemy.ext.declarative.declarative_base()

class Scan(Base):
   __table__ = scanTable

   id = scanTable.c.id
   filename = scanTable.c.filename
   hash = scanTable.c.hash
   gridSizeX = scanTable.c.gridSizeX
   gridSizeY = scanTable.c.gridSizeY
   dx = scanTable.c.dx
```

```
    dy = scanTable.c.dy
    sweepPoints = scanTable.c.sweepPoints
    startX = scanTable.c.startX
    startY = scanTable.c.startY
    startTime = scanTable.c.startTime
    endTime = scanTable.c.endTime

    def __init__(self, header=None):
        if header:
            self.filename = header.filename
            self.hash = header.hash
            self.gridSizeX = header.xPixels
            self.gridSizeY = header.yPixels
            self.dx = header.dx
            self.dy = header.dy
            self.sweepPoints = header.sweepPoints
            self.startX = header.startX
            self.startY = header.startY
            self.startTime = header.startTime
            self.endTime = header.endTime

    def __repr__(self):
        return "<Scan('%s', '%s', '%s', '%s')>" % (self.filename,
            self.gridSizeX, self.gridSizeY, self.sweepPoints)

class ScanPoint(Base):
    __table__ = scanPointsTable
```

```
id = scanPointsTable.c.id

scanId = scanPointsTable.c.scanId

v = scanPointsTable.c.voltage

i = scanPointsTable.c.current

lix = scanPointsTable.c.lix

x = scanPointsTable.c.x

y = scanPointsTable.c.y

z = scanPointsTable.c.z

ibwd = scanPointsTable.c.current_bwd

lixbwd = scanPointsTable.c.lix_bwd

zbwd = scanPointsTable.c.z_bwd


def __init__(self, x, y, v):

   self.x = x

   self.y = y

   self.v = v

   self.z = None

   self.zbwd = None

   self.i = None

   self.ibwd = None

   self.lix = None

   self.lixbwd = None

   self.vbwd = None


def __repr__(self):

   return "<ScanPoint('%s', '%s', '%s')>" % (self.x, self.y, self.v)
```

```
class BinaryReader:
   def __init__(self, fileName):
      self.file = open(fileName, 'rb')

   def read(self, formatStr):
      size = struct.calcsize(formatStr)
      value = self.file.read(size)
      if size != len(value):
         raise Exception
      return struct.unpack(formatStr, value)

   def skip(self, size):
      if(len(self.file.read(size)) < size):
        raise Exception

   def close(self):
      self.file.close()

   def __del__(self):
      self.file.close()

class Header3DS:
   def __init__(self, filename):
      #common parameters
      self.filename = filename
      self.xPixels = 0
```

```
self.yPixels = 0
self.sweepPoints = 0
self.startTime = None
self.endTime = None
self.startX = 0
self.startY = 0
self.dx = 0
self.dy = 0

#3DS parameters
self.experimentParams = None
self.fixedParams = None
self.sweepSignal = None
self.channels = None

f = open(filename, 'r')
line = ''
while not ':HEADER_END:' in line:
   line = f.readline()
   m = re.search('Grid dim="(\d+) x (\d+)"', line)
   if m:
      self.xPixels = int(m.group(1))
      self.yPixels = int(m.group(2))
      continue;
   m = re.search('Fixed parameters="([^"]*)"', line)
   if m:
      self.fixedParams = m.group(1).split(';')
```

```
            continue
        m = re.search('Experiment parameters="([^"]*)"', line)
        if m:
            self.experimentParams = m.group(1).split(';')
            continue
        m = re.search('Channels="([^"]*)"', line)
        if m:
            self.channels = m.group(1).split(';')
            continue
        m = re.search('Sweep signal="([^"]*)"', line)
        if m:
            self.sweepSignal = m.group(1)
            continue
        m = re.search('Points=(\d+)', line)
        if m:
            self.sweepPoints = int(m.group(1))
            continue;
        m = re.search('Start time="([^"]*)"', line)
        if m:
            self.startTime = datetime.datetime.strptime(m.group(1),
                '%d.%m.%Y %H:%M:%S')
            continue
        m = re.search('End time="([^"]*)"', line)
        if m:
            self.endTime = datetime.datetime.strptime(m.group(1), '%d.%m.%Y
                %H:%M:%S')
            continue
```

```
            m = re.search('Grid settings=([^\r]*)', line)
            if m:
                settings = [float(x) for x in m.group(1).split(';')]
                self.startX = settings[0]
                self.startY = settings[1]
                self.dx = settings[2]
                self.dy = settings[3]
                continue
        self.size = f.tell()
        f.close()

class HeaderSXM:
    def __init__(self, filename):
        #common parameters
        self.filename = filename
        self.xPixels = 0
        self.yPixels = 0
        self.sweepPoints = 1
        self.startTime = None
        self.endTime = None
        self.startX = 0
        self.startY = 0
        self.dx = 0
        self.dy = 0

        #3DS parameters
        self.bias = None
```

```
self.startTime= None
self.channels = []


f = open(filename, 'r')
line = ''
while not ':SCANIT_END:' in line:
   line = f.readline()
   if ':SCAN_PIXELS:' in line:
      line = f.readline()
      tokens = line.split()
      self.xPixels = int(tokens[0])
      self.yPixels = int(tokens[1])
   elif ':SCAN_OFFSET:' in line:
      line = f.readline()
      tokens = line.split()
      self.startX = float(tokens[0])
      self.startY = float(tokens[1])
   elif ':REC_DATE:' in line:
      line = f.readline()
      self.startDate = datetime.datetime.strptime(line.split()[0],
          '%d.%m.%Y')
   elif ':REC_TIME:' in line:
      line = f.readline()
      self.startTime = datetime.datetime.strptime(line.split()[0],
          '%H:%M:%S')
   elif ':BIAS:' in line:
      line = f.readline()
```

```
            self.bias = float(line)
        elif ':SCAN_RANGE:' in line:
            line = f.readline()
            tokens = line.split()
            self.xRange = float(tokens[0])
            self.yRange = float(tokens[1])
        elif ':DATA_INFO:' in line:
            f.readline()
            line = f.readline()
            tokens = line.split("\t")
            while len(tokens) == 7:
                self.channels.append(tokens[2])
                if 'both' in tokens[4]:
                    self.channels.append(tokens[2]+'[bwd]')
                line = f.readline()
                tokens = line.split("\t")
        elif ':SCANIT_TYPE:' in line:
            line = f.readline()
            tokens = line.split()
            self.dataFormat = ''
            if tokens[1] == 'MSBFIRST':
                self.dataFormat += '>'
            else:
                self.dataFormat += '<'
            if tokens[0] == 'FLOAT':
                self.dataFormat += 'f'
            else:
```

```
                self.dataFormat += 'lf'

        f.readline()
        f.readline()
        f.read(2)
        self.size = f.tell()
        f.close()

        #xRange might itself be dx? ask Kelley
        self.dx = self.xRange / (self.xPixels-1)
        self.dy = self.yRange / (self.yPixels-1)

class HeaderDAT:
    def __init__(self, filename):
        #common parameters
        self.filename = filename
        self.xPixels = 1
        self.yPixels = 1
        self.sweepPoints = 0
        self.startTime = None
        self.endTime = None
        self.startX = 0
        self.startY = 0
        self.dx = 0
        self.dy = 0

        #DAT parameters
```

```
        self.columns = None

        f = open(filename, 'rb')
        for line in f:
            if '[DATA]' in line:
                line = next(f)
                self.columns = line.split('\t')
                break;

            tokens = line.split('\t')
            if 'Date' in tokens[0]:
                self.startTime = datetime.datetime.strptime(tokens[1],
                    '%d.%m.%Y %H:%M:%S')
            elif 'X ' in tokens[0]:
                self.startX = float(tokens[1])
            elif 'Y ' in tokens[0]:
                self.startY = float(tokens[1])
            elif 'Num Pixel' in tokens[0]:
                self.sweepPoints = int(tokens[1])
        self.size = f.tell()
        f.close()

def safeIndex(l, key):
    try:
        return l.index(key)
    except:
        return None
```

```
def parse3DS(reader, header):
   sweepPoints = []


   try:
     for x in xrange(header.xPixels):
        for y in xrange(header.yPixels):
           startV = reader.read('>f')[0]
           endV = reader.read('>f')[0]
           vInc = (endV - startV) / (header.sweepPoints-1)
           for i in range(len(header.experimentParams)):
              reader.skip(4)
           sweep = [ScanPoint(x,y, startV + vInc*n) for n in
               xrange(header.sweepPoints)]
           for chan in xrange(len(header.channels)):
              name = header.channels[chan]
              attr = None
              if name == 'Z (m)':
                 attr = 'z'
              elif name == 'Z [bwd] (m)':
                 attr = 'zbwd'
              elif name == 'Current (A)':
                 attr = 'i'
              elif name == 'Current [bwd] (A)':
                 attr = 'ibwd'
              elif name == 'LIX 1 omega (A)':
                 attr = 'lix'
```

```
            elif name == 'LIX 1 omega [bwd] (A)':
               attr = 'lixbwd'
            for k in xrange(header.sweepPoints):
             if attr:
                value = reader.read('>f')[0]
                if math.isnan(value) or math.isinf(value):
                   value = None
                setattr(sweep[k], attr, value)
             else:
                reader.skip(4)
         for point in sweep:
          sweepPoints.append(point)
   except:
      pass
   return sweepPoints


def parseDAT(reader, header):
   scanPoints = []
   channelMap = {}
   biasIndex = 0
   for i, channel in enumerate(header.columns):
      if 'Bias calc ' in channel:
         biasIndex = i
      elif 'Current [bwd] ' in channel:
         channelMap['ibwd'] = i
      elif 'Current ' in channel:
         channelMap['i'] = i
```

```
            elif 'LIX 1 omega [bwd] ' in channel:
                channelMap['lixbwd'] = i
            elif 'LIX 1 omega ' in channel:
                channelMap['lix'] = i
            elif 'Z [bwd] ' in channel:
                channelMap['zbwd'] = i
            elif 'Z ' in channel:
                channelMap['z'] = i

        reader.file.seek(0)
        while not '[DATA]' in reader.file.readline():
            pass
        reader.file.readline()
        for line in reader.file:
            tokens = line.split('\t')
            scanPoint = ScanPoint(0,0, float(tokens[biasIndex]))
            for channel, i in channelMap.iteritems():
                value = float(tokens[i])
                if math.isnan(value) or math.isinf(value):
                    value = None
                setattr(scanPoint, channel, value)
            scanPoints.append(scanPoint)
        return scanPoints

    def parseSXM(reader, header):
        scanPoints = []
```

```
    for x in xrange(header.xPixels):
        for y in xrange(header.yPixels):
            scanPoints.append(ScanPoint(x, y, header.bias))

    try:
        for chan in header.channels:
            attr = None
            if chan == 'Z':
                attr = 'z'
            elif chan == 'Z[bwd]':
                attr = 'zbwd'
            elif chan == 'Current':
                attr = 'i'
            elif chan == 'Current[bwd]':
                attr = 'ibwd'
            for x in xrange(header.xPixels):
                for y in xrange(header.yPixels):
                    value = reader.read(header.dataFormat)[0]
                    if math.isnan(value) or math.isinf(value):
                        value = None
                    if attr:
                        setattr(scanPoints[x*header.xPixels + y], attr, value)
    except:
        pass
    return scanPoints

def hashFile(filename, blocksize=65536):
```

```
    f = open(filename, 'r')
    h = hashlib.sha256()
    buf = f.read(blocksize)
    while len(buf)>0:
        h.update(buf)
        buf = f.read(blocksize)
    f.close()
    return h.digest()


def uploadScan(data, header):
    scan = Scan(header)
    session.add(scan)
    session.commit()
    for point in data:
        point.scanId = scan.id
        session.add(point)
    session.commit()

def parseHeader(filename):
    ext = os.path.splitext(filename)[1]
    header = None
    if ext == '.3ds':
        header = Header3DS(filename)
    elif ext == '.sxm':
        header = HeaderSXM(filename)
    elif ext == '.dat':
```

```
      header = HeaderDAT(filename)
   if header:
      header.hash = hashFile(filename)
   return header

def parseData(filename, header):
   reader = BinaryReader(filename)
   reader.skip(header.size)
   data = None
   if isinstance(header, Header3DS):
      data = parse3DS(reader, header)
   elif isinstance(header, HeaderSXM):
      data = parseSXM(reader, header)
   elif isinstance(header, HeaderDAT):
      data = parseDAT(reader, header)
   reader.close()
   return data

def uploadFile(filename):
   header = parseHeader(filename)
   if not header:
      return
   data = parseData(filename, header)
   uploadScan(data, header)

Session = sqlalchemy.orm.sessionmaker(bind=db)
session = Session()
```

```
uploadFile(sys.argv[1])
```

APPENDIX C

ANALYSIS SCRIPTS

This code was written by me for analyzing 3ds files one voltage frame at a time. It can also be used on single stm images which are single voltage frames already. Ross McDonald helped me to get the syntax for connecting to the MySQL database correct.

```
#!/usr/bin/python


import sqlalchemy
import numpy as np
import matplotlib.pyplot as mpl
import os
from matplotlib.font_manager import FontProperties


fontP = FontProperties()
fontP.set_size('small')


db = sqlalchemy.create_engine('mysql://root:password
@localhost/scanDB?charset=utf8&use_unicode=0', echo=False)



#  scanId = [13, 64, 69, 70, 76, 78, 88, 90, 351, 372, 580, 593, 605, 715,
   722 ,747, 795, 834, 929, 994, 1025, 1027, 1028, 1131, 2130, 2685,
   2702, 2708, 2970, 2984, 3144] #ad a list of valid 3ds scanIds
scanId = [722]
```

```
for item in scanId:
   fig = mpl.figure()

   with db.begin() as connection:

      volt = [] # hold a list of the unique voltages in a given scan file
         for parsing frame by frame (id, voltage) define a frame
      cur = []
      lix = []
      x = []
      y = []

      scanMetadata = connection.execute("SELECT gridSizeX,
         gridSizeY,startX, startY, dx, dy, startTime FROM scanDB.Scans
         WHERE id = "+ str(item) + ";").first() #grabs the metadata from
         the scans db for the given id

#     gridsizex = scanMetadata['gridSizeX']
#     maxx = gridsizex - 5
#     gridsizey = scanMetadata['gridSizeY']
#     maxy = gridsizey - 5
      #limit = " AND (x >= 20 AND x <= 25) AND (y >= 30 AND y <= 35);"
      limit = " AND (y = 7) AND (x >= 8 AND x <= 10);"
#     limit = " AND y = 7;"
```

```
      #print limit

      coords = connection.execute("SELECT DISTINCT x, y FROM
          scanDB.ScanPoints WHERE scanId = "+ str(item) + str(limit) +
          ";") #grabs the voltage table for a given scanId and returns the
          distinct values

#     coords = connection.execute("SELECT DISTINCT x, y FROM
    scanDB.ScanPoints WHERE scanId = "+ str(item) + ";") #no limits on
    coordinates

      for loc in coords:
         x.append(loc['x'])
         y.append(loc['y'])

      for i in x:
         for j in y:
            if j == max(y):
               i = i + 1

               scanData = connection.execute("SELECT current, lix, voltage
                   FROM scanDB.ScanPoints WHERE scanId = " + str(item) + " AND
                   x = " + str(i) + " AND y = " + str(j) + ";") #checks our
                   unique frame and comes back with data

               for point in scanData:
                  if not point['current'] == None:
```

```
            cur.append(float(point['current'])) #formatted into nA
        #  if not point['lix'] == None:
        #     lix.append(float(point['lix'])*10**12) #lix is formatted
            into nA/nV
           if not point['voltage'] == None:
              volt.append(float(point['voltage']))

        label = "(" + str(i) + "," + str(j) + ")"

        #print volt, cur
        mpl.plot( volt, cur )
        mpl.xlabel('voltage [V]')
        mpl.ylabel('current [A]')

        cur[:] = []
        volt[:] =[]
        lix[:] = []


        if j == max(y) and i == max(x):
           break
     if i == max(x):
        x[:] = []
        y[:] = []
        break

filename = str(item) + str(limit) + "iv_inMolecule.png" #save the scan
```

```
    and list the voltage and scanID #
  dirname = "/home/kelley/Desktop/presentation/overview/"+
    str(scanMetadata['startTime']) + "iv/"

  if not os.path.exists(dirname):
    os.makedirs(dirname)

  os.chdir(dirname)

  mpl.title('I vs V not normalized')
#  mpl.legend(loc = 'center left', ncol = 2, bbox_to_anchor=(1,0.5), prop
   = fontP, borderaxespad = 0 )
  mpl.savefig(filename)

  mpl.clf()
```